

UC Berkeley

UC Berkeley Electronic Theses and Dissertations

Title

On-Surface Synthesis and Local Electronic Structure Characterization of Low-Dimensional Nano-Materials

Permalink

<https://escholarship.org/uc/item/20w305p0>

Author

Chen, Chen

Publication Date

2018

Peer reviewed|Thesis/dissertation

**On-Surface Synthesis and Local Electronic Structure Characterization of
Low-Dimensional Nano-Materials**

by

Chen Chen

A dissertation submitted in partial satisfaction of the

requirements for the degree of

Doctor of Philosophy

in

Chemistry

in the

Graduate Division

of the

University of California, Berkeley

Committee in charge:

Professor Michael F. Crommie, Co-Chair

Professor Felix R. Fischer, Co-Chair

Professor Feng Wang

Professor Jeffrey R. Long

Spring 2018

**On-Surface Synthesis and Local Electronic Structure Characterization of
Low-Dimensional Nano-Materials**

Copyright 2018
by
Chen Chen

Abstract

On-Surface Synthesis and Local Electronic Structure Characterization of

Low-Dimensional Nano-Materials

by

Chen Chen

Doctor of Philosophy in Chemistry

University of California, Berkeley

Professor Michael F. Crommie, Co-Chair

Professor Felix R. Fischer, Co-Chair

Understanding of the electronic properties of new materials is of central importance for science and technology. In particular, low-dimensional nano-materials exhibit exotic properties that are determined by quantum mechanics. Rapid development of reticular chemistry has enabled the syntheses of a variety of low-dimensional condensed matter systems that are formed by linking up molecular building blocks. This dissertation focuses on the on-surface synthesis of such materials and consequent characterization of their local electronic structure with scanning tunneling microscopy (STM).

The structure – property relationship of two low-dimensional nano-materials will be described: quasi-one-dimensional (1D) graphene nanoribbons (GNRs) and two-dimensional (2D) covalent organic frameworks (COFs). In the case of GNRs, we first show that two compatible molecular precursors with different sizes lead to GNR heterojunctions with atomically precise interfaces. In order to test predictions for how doped GNRs should behave, we synthesized B-doped GNRs with different doping concentrations on Au(111). Characterization of their electronic properties revealed a symmetry-dependent hybridization between the dopant states and the underlying Au substrate. We also describe our efforts to synthesize N=11 armchair GNRs through sp^3 -to- sp^2 conversion of carbon atoms. In the case of 2D COFs, we first show that formation of imine linkages within COF366-OMe causes a downshift in the frontier orbital energy of porphyrin cores due to the electron-withdrawing characteristics of imine bonds. We then demonstrate the ability to achieve a 2D lattice of type II heterojunctions through judicious choice of molecular precursors that result in an asymmetrical bonding scheme within a 2D COF.

Our studies show that on-surface synthesis can lead to the realization of target nanostructures that are unreachable *via* solution-based methods, as demonstrated by intra-molecular reactions that lead to new “nano-graphene” species.

Contents

Contents	i
List of Figures	iv
List of Abbreviations	vi
Acknowledgments	vii
1 Introduction	1
1.1 Low-Dimensional Nano-Materials	1
1.1.1 Graphene Nanoribbons	2
1.1.2 Two-Dimensional Covalent Organic Frameworks	3
1.1.3 Other Molecular Species	4
1.2 Surface Chemistry and Bottom-up Synthesis	4
1.2.1 Ullmann-Type Reaction	5
1.2.2 Schiff-Base Condensation (Imine Formation) Reaction	7
1.3 Principles of Scanning Tunneling Microscopy and Spectroscopy	8
1.3.1 The Bardeen Theory of Electron Tunneling	9
1.3.2 Asymmetry in Tunneling Spectrum	12
1.3.3 The Tersoff—Hamann Model	14
2 Instrumentation	18
2.1 Low-Temperature STM	18
2.1.1 UHV Chambers	18
2.1.2 Cryogenics	19
2.1.3 Vibration Isolation System	20
2.1.4 STM Scanner	20
2.1.5 Electronics and Software	21
2.2 Room-Temperature STM	22
2.3 Evaporator Cells	22
2.4 Quartz Crystal Microbalance	24
3 Graphene Nanoribbons	25
3.1 Molecular Bandgap Engineering in 7-13 Armchair GNR Heterojunction	25

3.1.1	Bottom-up Synthesis and Local Characterization of Electronic States	26
3.1.2	Theoretical Calculations and Comparison to Experimental Results	30
3.1.3	Summary	33
3.2	Concentration Dependence of Dopant Electronic Structure in Boron-doped N=7 AGNRs	33
3.2.1	Concentration-Dependent Dopant Electronic Structure	34
3.2.2	Synthesis and Characterization of B-doped AGNRs with Different Dopant Concentrations	35
3.2.3	Symmetry-Dependent Hybridization between the Dopant States and Au(111) Substrate	40
3.2.4	Summary	44
3.3	N=11 AGNRs	45
3.3.1	On-Surface Synthesis of N=11 AGNRs <i>via</i> sp ³ -to-sp ² conversion	45
3.3.2	Quality of N=11 AGNRs Characterized by STM and nc-AFM	47
3.3.3	Summary	49
3.4	Conclusion and Outlook	50
4	Two-Dimensional Covalent Organic Frameworks	51
4.1	Symmetrical Bonding Scheme: COF366-OMe	51
4.1.1	Electronic Structure of the Core Precursor Molecule TAPP	51
4.1.2	Synthesis of COF366-OMe on Au(111) from Precursor Molecules	53
4.1.3	Local Electronic Structure of COF366-OMe Measured by STM	54
4.1.4	Theoretical Calculations and Comparisons to Experimental Results	57
4.1.5	Summary	58
4.2	Asymmetrical Bonding Scheme: TAPP-TFPP-COF	59
4.2.1	Synthesis of TAPP-TFPP-COF on Au(111) Surface	59
4.2.2	Local Electronic Structure of TAPP-TFPP-COF Measured by STM	60
4.2.3	Theoretical Calculations and Comparisons to Experimental Results	63
4.2.4	Hirshfeld Charge Analysis and Dipole-Induced Energy Shift	64
4.2.5	Summary	66
4.3	Conclusion and Outlook	66
5	Molecular Species	68
5.1	Surface-Assisted Synthesis of Peripentacene	68
5.1.1	Background on Periacenes	68
5.1.2	Synthesis of Peripentacene on a Au(111) Surface	69
5.1.3	Summary	71
5.2	On-Surface Nano-Graphene Synthesis from <i>ortho</i> -Arylene Precursors	72

5.3 Conclusion	73
Bibliography	74
Appendix: List of All Molecules Studied	85

List of Figures

1.1 Classical Ullmann coupling reaction	6
1.2 Reaction scheme of N=7 AGNRs	6
1.3 Schiff-base condensation reaction	7
1.4 Schematic of an STM	9
1.5 An energy diagram of the tip-sample junction	14
1.6 The Tersoff–Hamann model of STM	16
2.1 Overview of UHV LT-STM	19
2.2 STM stage and scanner	21
2.3 A Knudsen cell evaporator	23
2.4 A dual-cell evaporator	24
3.1 Comparison of bandgap between N=13 AGNR and N=7 AGNR	26
3.2 Bottom-up synthesis of 7-13 AGNR heterojunctions	27
3.3 STM dI/dV spectroscopy of 7-13 AGNR heterojunction electronic structure	28
3.4 Comparison of experimental dI/dV maps and theoretical LDOS for a 7-13 AGNR heterojunction	29
3.5 Theoretical electronic structure of 7-13 AGNR heterojunction	32
3.6 Band structure evolution of freestanding boron-doped N=7 armchair graphene nanoribbons at different dopant densities	35
3.7 Electronic structure of dilute boron-doped N=7 AGNR on Au(111)	37
3.8 Electronic structure of densely boron-doped N=7 AGNR on Au(111)	39
3.9 DFT-LDA calculation of dilute-doped N=7 GNR on Au(111) substrate	42
3.10 DFT-LDA calculation of densely-doped N=7 GNR on Au(111) substrate	44
3.11 Proposed Synthetic Route of N=11 AGNRs	46
3.12 Representative STM images and chemical structures after each annealing stage during growth of N=11 AGNRs	47
3.13 STM and AFM images of N=11 AGNRs	49
4.1 Single TAPP molecule electronic structure	52
4.2 Synthesis of COF366-OMe on a Au(111) surface	54
4.3 STS measurements of COF366-OMe on Au(111) surface	55
4.4 Spatial distribution of COF366-OMe electronic states	56
4.5 Synthesis and STM imaging of TAPP-TFPP-COF on Au(111)	60

4.6 Local electronic structure of TAPP-TFPP-COF measured by STS and dI/dV mapping.....	62
4.7 Structure of TAPP-TFPP-COF/Au(111) and PDOS calculated by DFT.....	63
4.8 Partial charge density plots and Hirshfeld charge analysis of TAPP-TFPP-COF.....	65
5.1 Chemical structure of n-periacene, peripentacene, and 6,6'-bipentacene.....	69
5.2 STM images of bipentacene and peripentacene.....	70
5.3 STM and nc-AFM images of a single peripentacene.....	71
5.4 Reaction scheme from <i>ortho</i> -arylene to nano-graphene.....	72
5.5 STM images of H-Ar-3 and H-8 molecules on Au(111)	73

List of Abbreviations

AFM: Atomic Force Microscopy
AGNR: Armchair Graphene Nanoribbons
CB: Conduction Band
CMOS: Complementary Metal–Oxide–Semiconductor
COF: Covalent Organic Framework
DFT: Density Functional Theory
DMA: 2,5-dimethoxybenzene-1,4-dicarboxaldehyde
DOS: Density of States
FET: Field Effect Transistor
FWHM: Full Width at Half Maximum
GNR: Graphene Nanoribbons
HOPG: Highly Oriented Pyrolytic Graphite
LDA: Local Density Approximation
LDOS: Local Density of States
MIM: Metal-Insulator-Metal
MOF: Metal Organic Framework
nc-AFM: non-contact Atomic Force Microscopy
PAH: Polycyclic Aromatic Hydrocarbon
PDOS: Projected Density of States
QCM: Quartz Crystal Microbalance
RT: Room Temperature
STM: Scanning Tunneling Microscopy
STS: Scanning Tunneling Spectroscopy
TAPP: (5,10,15,20-tetrakis (4-aminophenyl) porphyrin
TMDC: Transition Metal Dichalcogenide
TFPP: (5,10,15,20-tetrakis (4-formylphenyl) porphyrin
TSP: Titanium Sublimation Pump
UHV: Ultra-High Vacuum
VB: Valence Band
ZGNR: Zigzag Graphene Nanoribbons
2D: Two-Dimensional

Acknowledgement

I am grateful to many people who helped me throughout my journey as a PhD student. I have been fortunate to work with great scientists with different skills, expertise, and above all, their unwavering love for science. First of all, I am indebted to my advisor Professor Michael Crommie for his trust in me when I was a chemistry graduate fresh out of college, who knew nothing about condensed matter physics, not even the concept of band structure. He has trained me to think as a physicist, to ask relevant and important questions, and to present ideas with simple and intuitive pictures. I am forever grateful for his massive support, both financially and academically.

I want to thank the people that I have worked directly with. Yen-Chia Chen introduced me to STM and trained me on the home-built low temperature STM which produced the majority of work described in this dissertation. Dimas G. de Oteyza was very nice to me during our short overlap, and I was happy to see him doing great in San Sebastian, Spain during my recent visit. Zahra Pedramrazi worked with me for the longest amount of time. I have been inspired by her diverse interests, as well as her passion for the things she loves and stands for. Danny Haberer has great practical skills, and I have learned a lot from him. Trinity Joshi is a very organized person and pays great attention to details. As a graduate student and a mom, she is the perfect example of modern women who excel at both career and family. Gaoqiang Wang joined us when I was preparing to graduate; he learns fast and works hard, and I am sure he will be very productive during his stay in the group. I have also worked with some brilliant undergraduate students and knowledgeable visiting scholars, including Won-Woo Choi, Nick Kau, Bobby Ge, Eric Yu, Lingjie Zhou, Pintu Das, Irene Rodriguez, Peinian Liu, and Ting Chen. Many of them have made significant contributions to the work described in this dissertation. I also want to thank former graduate student Ryan Yamachika, who knows the lab and instrumentation so well that we would always go to him for help when we were out of our depth dealing with malfunctioning instruments.

Other members of the Crommie group have always made me feel welcomed. I enjoyed discussions with Dan Rizzo on graphene nanoribbons and their topological properties. I had a lot of dinners with Dillon Wong, Salman Kahn, Chad Germany, Hsin-Zon Tsai and Juwon Lee, mostly in restaurants on the south side of campus. Some of the conversations we had during those dinners covered topics ranging from society to psychology, from religions to politics, from sports to arts, and they broadened my horizon dramatically. I miss playing soccer regularly with Sebastian Wickenburg and Giang Nguyen, who are both great players. There are numerous people in the group that have helped me in one way or another, and I have enjoyed conversations and interactions with them. To name a few, Yi Chen, Franklin Liou, Andrew Aikawa, Aaron Bradley, Kacey Meaker, Yang Wang, Christopher Bronner, Charlotte Herbig, Miguel Moreno Ugeda, Jairo Velasco Jr., Arash A. Omrani, Jiong Lu, and Alex Riss.

Our interdisciplinary research is based on close collaborations with chemists, theorists, and electrical engineers. Professor Felix Fischer and his group members helped synthesize precursor molecules for graphene nanoribbons. Professor William Dichtel, Professor Omar Yaghi, Professor Seth Marder, and their respective group members helped synthesize precursor molecules for covalent organic frameworks. Professor Steve Louie and his students Ting Cao, Fangzhou Zhao helped us greatly in calculating and interpreting the electronic properties of graphene nanoribbons, whereas Professor Jean-Luc Bredas and his group members Hong Li, Huifang Li helped us understand covalent organic frameworks theoretically. Professor Jeffrey Bokor and his group members made graphene nanoribbons into electronic devices and tested their properties. It has been a pleasant experience interacting with so many experts within their respective field of study, and I have learned so much from them.

My Berkeley PhD experience has been greatly enhanced by an excellent group of administrative staff. As a chemistry graduate student working in a physics lab, I have been supported by staff members from both chemistry and physics. Aileen Harris, Lynn Keithlin from chemistry helped me with various paperwork, and most importantly, getting financial support from teaching. Our group assistant Lisa Partida, and Elaine Quiter helped me with all the nuisances on getting funded, equipment purchase, and travel reimbursement. Eleanor Crump, Anthony Vitan, and Carlos Bustamante from physics have provided massive support ranging from building access to shipping and receiving. All of these nice people made my life as a graduate student so much easier, and I could focus solely on research.

I would like to express my deep gratitude towards my family. My father Tianrong Chen and mother Xiaochun Yang both work in academic institutions, and they taught me dedication, integrity, and humility. My parents in law Caifeng Xie and Jianlin Zhou, who I only started to know in my later years as a PhD student, loved me as their own son. And finally to my wife Mo Zhou, who supported me throughout my ups and downs and inspired me with her work in machine learning and artificial intelligence, I want to say thank you and I am really lucky to have you in my life.

Last but not least, I would like to pay tribute to Mr. Arsène Wenger, who has inspired me ever since I was a teenager, for his loyalty, his commitment, his passion, and his grace in adversity.

Chapter 1

Introduction

1.1 Low-Dimensional Nano-Materials

We live in a world of rapid technological advancement. The age of information has seen a revolution in people's style of living, as daily activities such as connecting with friends, shopping, and travelling have become easier and have allowed for greater interconnectivity. A crucial driving force for this revolution has been unprecedented computation power, which has been fueled by the continuing miniaturization of electronic circuitry. As the device size for Si-based complementary metal-oxide-semiconductor (CMOS) technology approaches nanometer length scale ($1 \text{ nm} = 10^{-9} \text{ m}$), however, challenges have begun to arise that include electrostatic effects such as diminishing gate control, quantum effects such as tunneling and interfering waves, atomistic effects such as dopant fluctuations, and so on [1]. In order to support the rapid development of information technology — including new focuses on artificial intelligence and machine learning — these challenges/barriers need to be overcome.

One approach to overcome these challenges is to look for new materials with superior properties and to explore the possibility of their integration into novel electronic devices. From a scientific rather than technological perspective, the creation of new materials and exploration of their physical properties are important to broaden the scope of human knowledge. The synthesis and characterization of new types of low-dimensional nano-materials will be the main topic of this dissertation.

The nano-materials discussed here mainly consist of light non-metallic elements from the first three rows of the period table, and carbon plays a central role in all of these materials due to its capability to form a variety of chemical scaffolds with strong covalent bonds. It is essentially the same reason that carbon is the center of organic chemistry and all living things on earth. The meaning of “low-dimensional” here is two-fold: (1) the size of the materials under study is small, and (2) these materials have reduced dimensionality compared to regular bulk three-dimensional materials. Both the small size and reduced dimensionality lead to material properties dominated by the laws of quantum mechanics, and result in new properties not seen for bulk 3D materials.

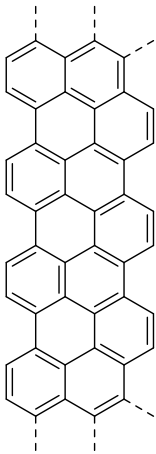
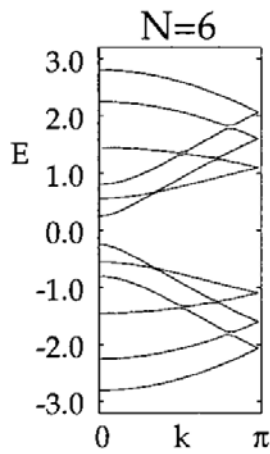
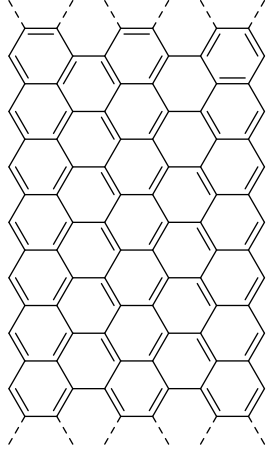
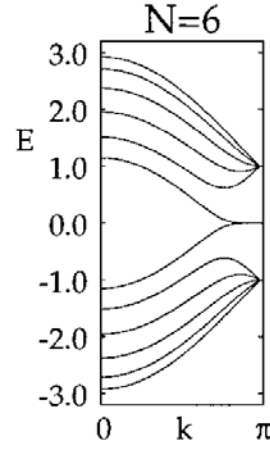
In this introductory chapter, I will briefly introduce the following low-dimensional nano-materials: quasi-one-dimensional graphene nanoribbons, two-dimensional covalent organic frameworks, and other molecular species. I will also introduce bottom-up synthesis on surfaces. Following this introductory chapter, I will discuss instrumentation (Chapter 2), graphene

nanoribbons (Chapter 3), covalent organic frameworks (Chapter 4), and molecular species (Chapter 5).

1.1.1 Graphene Nanoribbons

Graphene nanoribbons (GNRs) are quasi-one-dimensional strips of graphene. Despite its extraordinary properties [2, 3], graphene lacks an energy gap and cannot be switched off like a normal semiconductor device. GNRs, on the other hand, have a tunable energy gap which is dependent on the width and edge geometry of the ribbon [4-7]. Two GNR edge structures with high symmetry are armchair and zigzag edges, and the width of a GNR can be represented by an integer number N (Table 1.1).

Table 1.1 Basic Information on GNRs

Edge Geometry	Chemical Structure	Definition of Width Integer N	Representative Tight-binding Band Structure*
Armchair (AGNR)		Number of carbon rows across the width (6-AGNR on the left)	
Zigzag (ZGNR)		Number of zigzag chains across the width (6-ZGNR on the left)	

* Taken from ref [5].

A particularly useful way to think about the band structure of a graphene nanoribbon is by starting with the Dirac cone of the graphene bands. Sampling the Dirac cone at different slicing planes and projecting them onto a one dimension band structure using a zone-folding scheme will give a good approximation of GNR band structure [5]. With this crude treatment, one can already see how the width (which determines the distance between adjacent slicing planes) and edge geometry (which decides the orientation of the slicing planes in the k-space of graphene) are of crucial importance to the band structure of GNRs. Some modification to GNR band structure does arise when DFT calculations are carried due to edge relaxations and spin polarization effects [6], and further utilization of the GW approximation generally results in a bigger energy gap compared to DFT results [7-9]. More details on the theoretical analysis of GNRs can be found in Dr. Yen-Chia Chen's PhD dissertation [10].

Earlier experimental realizations of GNRs were typically based on top-down methods including lithography from 2D layers of graphene [11], unzipping carbon nanotubes [12, 13], and other chemical methods [14]. Such methods, however, lack good control over the width or the edge geometry and the resulting GNRs suffered from random defects and inhomogeneity. In 2010, Jinming Cai and coworkers developed a bottom-up method to synthesize atomically precise GNRs with predetermined width and edge geometry [15]. Since then, fabrication of GNRs from small molecules based on rational design of organic chemistry principles has become a growing research field. The ability of a UHV STM system to carry out *in-situ* GNRs growth and to characterize GNRs' local electronic properties makes it an ideal platform for such studies.

1.1.2 Two-Dimensional Covalent Organic Frameworks

Atomically-thin 2D materials have been the focus of intensive research since the turn of the century, both theoretically and experimentally. In particular, graphene and transition metal dichalcogenides (TMDCs) have proved to be excellent platforms for not only novel physics, but also important applications [2, 16-20]. On the other hand, the rapid development of reticular chemistry exemplified by metal organic frameworks (MOFs) and covalent organic frameworks (COFs) has also significantly expanded the chemistry toolbox for making periodic structures and attracted the attention of condensed matter physicists [21-23].

In particular, COFs are extended organic frameworks whose backbones are made of light elements including carbon, boron, nitrogen, oxygen, and so on. These tailored structures are determined by the geometries and chemical identities of their monomers. Since the first successful synthesis of COF-1 from boronic acid precursors [22], numerous COFs with different chemical linkages [24-28], geometries [29-31], and pore sizes [32] have been reported, showing properties of interest for applications such as gas storage [33, 34], catalysis [35-37], and photodetectors [38, 39]. 2D COF films as thin as few or even a single atomic layer have been

synthesized in solution [29, 40, 41], at air/water interfaces [42, 43], and on surfaces [44-48].

Compared to other 2D materials such as graphene and TMDCs, 2D COFs offer the possibility of creating a staggering amount of new materials enabled by organic chemistry. Contrary to the rapid progress in synthesizing many different COFs, however, characterization of their local electronic properties has progressed at a slower rate. A limited number of COFs displaying honeycomb symmetry have been examined using scanning tunneling spectroscopy techniques, revealing different aspects of their frontier orbital electronic structure [49, 50]. More characterizations on different COFs are needed to understand their electronic properties and to guide the rational design of 2D COF synthesis.

1.1.3 Other Molecular Species

Both one-dimensional GNRs and two-dimensional COFs have extended crystalline structure with well-defined momentum. Single molecules, on the other hand, can be regarded as zero-dimensional. The lack of repeating unit cells means that the quantum states of a single molecule cannot be characterized by a wave vector k , and these states are discrete in energy.

The motivations to study single molecule at surfaces are two-fold. First, compared to GNRs or COFs, single molecules are smaller in size and represent the ultimate limit of miniaturization in molecular electronics. Many single molecules we studied were designed to be molecular precursors for extended GNR or COF structures. By studying these molecular species we can understand how electronic structure evolves as single precursor molecules are covalently bonded into extended networks with well-defined wave vector (see section 4.1 for an example). Secondly, the chemistry of these molecular species is also fascinating, especially when they are put onto surfaces. Sometimes, reaction products that are difficult to obtain from traditional solution-based chemistry can be achieved from on-surface synthesis (see section 5.1 for an example).

The history of using STM to study molecular species is almost as long as the history of STM itself. Soon after the invention of STM, there were attempts at imaging biological molecules [51, 52]. A few years later, individual molecules of copper phthalocyanine [53], lipid bilayers [54], and sorbic acid [55] were reported in 1987. Before the turn of the millennium, STM had already been used for not only direct real-space imaging of single molecules, but also single molecule (inelastic) spectroscopy measurements as well as molecular manipulation [56]. Combined with AFM, which is capable of single molecule force spectroscopy [57], local probe characterization became one of the most popular techniques to study molecular species on surfaces in great detail.

1.2 Surface Chemistry and Bottom-up Synthesis

The vast scope of “surface chemistry” contains topics ranging from colloidal science to electrochemistry and heterogeneous catalysis [58]. The focus of our research is on the synthesis

of low-dimensional nano-materials (GNRs and COFs) through surface-assisted chemical reactions. Compared to solution synthesis the nano-materials synthesized from on-surface reactions are usually cleaner and more compatible with local probe measurements. Oriented and atomically flat surfaces of single-crystal noble metals are the standard substrate we use for these studies, due to their compatibility with UHV STM study, as well as their catalytic properties for various reactions of interest.

Surface synthesis has a few distinct characteristics that are absent from solution reactions. Firstly, due to the reduced dimensionality of the surface (3D to 2D), the configuration of reactants absorbed on the surface is usually quite different from their configuration in a solution, and this can lead to different reaction pathways. Secondly, the diffusion of molecular species on a surface is an important step (sometimes even the limiting step [59]) in the reaction pathway. Thirdly, compared to solution reactions, the controlling knobs for surface-assisted reactions are restricted to the choice of substrate and annealing temperature. Although there have been reports of using metals (such as Pt and Pd) deposited onto substrates as catalysts to facilitate on-surface reactions [60, 61], such cases are rare and require good control of the coverage of the deposited metal catalyst.

The differences between on-surface synthesis and solution synthesis dictate that not all solution reactions will find their counterparts on surfaces. On the other hand, surface-assisted reactions may also lead to products that are elusive through solution synthesis (see Chapter 5). Up till now, a number of reactions known to organic chemists have been shown to work on surfaces [62], including aryl-aryl coupling (Ullmann-type reaction), alkyne coupling [63], cyclotrimerization of alkyne [64], condensation reactions of boronic acid [44, 65], Schiff-base condensation reaction [66-68], dimerization of N-heterocyclic carbenes [69], alkane polymerization [70], acylation reactions [71, 72], Bergman cyclization [73, 74], cyclodehydrogenation [15, 75, 76], click reactions [77], Heck reaction [60], and cycloaddition reactions [77, 78]. Here I will briefly introduce the two on-surface reactions that are extensively used in our synthesis of GNRs and COFs, that is, Ullmann-type reactions and Schiff-base condensation reactions.

1.2.1 Ullmann-Type Reaction

The Ullmann reaction was discovered by Fritz Ullmann more than a century ago [79], and has been extensively used in organic synthesis ever since [80]. The classical Ullmann reaction is a coupling reaction between two aryl halides with copper as catalyst, as shown in Figure 1.1.

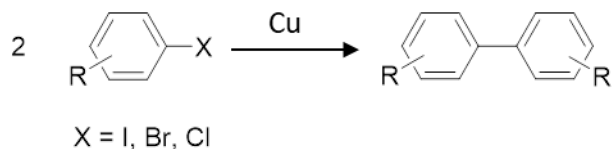


Figure 1.1 Classical Ullmann coupling reaction.

The first realization of surface confined Ullmann-type reaction was reported in early 1990s [81, 82], where the coupling between iodobenzene molecules on Cu(111) surface was studied by means of Auger electron spectroscopy (AES), high resolution electron energy loss spectroscopy (HREELS), temperature-programmed reaction (TPR) spectroscopy, and isotope labelling. Later an STM tip was used to manipulate iodobenzene molecules on Cu(111) and induce the coupling between them [83]. In 2007, a pioneering work by Grill et al. demonstrated the use of on-surface Ullmann-type reaction to achieve covalent bonded networks with predefined geometry [84].

The detailed mechanism of Ullmann-type reactions on metallic surfaces is not completely understood; however, it is generally accepted that the underlying substrate plays an important role in activation and cleavage of the aryl-halogen bond. Different metal substrates have been shown to have different catalytic activity for the on-surface Ullmann-type coupling [62]. Organometallic intermediates have been proposed and captured for coupling reactions on different surfaces of Cu [45, 85-87] and Ag [88, 89], but similar intermediates have not been observed on the Au(111) surface [62].

In 2010, the Ullmann-type coupling was put to use for the surface-assisted synthesis of atomically precise GNRs, where halogenated molecular precursors first link up into polymer chains before the polymers undergo a second step of cyclodehydrogenation to obtain flat GNRs [15]. Since then, Ullmann-type coupling plus cyclodehydrogenation has become a popular strategy to fabricate bottom-up GNRs with different width, edge geometry, and heteroatom doping.

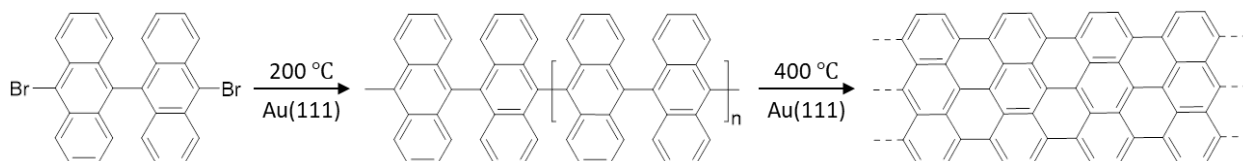


Figure 1.2 Reaction scheme of N=7 AGNRs. Annealing the dibromo- bianthracene precursors to 200 °C results in the formation of linear polymers through Ullmann-type coupling. A second annealing step to 400 °C give rise to the formation of N=7 AGNRs.

1.2.2 Schiff-Base Condensation (Imine Formation) Reaction

Schiff-base is named after Italian chemist Hugo Schiff, who discovered Schiff-bases more than 150 years ago [90]. The general form of a Schiff-base (also called an imine group) is shown in Figure 1.3, and it can be synthesized from a condensation reaction between a carbonyl group and an amine group.

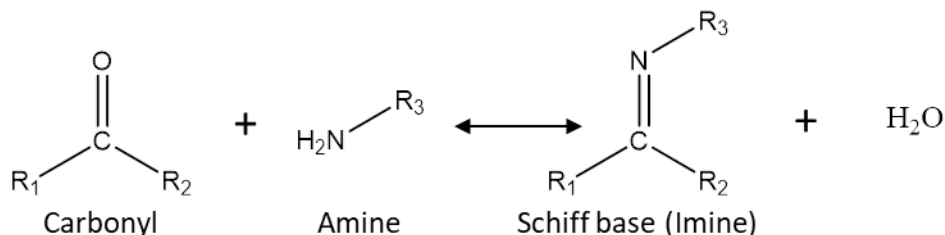


Figure 1.3 Schiff-base condensation reaction. The reaction between a carbonyl group and an amine group gives Schiff-base and water.

The Schiff-base condensation reaction is widely used in the solution synthesis of COFs, due to the high chemical stability of imine linkages [91]. There have also been reports of imine linkage COF growth at the liquid/solid interface [41, 92, 93]; however, under these growth conditions, it is difficult to make COFs as a single layer, and the characterization of their local electronic properties with low temperature STM is very difficult. Recently, a “self-limiting solid-vapor interface reaction strategy” was employed to produce single layer imine linkage COFs on HOPG [48, 67, 94, 95], and ambient STM imaging of the resulting COFs reveals domain sizes on the order of 100 nm. A key feature involved in the synthesis of these imine linkage COFs is the so called “dynamic covalent chemistry” [96], where the reversibility of the Schiff-base condensation reaction offers “error-checking” and “proof-reading” mechanisms, leading to the formation of the most thermodynamically stable structures [23].

In order to produce the “cleanest” possible COF for low temperature STM characterization of its electronic structure, we employed a slightly different approach to synthesize imine linkage COFs. The reaction is still Schiff-base condensation as illustrated in Figure 1.3; however, it occurs in UHV on a metallic surface, and no other species are on the substrate initially except for the two precursors, an amine and a carbonyl. Because the by-product water gets desorbed from the surface during reaction, such a strategy does not allow as good “error correction” as the aforementioned strategies which offer a plethora supply of water molecules. Although the COF domain size we got is smaller (tens of nanometers, see Chapter 4), the lack of solvent and other contaminants on the surface provides an excellent environment for measuring the local electronic structure of the COF species by low temperature STM.

Compared to the Ullmann-type reaction introduced earlier (section 1.2.1), the Schiff-base condensation reaction does not require catalytic activity from the underlying substrate. Therefore, this reaction has the potential to be carried out on insulating substrates such as h-BN and SiO₂, making the resulting COF structures more interesting for electronic device applications.

1.3 Principles of Scanning Tunneling Microscopy and Spectroscopy

This section describes the basic principles of scanning tunneling microscopy (STM) and spectroscopy (STS), which are the major experimental techniques for the study of low-dimensional nano-materials. The first STM was developed by Binnig, Rohrer, Gerber, and Weibel in the early 1980s [97-99], and because of this invention, Binnig and Rohrer were awarded the Nobel Prize in physics in 1986.

Quantum mechanics dictates that an electron has a certain probability to *tunnel* through an energy barrier due to their wave-like characteristics, and this tunneling phenomenon is the basic idea behind STM. In an STM, a metallic tip is brought to close proximity to a conducting sample surface (distance usually < 1 nm). As shown in Figure 1.4, a voltage bias is applied between the tip and the sample, resulting in electrons tunneling through the vacuum gap from one side to the other. The tunneling current is then converted to a voltage and used as an input to a feedback circuit in the STM electronics. Two common modes of STM operation are constant-current mode and constant-height mode. In both modes, the X- and Y- piezos move the tip laterally to create raster scans of the sample surface. In the constant-current mode of operation, the feedback circuit tries to maintain a preset value of the tunneling current by changing the voltage applied on the Z-piezo which controls the tip sample distance. If the detected current is greater (smaller) than the set value, the tip will be moved away from (toward) the sample. The voltages applied to the Z-piezo are translated to relative distance between the tip and the surface, and a two-dimensional topographic image is generated. In the constant-height mode of operation, the feedback circuit is turned off to keep the relative Z- position constant during scan, and the amplitude of tunneling current is recorded to generate a two-dimensional image.

An STM is capable of generating not only topographic images, but also spectroscopic measurements. In the latter case, STS is a technique that probes local electronic structure of the sample. Instead of real-space raster scans, differential tunneling conductance dI/dV is recorded in STS. By turning off the feedback, and recording the dI/dV signal while sweeping the sample-tip bias, one may inspect energy-resolved local electronic structures of the sample.

In order to better understand the principles of STM and STS, the Bardeen theory of electron tunneling [100] and the Tersoff-Hamann model will be discussed [101, 102]. Here only a rough sketch of these theories and key conclusions will be given, and more detailed step-by-step derivations can be found in C. Julian Chen's book "Introduction to STM" [103].

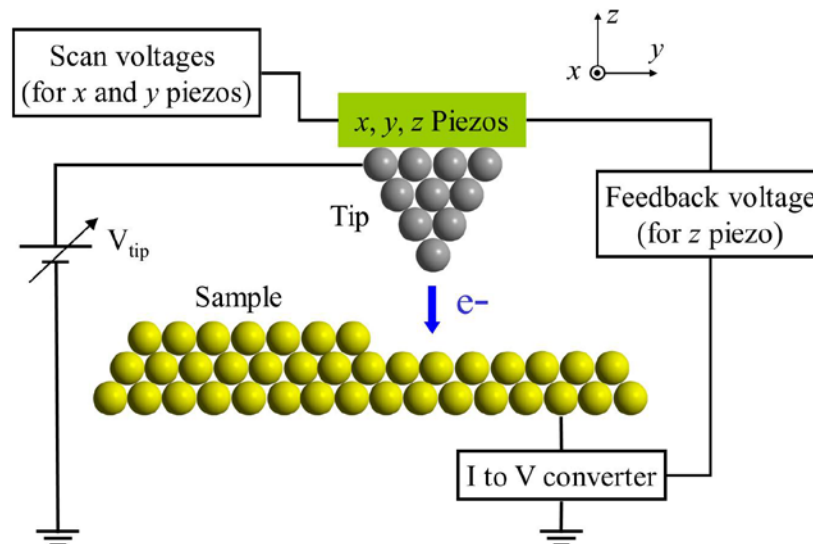


Figure 1.4 Schematic of an STM

1.3.1 The Bardeen Theory of Electron Tunneling

J. Bardeen's original PRL paper "Tunneling from a Many-Particle Point of View" laid down the theoretical basis for the observation of tunneling current flowing between two metals separated by a thin oxide layer [100]. The formalism developed there were later utilized to describe the basic operation principles of STM and STS [103].

Imagine a metal-insulator-metal (MIM) junction; instead of trying to solve the complicated Schrödinger equation for the entire system, Bardeen's ingenious approach was to consider two sub-systems of a metal-insulator interface. The electronic states of the individual sub-systems are obtained by solving the stationary Schrödinger equations of the individual sub-systems. In most cases, those solutions are much easier to obtain than that of the entire junction system. The transmission rate of electrons from one electrode to another is calculated using time-dependent perturbation theory.

Several assumptions/approximations of Bardeen's theory are [104]:

1. Tunneling is sufficiently weak and first-order approximations are sufficient to describe the system.
2. Eigenstates of different electrodes are nearly orthogonal.
3. Electron-electron interactions are ignored.
4. Occupation probabilities for sample and tip states are independent of each other, and they do not change during tunneling.
5. Both the sample and the tip are in electrochemical equilibrium.

In the simplest one dimensional case (junction along Z- axis), when the two electrodes are far apart, the wavefunction of left electrode A satisfies Schrödinger equation:

$$\left[\frac{-\hbar^2}{2m} \frac{\partial}{\partial z^2} + U_A \right] \varphi_A = E_A \varphi_A \quad (1.1)$$

where U_A is the potential function of electrode A, which depends on both time and spatial coordinates, and φ_A is the wavefunction of electrode A.

Similarly for electrode B on the right, we have

$$\left[\frac{-\hbar^2}{2m} \frac{\partial}{\partial z^2} + U_B \right] \psi_B = E_B \psi_B \quad (1.2)$$

Now let's assume at time $t = 0$, φ_μ and ψ_ν are eigenstates of electrodes A and B, and satisfy equation (1.1) and equation (1.2) respectively. As the two electrodes get closer to each other, φ_μ of electrode A is perturbed by the potential of electrode B, and hence has a probability of transferring to the states of electrode B. In other words, we assume the wavefunction of the entire junction system to be

$$\Psi = \varphi_\mu e^{-iE_\mu t/\hbar} + \sum_{\nu=1}^{\infty} c_\nu(t) \psi_\nu e^{-iE_\nu t/\hbar} \quad (1.3)$$

where the coefficients $c_\nu(t)$ are to be determined by

$$i\hbar \frac{\partial \Psi}{\partial t} = \left[\frac{-\hbar^2}{2m} \frac{\partial}{\partial z^2} + U_A + U_B \right] \Psi \quad (1.4)$$

and at time $t = 0$, $c_\nu(0) = 0$.

Inserting equation (1.3) into equation (1.4) leads to

$$i\hbar \sum_{\nu=1}^{\infty} \frac{dc_\nu(t)}{dt} \psi_\nu e^{-iE_\nu t/\hbar} = U_B \varphi_\mu e^{-iE_\mu t/\hbar} + U_A \sum_{\nu=1}^{\infty} c_\nu(t) \psi_\nu e^{-iE_\nu t/\hbar} \quad (1.5)$$

Taking the inner product of both sides of the preceding equation with $\psi_\nu^* e^{iE_\nu t/\hbar}$, and using the fact that φ_μ and ψ_ν are orthogonal because they are eigenstates of different electrodes, we have

$$i\hbar \frac{dc_\nu(t)}{dt} = \int \psi_\nu^* U_B \varphi_\mu e^{-i(E_\mu - E_\nu)t/\hbar} d^3\mathbf{r} + \int \psi_\nu^* U_A \psi_\nu c_\nu(t) d^3\mathbf{r}$$

The second term on the right-hand side can be neglected under the approximation that tunneling is weak enough that coefficients $c_\nu(t)$ are sufficiently small when t is close to 0. Therefore we have

$$i\hbar \frac{dc_\nu(t)}{dt} = \int \psi_\nu^* U_B \varphi_\mu e^{-i(E_\mu - E_\nu)t/\hbar} d^3\mathbf{r} \quad (1.6)$$

Define a tunneling matrix element as

$$M_{\mu\nu} = \int \psi_\nu^* U_B \varphi_\mu d^3\mathbf{r} \quad (1.7)$$

and solve equation (1.6) for $c_\nu(t)$,

$$c_v(t) = M_{\mu\nu} \frac{e^{-i(E_\mu - E_\nu)t/\hbar} - 1}{E_\mu - E_\nu} \quad (1.8)$$

That is to say, if we start with eigenstate φ_μ of electrode A at $t = 0$, the probability of having eigenstate ψ_ν of electrode B at time t will be

$$\rho_{\mu\nu} \equiv |c_\nu(t)|^2 = |M_{\mu\nu}|^2 \frac{4\sin^2((E_\mu - E_\nu)t/2\hbar)}{(E_\mu - E_\nu)^2} \quad (1.9)$$

The function $f(t)$, defined as

$$f(t) = \frac{4\sin^2((E_\mu - E_\nu)t/2\hbar)}{(E_\mu - E_\nu)^2} \quad (1.10)$$

reaches its maximum at $E_\mu = E_\nu$ and approaches zero rapidly for $E_\mu \neq E_\nu$.

If we assume the condition of elastic tunneling $E_\mu = E_\nu$, and utilize the concept of density of states $\rho(E)$, equation (1.9) can be rewritten as

$$\rho_{\mu\nu}(t) = \frac{2\pi}{\hbar} |M_{\mu\nu}|^2 \rho_B(E_\mu) t \quad (1.11)$$

where the mathematical identity $\int_{-\infty}^{+\infty} \frac{\sin^2 au}{\pi a u^2} du = 1$ is used.

Now from the side of electrode A, the number of available states is defined by the density of states of electrode A at energy $\rho_A(E)$, and the energy interval defined by the bias voltage V . Under the assumption that density of states of both electrodes does not vary appreciably near the Fermi level on the range of the applied bias voltage V , the tunneling current is

$$I = \frac{2\pi e^2}{\hbar} |M_{\mu\nu}|^2 \rho_A(E_F) \rho_B(E_F) V \quad (1.12)$$

and the tunneling conductance $G = I/V$ is

$$G = 2\pi^2 G_0 |M_{\mu\nu}|^2 \rho_A(E_F) \rho_B(E_F) \quad (1.13)$$

where $G_0 = \frac{e^2}{\pi\hbar}$ is the conductance quantum.

The derivations above are based on two electrodes A and B separated by a tunnel barrier. By setting one electrode as the tip and the other as the sample, the formalism represents the basic principle of STM. One correction does occur when the temperature is finite and electrons in both electrodes follow the Fermi distribution [105]

$$f(E) = (1 + \exp[(E - E_F)/k_B T])^{-1} \quad (1.14)$$

With a bias voltage V , the total tunneling current is

$$I = \frac{4\pi e}{\hbar} \int_{-\infty}^{+\infty} [f(E_F - eV + \varepsilon) - f(E_F + \varepsilon)] \rho_A(E_F - eV + \varepsilon) \rho_B(E_F + \varepsilon) |M|^2 d\varepsilon \quad (1.15)$$

When $k_B T$ is small, $f(E)$ can be approximated by a step function, and the tunneling current is then

$$I = \frac{4\pi e}{\hbar} \int_0^{eV} \rho_A(E_F - eV + \varepsilon) \rho_B(E_F + \varepsilon) |M|^2 d\varepsilon \quad (1.16)$$

If we assume the tunneling matrix $|M|$ does not change much in the interval of integral,

$$I \propto \int_0^{eV} \rho_A(E_F - eV + \varepsilon) \rho_B(E_F + \varepsilon) d\varepsilon \quad (1.17)$$

indicating a symmetrical contribution to the tunneling current by electronic structure of the two electrodes.

Further analysis of the tunneling matrix $M_{\mu\nu}$ also leads to a more symmetrical form

$$M_{\mu\nu} = \frac{\hbar^2}{2m} \int_{z=z_0} \left[\varphi_\mu \frac{\partial \psi_\nu^*}{\partial z} - \psi_\nu^* \frac{\partial \varphi_\mu}{\partial z} \right] dx dy \quad (1.18)$$

and it is the surface integral of the wavefunctions (and their normal derivatives) of the two electrodes evaluated at the separation surface within the barrier.

1.3.2 Asymmetry in Tunneling Spectrum

When probing electronic structure of various samples, a common observation is that the unoccupied states above the Fermi level of the sample are usually prominent, whereas the occupied states below the Fermi level of the sample are usually obscure and sometimes even missing from the spectroscopy. This phenomenon can be explained by the energy dependence of tunneling matrix element, as described below.

In the gap region, the wavefunction of electrode A is

$$\varphi_\mu(z) = \varphi_\mu(0) e^{-\kappa_\mu z} \quad (1.19)$$

where $z = 0$ indicate the interface between electrode A and the tunnel barrier, and $\kappa_\mu = \sqrt{2mE_\mu}/\hbar$ is the decay constant corresponding to the energy eigenvalue of φ_μ .

Similarly in the gap region, the wavefunction of electrode B is

$$\psi_\nu(z) = \psi_\nu(s) e^{-\kappa_\nu(s-z)} \quad (1.20)$$

where $z = s$ indicate the interface between electrode B and the tunnel barrier, and $\kappa_\nu = \sqrt{2mE_\nu}/\hbar$ is the decay constant corresponding to the energy eigenvalue of ψ_ν . Under the condition of elastic tunneling, $\kappa_\nu = \kappa_\mu = \sqrt{2mE_\mu}/\hbar$.

Inserting equation (1.19) and equation (1.20) into equation (1.18), we obtain

$$\begin{aligned} M_{\mu\nu} &= \frac{\hbar^2}{2m} \int_{z=z_0} 2\kappa_\mu \varphi_\mu(0) \psi_\nu(s) e^{-\kappa_\mu z_0} e^{-\kappa_\mu(s-z_0)} dx dy \\ M_{\mu\nu} &= \left[\frac{\hbar^2}{2m} \int_{z=z_0} 2\kappa_\mu \varphi_\mu(0) \psi_\nu(s) dx dy \right] e^{-\kappa_\mu s} \end{aligned} \quad (1.21)$$

Hence, the energy dependence of tunneling matrix element $M_{\mu\nu}$ is through the decaying constant κ_μ .

Figure 1.5 shows an energy diagram of a tip-sample junction, where a positive sample bias V is applied. The electrons tunnel from the occupied states of the tip into the empty states of the sample. We introduce an average work function $\bar{\phi}$ which is the energy difference of the vacuum level to the middle of the two Fermi levels.

We first rewrite equation (1.16) to a more symmetrical form

$$I = \frac{4\pi e}{\hbar} \int_{-\frac{1}{2}eV}^{\frac{1}{2}eV} \rho_{Tip}(E_F - \frac{1}{2}eV + \varepsilon) \rho_{Sample}(E_F + \frac{1}{2}eV + \varepsilon) |M(\varepsilon)|^2 d\varepsilon \quad (1.22)$$

The decay constant for a tip occupied state of eigenvalue E is

$$\kappa = \frac{\sqrt{2mE}}{\hbar} = \frac{\sqrt{2m(\bar{\phi}-\varepsilon)}}{\hbar} \quad (1.23)$$

Under experimental conditions, ε is smaller than $\frac{1}{2}eV$, and hence much smaller than $\bar{\phi}$, we can expand equation (1.23) to

$$\kappa = \frac{\sqrt{2m(\bar{\phi}-\varepsilon)}}{\hbar} = \frac{\sqrt{2m\bar{\phi}}}{\hbar} \left(1 - \frac{\varepsilon}{2\bar{\phi}}\right) = \kappa_0 \left(1 - \frac{\varepsilon}{2\bar{\phi}}\right) \quad (1.24)$$

where $\kappa_0 = \frac{\sqrt{2m\bar{\phi}}}{\hbar}$ is the decay constant corresponding to the average work function $\bar{\phi}$.

Following equation (1.21) and equation (1.24), we can write the tunneling matrix as a function of the energy parameter ε (see Figure 1.5)

$$M(\varepsilon) = M(0) \exp\left(\frac{\kappa_0 \varepsilon s}{2\bar{\phi}}\right) \quad (1.25)$$

Inserting equation (1.25) into equation (1.22) leads to the expression of tunneling current as

$$I = \frac{4\pi e}{\hbar} \int_{-\frac{1}{2}eV}^{\frac{1}{2}eV} \rho_{Tip}(E_F - \frac{1}{2}eV + \varepsilon) \rho_{Sample}(E_F + \frac{1}{2}eV + \varepsilon) |M(0)|^2 \exp\left(\frac{\kappa_0 \varepsilon s}{\bar{\phi}}\right) d\varepsilon \quad (1.26)$$

If we analyze the above equation carefully, we see that the positive half of the bias interval is more important than the negative half due to the exponential factor at the end.

In the limiting case of gap width s being large enough, the main contribution to the tunneling current (equation (1.26)) comes from a small energy interval near $\varepsilon \approx \frac{1}{2}eV$. In this case, the differential tunneling conductance is approximately

$$\frac{dI}{dV} \approx \rho_{Sample}(E_F + eV) \rho_{Tip}(E_F) \quad (1.27)$$

In other words, by using a positive bias to probe the unoccupied states of the sample, the tunneling current at bias voltage V is proportional to the sample DOS at energy $E_F + eV$, and the tip DOS can be treated as flat. Hence the unoccupied states of the sample are relative easy to probe.

On the other hand, when a negative bias is applied to the sample, electrons tunnel from the occupied states of the sample to the unoccupied states of the tip. In this case, the electronic structure of the tip plays a leading role, resulting in the occupied states of the sample more difficult to probe.

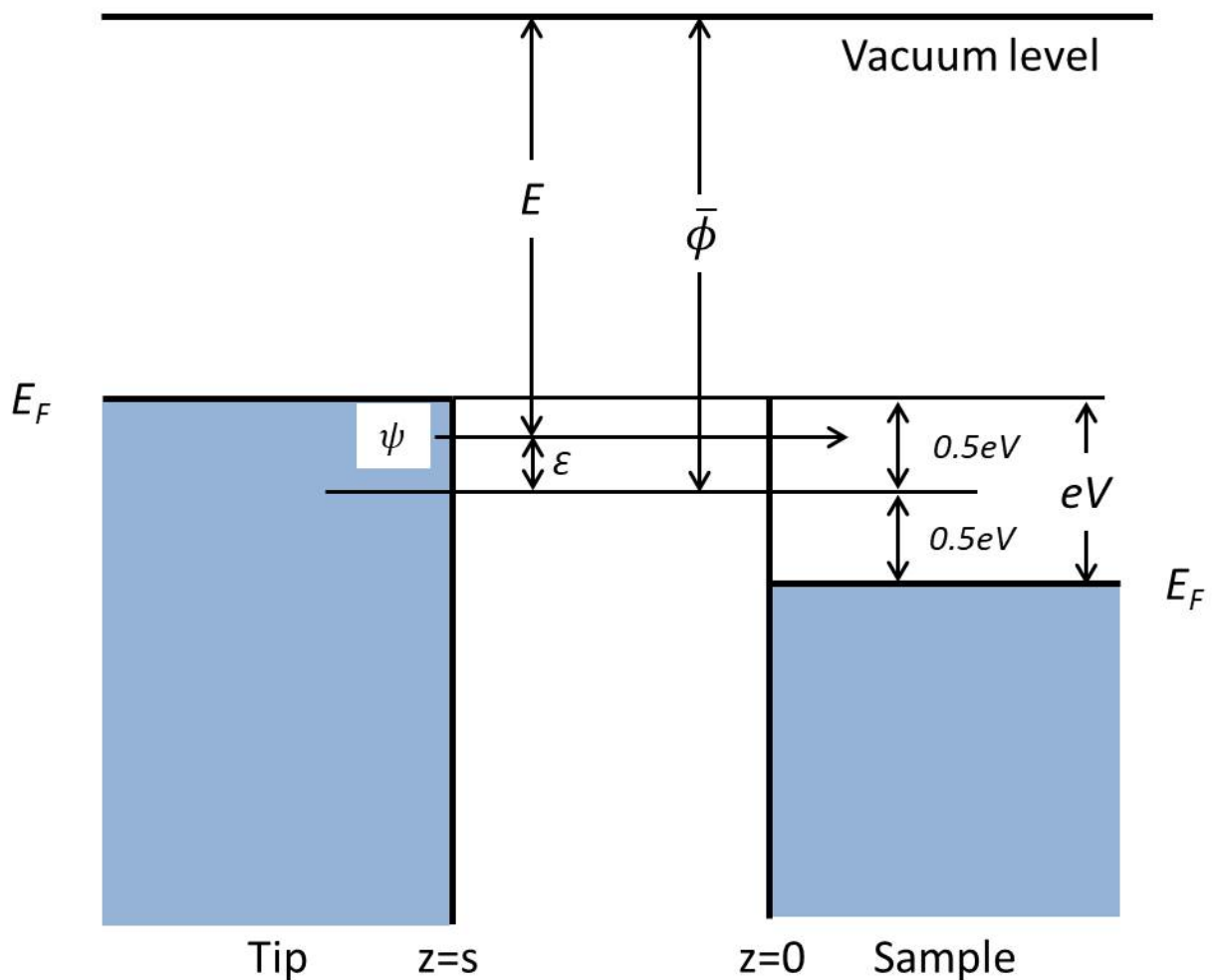


Figure 1.5 An energy diagram of the tip-sample junction. A positive bias voltage V is applied. The electrons tunnel from the occupied states of the tip into the empty states of the sample. Reproduced based on figure 2.5 of reference [103].

1.3.3 The Tersoff—Hamann Model

About one year after the invention of STM, Tersoff and Hamann formulated a widely-used model based on Bardeen's tunneling theory [101, 102]. From Bardeen's theory of tunneling, we

know that the imaging mechanism of STM is a convolution of tip electronic states and sample electronic states. The difficulty to know the exact tip states was the motivation for Tersoff and Hamman, who proposed a particular model of the tip, such that the tip properties can be taken out of the problem of tunneling. Following the discussion in Chen's book [103], the original derivation by Tersoff and Hamman is given below.

As shown in Figure 1.6, the STM tip is modeled as a locally spherical potential well with radius of curvature R centered at \mathbf{r}_0 . The sample surface is represented by the $z = 0$ plane. The center of curvature of the tip is $\mathbf{r}_0 = (0, 0, z_0)$. In the vacuum region, both wave functions of the sample and the tip near the Fermi level satisfy the Schrödinger equation

$$-\frac{\hbar^2}{2m}\Delta\Psi(\mathbf{r}) = -\phi\Psi(\mathbf{r}) \quad (1.28)$$

Here ϕ is the work function, which is related to the decaying constant κ by $\kappa = \sqrt{2m\phi}/\hbar$.

$$\Delta\Psi(\mathbf{r}) = \kappa^2\Psi(\mathbf{r}) \quad (1.29)$$

For the sample wave function in the vacuum, equation (1.29) can be resolved by a two-dimensional Fourier expansion. Using the notation $\mathbf{x} = (x, y)$ and $\mathbf{q} = (k_x, k_y)$, the general form of the sample wavefunction is

$$\varphi(\mathbf{r}) = \int d^2\mathbf{q} f(\mathbf{q}, z) e^{i\mathbf{q}\cdot\mathbf{x}} \quad (1.30)$$

Inserting it into equation (1.29), we obtain the equation for $f(\mathbf{q}, z)$,

$$\frac{d^2}{dz^2} f(\mathbf{q}, z) = (\mathbf{q}^2 + \kappa^2) f(\mathbf{q}, z) \quad (1.31)$$

The solution is

$$f(\mathbf{q}, z) = a(\mathbf{q}) e^{-\sqrt{\mathbf{q}^2 + \kappa^2} \cdot z} \quad (1.32)$$

where $a(\mathbf{q})$ are the coefficients of the Fourier components of the sample surface wavefunction at $z = 0$, and contain all the information of the surface electronic structure. The sample wavefunction in the vacuum region is then

$$\varphi(\mathbf{r}) = \int d^2\mathbf{q} a(\mathbf{q}) e^{-\sqrt{\mathbf{q}^2 + \kappa^2} \cdot z + i\mathbf{q}\cdot\mathbf{x}} \quad (1.33)$$

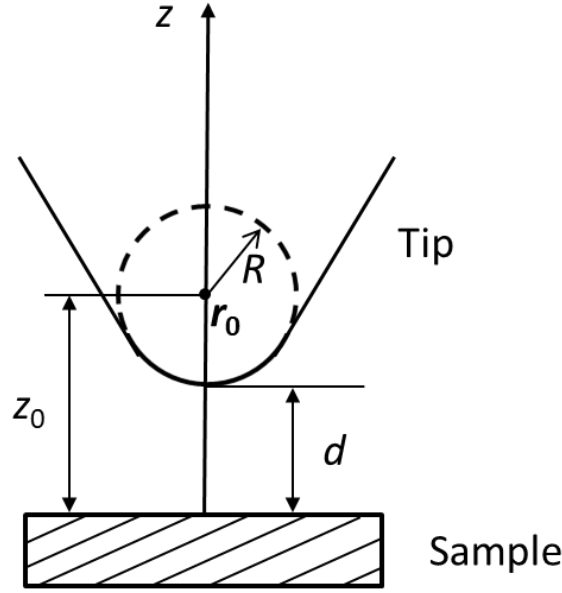


Figure 1.6 The Tersoff–Hamann model of STM. The tip is modeled as a locally spherical potential well with radius of curvature R centered at \mathbf{r}_0 . Adapted from ref [103].

For the tip wave function $\psi(\mathbf{r})$, Tersoff and Hamman assumed that it is spherically symmetrical with respect to the center of curvature \mathbf{r}_0 . Apply equation (1.29) to the tip wave function $\psi(\mathbf{r})$, we get

$$\frac{1}{r} \frac{d^2}{dr^2} [r\psi(\mathbf{r})] = \kappa^2 \psi(\mathbf{r}) \quad (1.34)$$

where $r^2 = x^2 + y^2 + (z - z_0)^2$ because $\mathbf{r}_0 = (0, 0, z_0)$ is the origin of the tip states. Up to a constant, the solution is

$$\psi(\mathbf{r}) = \frac{1}{r} e^{-\kappa r} \quad (1.35)$$

For the region $z < z_0 = d + R$, the Fourier transform of equation (1.35) is

$$\psi(\mathbf{r}) = \frac{1}{r} e^{-\kappa r} = \frac{1}{2\pi} \int d^2\mathbf{p} \frac{e^{-\sqrt{\kappa^2 + \mathbf{p}^2}(z_0 - z) + i\mathbf{p}\cdot\mathbf{x}}}{\sqrt{\kappa^2 + \mathbf{p}^2}} \quad (1.36)$$

where \mathbf{p} is the two-dimensional wave vector.

Now that the wave functions for both sample and tip are given (equations (1.33) and (1.36)), the tunneling matrix element can be estimated by (following equation (1.18))

$$M = -\frac{\hbar^2}{2m} \int_{z=0} \left[\psi \frac{\partial \varphi}{\partial z} - \varphi \frac{\partial \psi^*}{\partial z} \right] dx dy \quad (1.37)$$

Up to a constant, it is

$$M \propto \int d^2\mathbf{q} \int d^2\mathbf{p} \int d^2\mathbf{x} \left[1 + \frac{\sqrt{\kappa^2 + \mathbf{q}^2}}{\sqrt{\kappa^2 + \mathbf{p}^2}} \right] a(\mathbf{q}) e^{-\sqrt{\kappa^2 + \mathbf{q}^2} \cdot z_0 + i(\mathbf{p} + \mathbf{q}) \cdot \mathbf{x}} \quad (1.38)$$

Integration of $e^{i(\mathbf{p} + \mathbf{q}) \cdot \mathbf{x}}$ over \mathbf{x} gives a delta function $\delta(\mathbf{p} + \mathbf{q})$. Finally

$$M \propto \int d^2\mathbf{q} a(\mathbf{q}) e^{-\sqrt{\kappa^2 + \mathbf{q}^2} \cdot z_0} \quad (1.39)$$

Comparing this with equation (1.33), we found that the tunneling matrix element is proportional to the unperturbed sample wave function at the center of curvature of the tip $\mathbf{r}_0 = (0, 0, z_0)$.

$$M \propto \varphi(\mathbf{r}_0) \quad (1.40)$$

Following equation (1.12), the tunneling conductance is

$$G \equiv \frac{I}{V} \propto |\varphi(\mathbf{r}_0)|^2 \rho_{Sample}(E_F) = \rho_{Sample}(E_F, \mathbf{r}_0) \quad (1.41)$$

where $\rho_{Sample}(E_F, \mathbf{r}_0)$ is the local density of states (LDOS) of the sample at the Fermi level at the center of curvature of the tip.

If we consider applying a finite sample bias V and the tip-sample junction is under finite temperature T , following the discussion in the latter part of section 1.3.1, one can write the tunneling current as

$$I = \frac{4\pi e}{\hbar} \int_0^{eV} \rho_{Tip}(E_F - eV + \varepsilon) \rho_{Sample}(E_F + \varepsilon) |\varphi(\mathbf{r}_0)|^2 d\varepsilon \quad (1.42)$$

And the differential conductance of the tunnel junction is

$$\frac{dI}{dV} \propto \text{LDOS}(E_F + eV, \mathbf{r}_0) \quad (1.43)$$

Equation (1.43) is the major result of the Tersoff–Hamann model, and the theoretical basis for STS point spectra as well as dI/dV mapping. It states that the amplitude of the differential conductance dI/dV measured at the sample bias V is proportional to the sample LDOS at energy $E_F + eV$ at the tip position.

Chapter 2

Instrumentation

This chapter introduces the experimental instruments for my research. In addition to UHV STMs which have been used on every single day of my PhD career, a few pieces of instruments prove to be essential to the experiments.

2.1 Low-Temperature STM

The STM used for most of the experiments in this dissertation is a home-built, ultra-high vacuum (UHV) low-temperature STM (LT-STM). The base pressure of the UHV chamber is $P \sim 1 \times 10^{-10}$ torr and the base temperature of the STM is $T \sim 7$ K. The STM was originally designed and constructed by Michael F. Crommie, Wei Chen and Vidya Madhavan. Details about this STM can be found in the Ph.D. theses of Wei Chen [106], Vidya Madhavan [107], Tiberiu Jamneala [108], Michael Grobis [109], Ryan Yamachika [110], and Yen-Chia Chen [10]. Only a brief overview of this STM will be presented here.

An overview of the STM is shown in Figure 2.1. The various parts of the STM can be broken down into five categories:

1. UHV chambers
2. Cryogenics
3. Vibration isolation system
4. STM scanner
5. Electronics and software

Below gives brief descriptions on these categories.

2.1.1 UHV Chambers

The chambers and the pumping system allow the STM to operate in a base pressure of $P \sim 1 \times 10^{-10}$ torr. The chambers are made of 304 stainless steel, which can be baked to above 100 °C for more efficient outgas of the chambers, leading to a better base pressure within UHV regime. A combination of a 500 l/s turbo pump and a diaphragm-backed pumping station is used to pump the entire system. Two ion pumps, with pumping rates of 500 l/s and 150 l/s, are mounted to the analysis (preparation) chamber and the transfer (STM) chamber, respectively. Unlike turbo or diaphragm pumps, the ion pumps do not create mechanical vibrations during

operation and therefore are suitable for low-noise STM measurements. In addition, both the analysis and the transfer chambers are equipped with titanium sublimation pumps (TSPs); periodical running of the TSPs helps to keep a lower base pressure in the chambers.

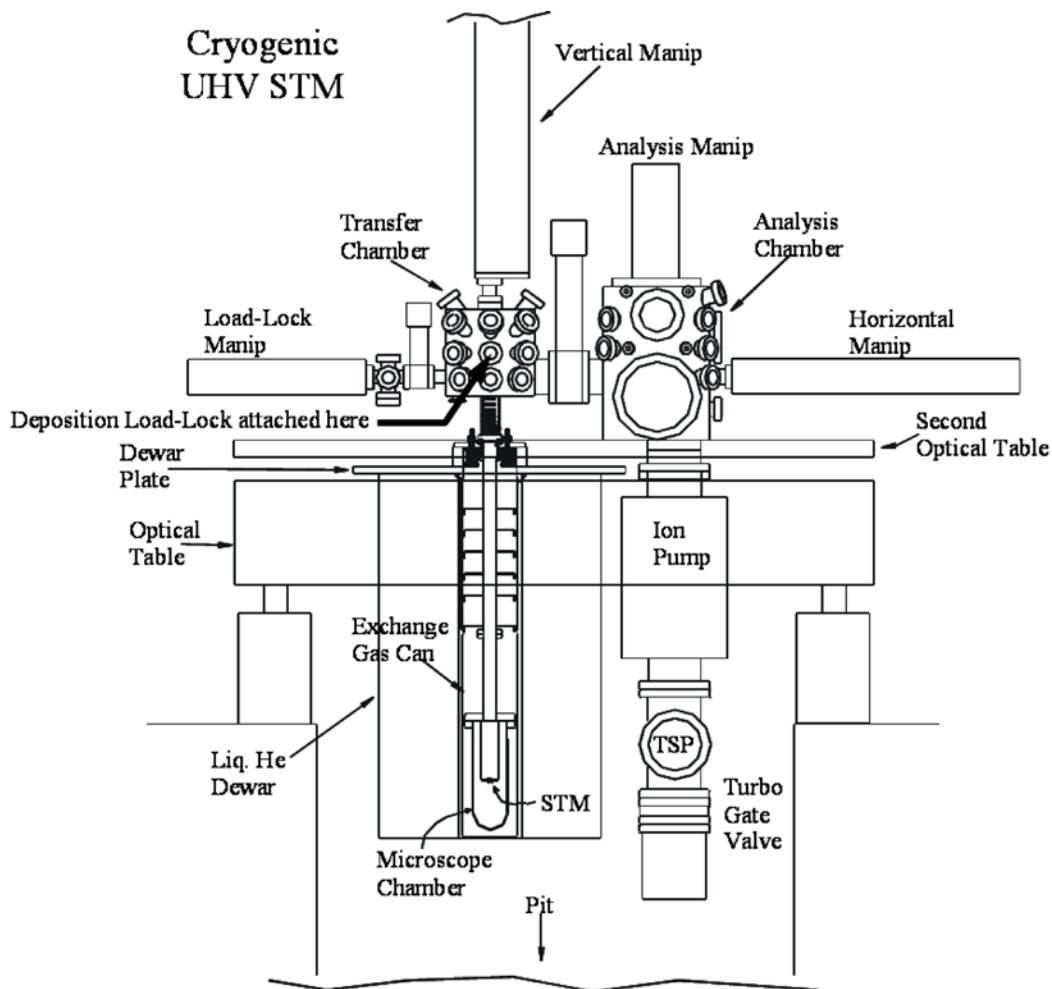


Figure 2.1 Overview of UHV LT-STM

2.1.2 Cryogenics

The STM is nominally maintained at $T \sim 7$ K by liquid helium (LHe). The microscope chamber (a bell jar) locates inside an 80-liter liquid helium dewar, which holds liquid helium for about 12 days. A He exchange gas can surrounds the microscope chamber and separates it from the helium gas vaporized from the LHe dewar. The He gas pressure in the exchange gas can is usually maintained in the range of 3 – 9 milli torr. The purpose of the He exchange gas can is threefold: (1) to minimize the vibration from LHe boiling off, (2) to avoid the pressure range of

~100 milli torr where high voltage arching occurs (Paschen's law), and (3) to control the operating temperature of the STM by controlling exchange gas pressure and thus heat transfer. The exchange gas can is designed to include a series of radiation shields to reduce the effect of thermal radiation from the transfer chamber, which is at room temperature. The wires in the exchange gas can are stainless steel coaxial cables. Their thermal conductivity is low and therefore is used to connect from connectors at room temperature to electrical feedthroughs on the microscope chamber at low temperature.

2.1.3 Vibration Isolation System

Vibration isolation is critical to STM measurements, and extensive care has been taken to reduce vibrational coupling to the STM. The UHV chambers are mounted on a dual stage optical table with vibrational isolation legs for each stage. By pumping compressed air gas in (out of) these vibrational isolation legs, the stages will become decoupled (coupled) to ground vibrations. A bellows of low spring constant at the bottom of the transfer chamber also helps decouple the two stages. The microscope chamber is suspended by two bellows that allow for acoustic mismatch between the microscope chamber and the transfer chamber. The entire UHV system locates in a soundproof room, which helps minimize acoustic noise. Under such conditions for vibration isolation, high-quality images can be routinely acquired with a tunneling current of ~1 pA.

2.1.4 STM Scanner

The STM scanner utilizes a piezoelectric tripod design, in which the fine displacements of a metallic tip along the X-, Y-, and Z- directions are actuated by three independent piezoelectric ceramics (Figure 2.2). A Pt-Ir (80:20) tip is shielded and enclosed in a Macor scanner body. The tripod scanner is supported by a machined Macor piece, which rests on a body piezo responsible for the course motion of the STM tip. The entire construction is called the "bug". Fine (50 μm) gold wires are employed to bring electrical contact to the tip, the tip shield and the piezo ceramics. The "bug" is placed on a walker plate, which includes four separate electrodes sandwiched between two thin glass plates (75 μm thick). The "bug" can be electrostatically clamped to the walker plate when a high voltage (~ 500 V) is applied between the "bug" and the electrodes. This clamping mechanism and the contraction/expansion of the body piezo controlled by an applied voltage combine to drive coarse motion of the bug along the walker plate. Details about how to construct the bug can be found in the appendix to Ryan Yamachika's Ph.D. thesis [110].

2.1.5 Electronics and Software

The electronic components of the STM consist of both home-built and commercial devices. Home-built electronics include the Z-box (the feedback circuit and the $\pm Z$ piezo voltages), the XY-box (+X and +Y piezo voltages for scanning), the field emission box (tip bias and voltage modulation), the walker box (coarse motion of the “bug”), and the ground breaking box (separation of the electrical grounds inside and outside the soundproof room). Commercial electronics include an Ithaco 1211 current-to-voltage pre-amplifier, an Electronic Development Corporation 522 power supply (tip bias), and two data precision 8200 power supplies (-X and -Y piezo voltages for lateral tip movement). For spectroscopy purpose a HP 33120A function generator and a Princeton Applied Research lock-in amplifier are used. A LakeShore 340 temperature controller helps to heat up the STM (mostly used to warm up the STM to ~ 40 K to remove hydrogen accumulated on surface over time, or in preparation for a system maintenance).

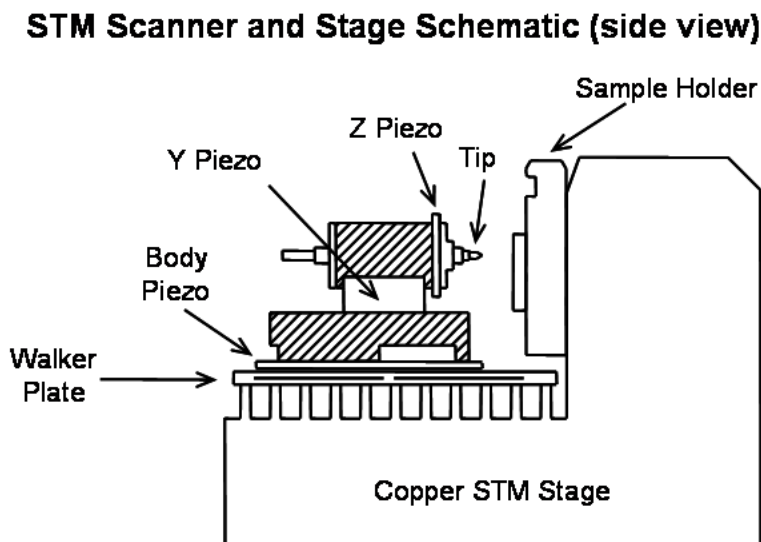


Figure 2.2 STM stage and scanner. The X piezo lies directly behind the Y piezo in this view and cannot be seen in the diagram. The sample receiver (the part that holds the sample holder) is not shown in the diagram.

A home-written C++ software controls the STM electronics, through the National Instruments PCI-6052E and NI PCI-MIO-16-XE data acquisition (DAQ) cards and a GPIB card on a computer. The software was developed in Microsoft Visual C++ 6.0 and the Microsoft Foundation Class (MFC) was used for the graphical user interface. Nate Jenkins wrote most of this software with help from Mike Grobis. Yuri Zuev, Ryan Yamachika, Xiaowei Zhang, and Yen-Chia Chen have debugged and added new features to the software.

As I became more and more familiar with the electronics and software of this LT-STM during my PhD, it became clear that this system does not have much advantage compared to state of the art commercial electronics and software packages such as Nanonis from Specs or R9 from RHK. In the spring of 2015, we actually had a test run with R9 control system; the STM scan and dI/dV measurements worked reasonably well, although tip approaching became a problem due to the unique design of the “bug”. We ended up not purchasing R9 from RHK. At the time I am writing this dissertation, there is an on-going effort to apply for funding to replace the current electronics with a Nanonis control system from Specs. Given that almost all the other STMs in our group are using Nanonis, it will be beneficial to make the transition.

2.2 Room-Temperature STM

An STM that operates at room temperature (RT) has also been used for the work in this dissertation. It is a commercial variable-temperature STM (VT-STM) system from Omicron NanoTechnology GmbH (now Scienta Omicron), with SCALA electronics for instrument control/data acquisition. Although it is capable of conducting measurements at cryogenic and elevated temperatures, we only use it at RT. Compared with the LT-STM, the RT-STM is faster in terms of sample preparation and imaging. Therefore it is more suitable for early exploratory trials, in order to go through a number of potential interesting systems and determine optimal parameters for growth procedures.

A few modifications to the RT-STM system were carried out during my PhD career, including a tweak to the STM circuits to replace the default internal pre-amplifier with an external Femto pre-amplifier, changing the default heater stage controller to separate high voltage supply and DC current supply, and adding a retractable thermocouple for directly measuring the temperature of a sample surface. More details can be found in Section 2.2 of Yen-Chia Chen’s dissertation [10].

Many efforts were taken to maintain the normal operation of the RT-STM. Among them, replacing defective wobble stick and push pull mechanism were relatively straightforward and pain-free, whereas fixing electrical short circuits inside the ion pump caused much more trouble due to difficulties in removing the pump and ergonomic issues. Recently, Dr. Gaoqiang Wang was able to fix a short circuit that prevented the course movement of the STM tip in a particular lateral direction.

2.3 Evaporator Cells

Evaporator cells are critical to our research projects because we need to sublime organic molecules in UHV all the time. The particular design we utilize is called a Knudsen cell. Basic parts of a Knudsen cell include a crucible, a heating filament, and a thermocouple to measure the

temperature of the cell. Heat shields and orifice shutters are also often seen in the design of a Knudsen cell. Figure 2.3 depicts a home-built Knudsen cell. This Knudsen cell design was introduced by Dr. Shaul Aloni to our group; it has been used to deposit a variety of molecules as well as NaCl thin films at operating temperatures 80 – 600 °C with corresponding filament currents 0.7 – 4.0 A. Although not depicted here, a thermal shield and an optional shutter are also part of the design (see Michael Grobis’s PhD thesis [109] for building of the Knudsen cell).

As the scope of chemistry accessible to us expanded and number of precursor molecules grew, it was desirable to deposit more than one molecule for a single experiment. This led us to design and build dual-cell evaporators that are easy to assemble, robust, and provide reliable temperature readings within the crucible. The schematic in Figure 2.4 shows the design of such a dual-cell evaporator. It was adapted from the design of Dr. Luca Floreano (a senior scientist at the beamline ALOISA in the ELETTRA synchrotron in Trieste, Italy) and introduced into our lab by postdoc Dr. Dimas G. de Oteyza. Details on how to build this type of evaporator can be found in the appendix of Yen-Chia Chen’s PhD thesis [10].

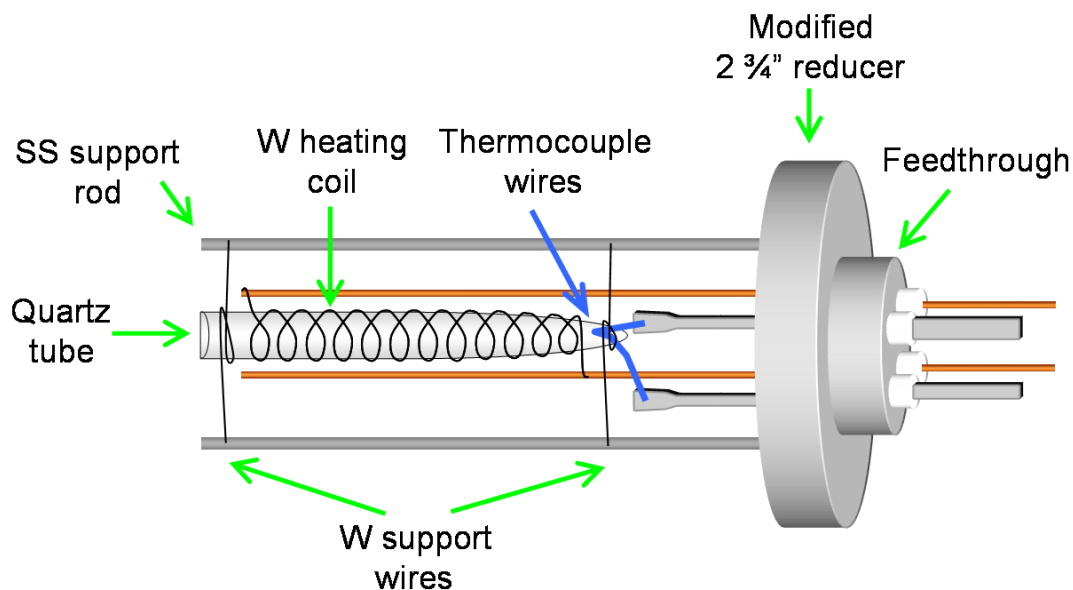


Figure 2.3 A Knudsen cell evaporator

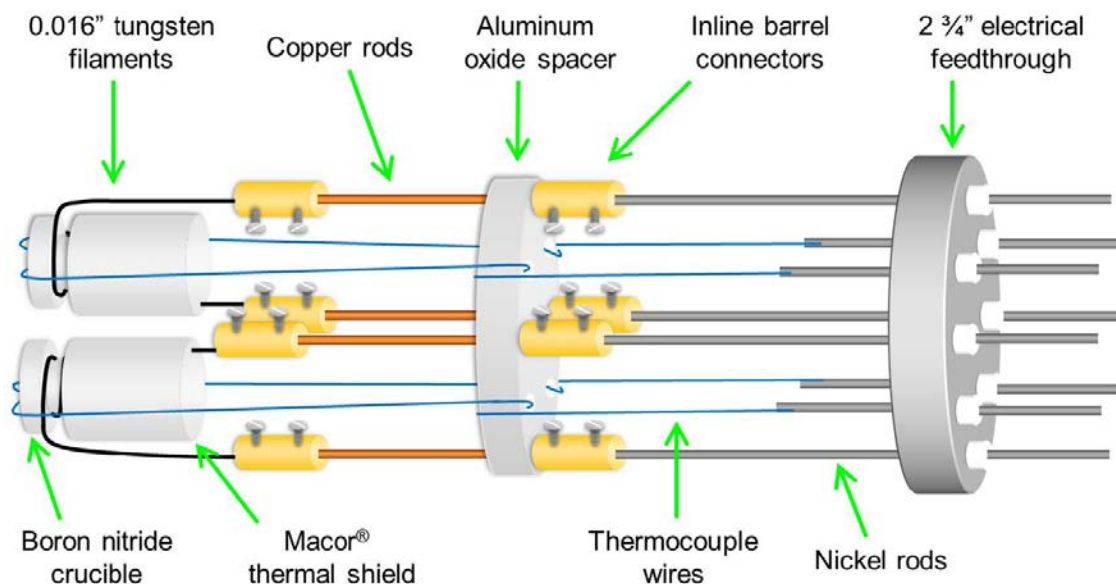


Figure 2.4 A dual-cell evaporator

2.4 Quartz Crystal Microbalance

A quartz crystal microbalance (QCM) measures the change in the resonant frequency of a quartz crystal resonator when some material adheres to it, and translates the signal to a thickness of the material layer. In our molecule-related projects, a QCM was often used to find appropriate temperatures for sublimation of molecules in UHV. The QCM is mounted on a linear motion drive, which is in turn mounted directly on the UHV chamber. It can be extended and exposed under molecular flux (usually facing an evaporator cell) during use, and fully retracted to avoid crashing with other vacuum parts after use. Around 30 minutes is usually needed for the QCM to stabilize after turning on its controller. We then gradually increase the filament current to raise the temperature of a Knudsen cell. If a molecule is starting to evaporate and deposit on the quartz crystal resonator, the displayed thickness will accumulate, and we can thus determine the evaporation temperature of the molecule. Most of the time we want to deposit molecules onto metallic substrates instead of a quartz crystal, therefore the use of QCM is not completely reliable for certain molecules, and we have to use STM to verify the successful deposition of those molecules.

Chapter 3

Graphene Nanoribbons

This chapter discusses about my work on graphene nanoribbons (GNRs), which are quasi-one dimensional strips of graphene. The researchers who contributed to these studies are Chen Chen, Zahra Pedramrazi, Ting Cao, Fangzhou Zhao, Dr. Yen-Chia Chen, Dr. Dimas G. de Oteyza, Dr. Danny Haberer, Dr. Giang D Nguyen, Daniel J Rizzo, Trinity Joshi, Dr. Christopher Bronner, Dr. Hsin-Zon Tsai, Dr. Arash A. Omrani, Dr. Francesca Toma, Dr. Ryan Cloke, Dr. Wade Perkins, Dr. Rebecca Durr, Dr. Tomas Marangoni, Won-Woo Choi, Dr. Felix Fischer, Dr. Steve G. Louie, and Dr. Michael F. Crommie.

When I first joined the Crommie group in the winter of 2012, the field of bottom-up graphene nanoribbons was just starting to develop and there were not many experimental groups in it. Over the years, we witnessed lots of monumental development in this field, including but not limited to: tuning the band gap of armchair GNR (AGNR) by changing the width [111], realization of GNR heterojunctions of type I [9] and type II [112], successful synthesis of a zigzag GNR (ZGNR) [113], tuning the electronic structure by insertion of heteroatoms at the edge [114-116] and backbone [117, 118] of GNRs, and more recently, topological band engineering of GNRs. There is great interest in the possibilities of GNRs being used for commercial electronic applications in the future.

3.1 Molecular Bandgap Engineering in 7-13 Armchair GNR

Heterojunction

The successful synthesis and characterization of N=13 AGNR by the Berkeley group was a significant development in the field of bottom-up GNRs, showing that bandgap engineering of GNRs from molecular precursors was completely feasible [111]. With both precursor molecules for N=7 AGNR and for N=13 AGNR in hand, we found that these two molecules are chemically compatible and in principle can be connected in the same fashion as either type of precursor is connected among themselves (a more technical term describing the chemistry would be “Ullmann-type coupling”). This work was originally published in “Nature Nanotechnology” [9].

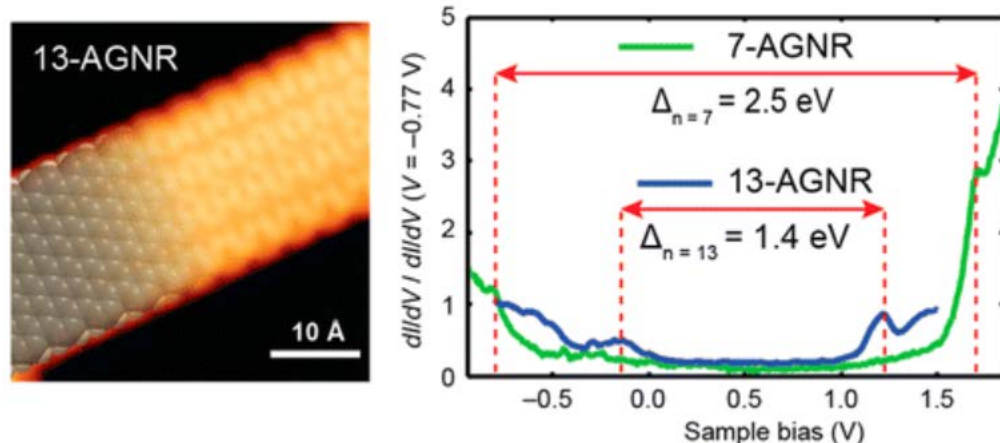


Figure 3.1 Comparison of bandgap between N=13 AGNR and N=7 AGNR. N=13 AGNR has a bandgap of 1.4 eV, compared to a bandgap of 2.5 eV for N=7 AGNR, thus confirming the feasibility of bandgap engineering of GNRs from molecular precursors. Taken from ref [111].

3.1.1 Bottom-up Synthesis and Local Characterization of Electronic States

7-13 AGNR heterojunctions were fabricated by combining the molecular building blocks 10,10'-dibromo-9,9'-bianthracene (1) and 2,2'-di((1,1'-biphenyl)-2-yl)-10,10'-dibromo-9,9'-bianthracene (2). As shown in Figure 3.2, molecules 1 and 2 are precursors to N = 7 and N = 13 AGNRs, respectively (referred to as 7-AGNRs and 13-AGNRs), where N is the width in number of rows of carbon atoms across the GNR.^[ref] The building blocks were thermally evaporated onto a Au(111) surface held at room temperature in UHV. The surface was then heated to 470 K for 10 min to induce homolytic cleavage [119] of the labile C–Br bonds in building blocks 1 and 2, yielding surface stabilized diradical intermediates. Because 1 and 2 share the same bianthracene backbone, their diradical intermediates are structurally complementary and are able to colligate into linear polymers. On further heating to 670 K for 10 min, a stepwise cyclization/dehydrogenation sequence converted these linear polymers into 7-13 AGNR heterojunctions (Figure 3.2). The samples were then cooled to 7 K for STM and STS measurements. Figure 3.2(b) presents an STM topographic image of a representative sample, showing 7-13 AGNR heterojunctions with shapes resembling the sketch in Figure 3.2(a). The narrower segments in these heterojunctions are 1.3 ± 0.1 nm in width in the STM image and are composed of covalently bonded monomers of 1 (N = 7). The wider segments measure 1.9 ± 0.2 nm in apparent width and consist of bonded monomers of 2 (N = 13). As the building blocks mixed and fused in a random sequence during the initial step-growth polymerization, various N = 7 and N = 13 segment lengths were observed (Figure 3.2(B), inset).

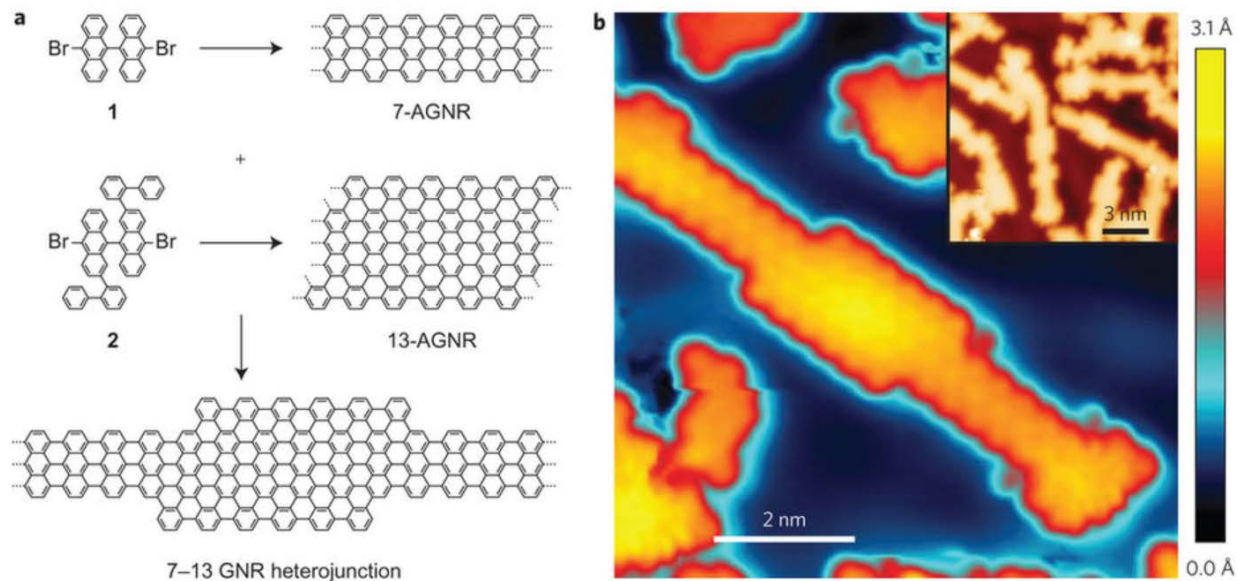


Figure 3.2 Bottom-up synthesis of 7-13 AGNR heterojunctions. (a) Synthesis of 7-13 AGNR heterojunctions from molecular building blocks 1 and 2. (b) High-resolution STM topograph of a 7-13 AGNR heterojunction (sample voltage $V_s = 60$ mV, tunneling current $I_t = 200$ pA). Inset: Larger-scale STM image of multiple GNR heterojunctions, showing a variety of segment lengths ($V_s = 0.50$ V, $I_t = 2$ pA).

To investigate the local electronic structure of these 7-13 AGNR heterojunctions, tunneling conductance dI/dV spectra were recorded while placing the STM tip at different positions above the heterojunctions (the magnitude of dI/dV reflects the energy-dependent LDOS at the STM tip position). As a background reference, a dI/dV spectrum taken on bare Au(111) is shown in green in Figure 3.3. A characteristic spectrum (blue curve, Figure 3.3) recorded at a specified position on an $N=7$ segment of a single heterojunction (see image in Figure 3.3 inset) exhibits a pronounced shoulder at $V_s = 1.86 \pm 0.02$ V (labeled state 1) and a peak at $V_s = -0.90 \pm 0.02$ V (where V_s is the sample voltage). In contrast, the marked $N=13$ segment (red curve) shows prominent peaks at $V_s = 1.45 \pm 0.02$ V (labelled state 2) and $V_s = -0.12 \pm 0.02$ V. The energy locations of these states are similar to the valence and conduction band-edges reported previously for isolated 7-AGNRs and 13-AGNRs on Au(111) [111, 120]. Additional states are observed in dI/dV spectra measured at positions near the interface between the $N=7$ and $N=13$ segments of a heterojunction. The black curve in Figure 3.3, obtained at the interface position marked by the black cross in the inset to Figure 3.3, exhibits two additional overlapping peaks labelled as states 3 and 4. Lorentzian peak-fitting yields peak positions for states 3 and 4 of $V_s = 1.25 \pm 0.02$ V and $V_s = 1.13 \pm 0.02$ V, respectively. These spectroscopic features were consistently observed on all ten GNR heterojunctions whose nanoribbon segments and interfaces

were inspected via dI/dV tunneling spectroscopy using different STM tips (all heterojunctions inspected via dI/dV had both $N = 7$ and $N = 13$ segments composed of at least two monomer units each; that is, segment lengths ≥ 1.6 nm).

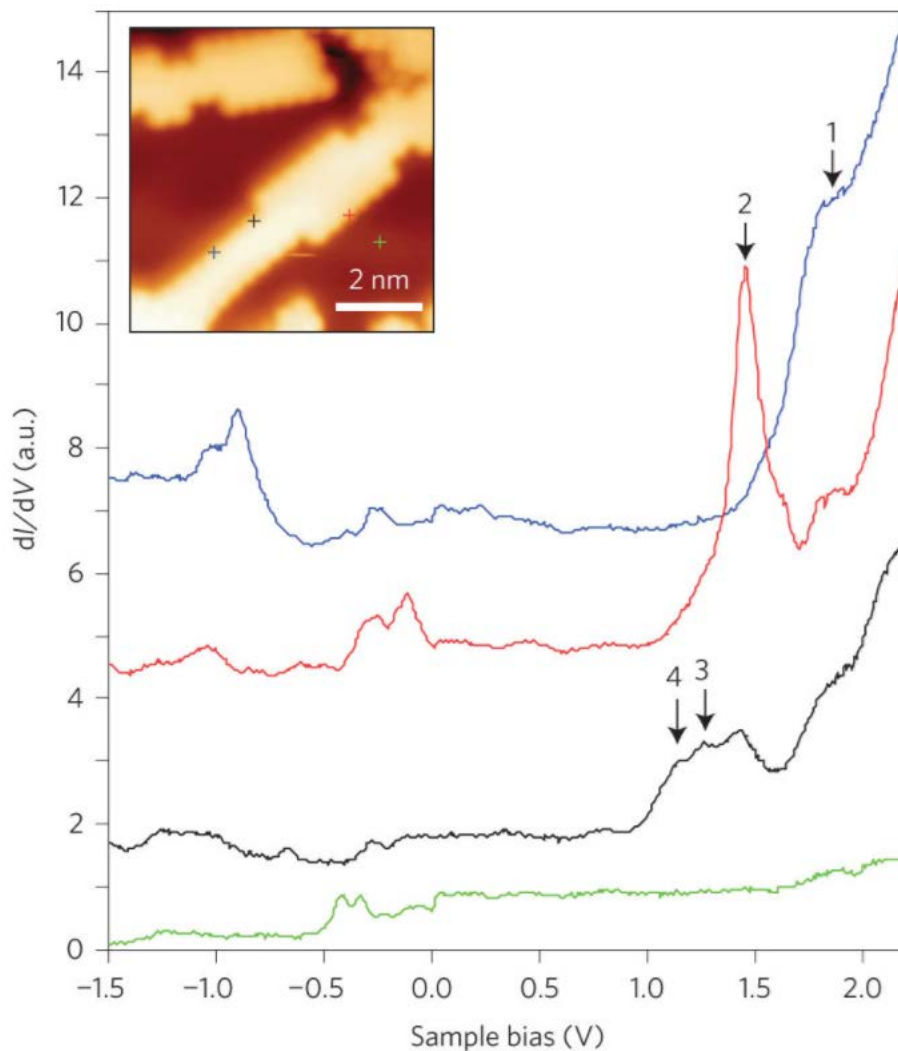


Figure 3.3 STM dI/dV spectroscopy of 7-13 AGNR heterojunction electronic structure. Blue curve: dI/dV spectrum acquired on the narrow $N = 7$ segment of a 7-13 AGNR heterojunction. Red curve: Spectrum acquired on the wider $N = 13$ segment. Black curve: Spectrum acquired at the interface region between $N = 7$ and $N = 13$ segments. Green curve: Calibration spectrum acquired with tip held over bare Au(111). The tip locations for these spectra are marked in the inset as color-coded crosses. All spectra were acquired with the same STM tip. The black, red and blue curves are vertically offset by 1, 4 and 6 arbitrary units, respectively, for clarity (open-feedback parameters: $V_s = 1.00$ V, $I_t = 35$ pA, modulation voltage $V_{rms} = 10$ mV). Resonant peaks showing the locations of four GNR heterojunction states in the unoccupied

region are labelled 1–4. Inset: STM topograph of the 7-13 AGNR heterojunction measured to obtain this series of dI/dV spectra ($V_s = 0.10$ V, $I_t = 95$ pA).

The spatial distributions of GNR heterojunction states 1-4 were explored experimentally using dI/dV mapping (Figure 3.4(a)-(d)). Figure 3.4(a) shows the dI/dV map obtained for the highest-energy state (state 1) at $V_s = 1.86$ V for the same heterojunction as shown in the inset to Figure 3.3. The dI/dV map of state 1 exhibits significant LDOS at the edges of the narrower $N=7$ segment and some LDOS at the edges of the wider $N=13$ segment. Figure 3.4(b) shows the dI/dV map obtained at the energy of state 2 ($V_s = 1.45$ V). This lower-energy state shows significant LDOS near the edges of the wider $N=13$ heterojunction segment, but no LDOS in the narrower $N=7$ segment. Figure 3.4(c) shows the dI/dV map of state 3 at $V_s = 1.25$ V. This even lower-energy state exhibits significant LDOS at the corners of the interface between the $N=7$ and $N=13$ segments, as well as some LDOS at the outer edges of the wider $N=13$ segment. Figure 3.4(d) shows the dI/dV map of state 4, the lowest energy peak for the unoccupied states, at $V_s = 1.15$ V. This state exhibits LDOS localized to the corners of the interface between the $N=7$ and $N=13$ regions, but very little LDOS anywhere else.

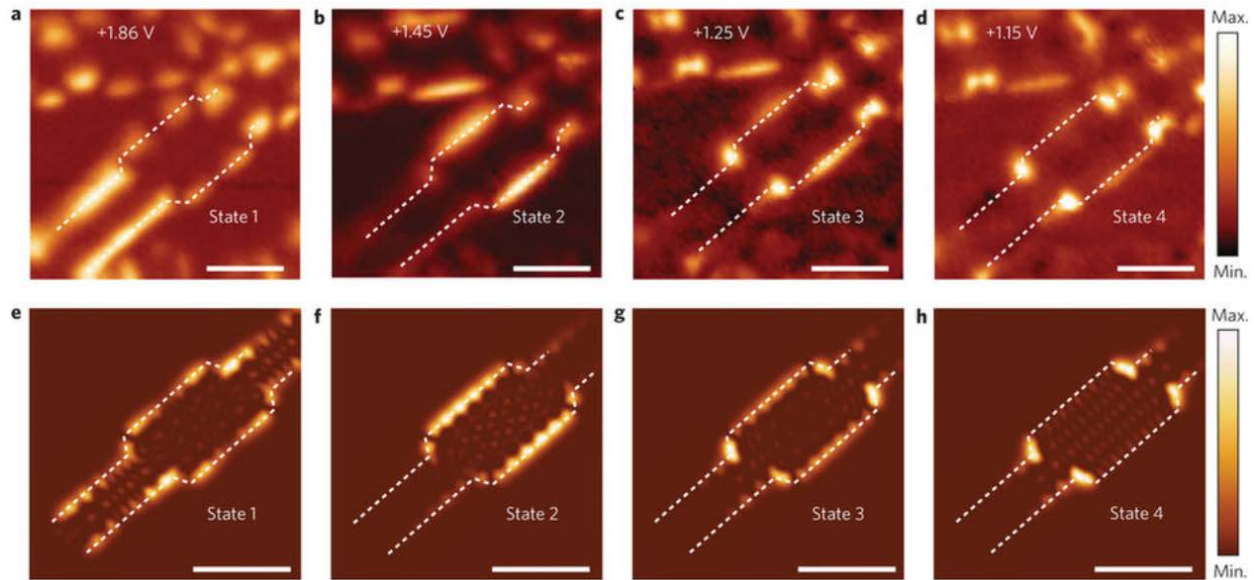


Figure 3.4 Comparison of experimental dI/dV maps and theoretical LDOS for a 7-13 AGNR heterojunction. (a)-(d) Experimental dI/dV spatial maps recorded at the energies of spectroscopic peaks 1-4 for the 7-13 GNR heterojunction shown in the inset to Figure 3.3 ($I_t = 35$ pA; modulation voltage $V_{rms} = 10$ mV). Dashed lines are drawn at the mid-height topographic position of the edges of the 7-13 GNR heterojunction. (e)-(h) DFT-calculated LDOS maps of states 1-4 calculated at a height of 4 \AA above a 7-13 GNR heterojunction. Dashed lines

are drawn at a distance equal to one carbon dimer-dimer spacing (1.2 \AA) outside the 7-13 GNR heterojunction carbon atom border. All scale bars, 2 nm.

The overall electronic structure of 7-13 AGNR heterojunctions shows some features that can be intuitively understood. For example, the fact that the highest-energy unoccupied state (state 1) shows LDOS in both the narrower and wider segments while the adjacent, lower-energy state (state 2) shows significant LDOS only in the wider segment is consistent with a simple quantum well picture. Other features, however, are harder to understand. The origins of interface states 3 and 4, for example, are not intuitive within the quantum well picture. Moreover, the fact that GNR heterojunctions exhibit high LDOS intensity at their edges but not in their interiors (similar to previously reported pristine 7- and 13-AGNRs [111, 120-122]) conflicts with previous theoretical predictions that there are no localized edge-states in AGNRs near the band-edges [5].

3.1.2 Theoretical Calculations and Comparison to Experimental Results

To better understand the properties of 7-13 AGNR heterojunctions, we used first-principles density functional theory (DFT) within the local density approximation (LDA) to calculate their electronic structure. We note that LDA tends to underestimate energy gaps, but here this is offset by the strong metallic screening of the substrate. The simulation was based on the isolated 7-13 junction structure shown in the inset to Figure 3.5(a) (all edges were terminated by hydrogen atoms, consistent with the experiment). The resulting density of states (DOS) is plotted in Figure 3.5(a), with a Gaussian broadening of 0.06 eV (states localized at the two ends of the structure [5, 123] were removed from the plot because we probed regions far from the ends of the GNR heterostructures). The four lowest unoccupied states are numbered 1 to 4 in descending order of energy, analogous to the labeling of the resonant states observed experimentally (Figure 3.3). Out-of-plane height-integrated (h -integrated) LDOS plots (Figure 3.5(b)-(e)) provide detailed information regarding the averaged planar (x - y) spatial distribution of these four calculated states. The lower-energy states 2, 3 and 4 are localized mainly on the wider $N = 13$ segment and can be understood as confined states in a potential well, with the adjacent and narrower $N = 7$ segments acting as energy barriers. The highest-energy state 1 extends over the entire heterojunction, including both the wide $N = 13$ and narrow $N = 7$ segments. All four states show significant intensity in the interior of the heterojunction and there are no localized edge states (as expected for armchair-edged GNR structures) [5, 6]. This appears to be in contradiction with the experimental dI/dV maps depicted in Figure 3.4(a)-(d), where only the edges exhibit LDOS noticeably higher than the background.

We are able to resolve this apparent contradiction by examining the height dependence of the calculated 7-13 AGNR heterojunction LDOS as opposed to the height-integrated quantities. This is shown by the simulated dI/dV maps in Figure 3.5(g)-(i), which illustrate the height dependence

of the LDOS for one particular state (state 2) at different distances h above the GNR heterojunction. At a height of $h = 2 \text{ \AA}$ above the carbon plane (Figure 3.5(g)), the LDOS appears rather uniformly distributed across the $N = 13$ segment, resembling the height-integrated LDOS shown in Figure 3.5(c). However, as one moves higher above the carbon plane, the heterojunction edges begin to exhibit more intense LDOS than the interior (Figure 3.5(h),(i)), to the point where the edges completely dominate the LDOS at a height of $h = 4 \text{ \AA}$ above the carbon plane (Figure 3.5(i)). Simulated dI/dV maps at even greater distances appear similar to Figure 3.5(i). This type of behavior was observed for all four of the calculated quantum well states of the heterojunction. As our STM tip is located $\sim 5 \text{ \AA}$ above the carbon plane of the GNR heterojunctions during dI/dV mapping (estimated via the tunnel junction resistance at the open-feedback set points), the experimental dI/dV maps should be directly compared with the theoretical LDOS calculated in a plane above the heterojunction. Indeed, the calculated LDOS of heterojunction states 1-4 at a height of 4 \AA above the carbon plane (Figure 3.4(e)-(h)) match the corresponding experimental dI/dV maps very well (Figure 3.4(a)-(d)).

The strong dependence of the LDOS distribution with height h can be explained by the difference in potential energy felt by electrons at different (x, y) positions above a GNR heterojunction, as shown in Figure 3.5(f). The red curve in Figure 3.5(f) shows the calculated potential energy difference (within LDA) between positions A1 and A2 in the $N = 7$ segment (marked in the inset structural drawing) as a function of height. A1 marks a carbon atom at the very edge of the segment and A2 marks an adjacent carbon atom just one dimer row into the interior. The potential energy at the edge is lower than the potential energy in the interior for heights greater than 1.6 \AA above the GNR heterojunction. This implies a smaller out-of-plane (h direction) potential barrier in the vacuum for electrons closer to the edge. The wave function at the edge therefore decays more slowly along the h direction into the vacuum than the wave function in the interior, resulting in higher LDOS contrast between the edges and the interior, as shown in Figure 3.5(i) (see Figure 3.5(f) inset). The same argument also applies to the $N = 13$ segment (green curve in Figure 3.5(f)). The stronger spectroscopic dI/dV signal observed near the edges of armchair GNRs is thus attributed to spatial variation in the electronic potential, even though the states themselves are not localized to the edges.

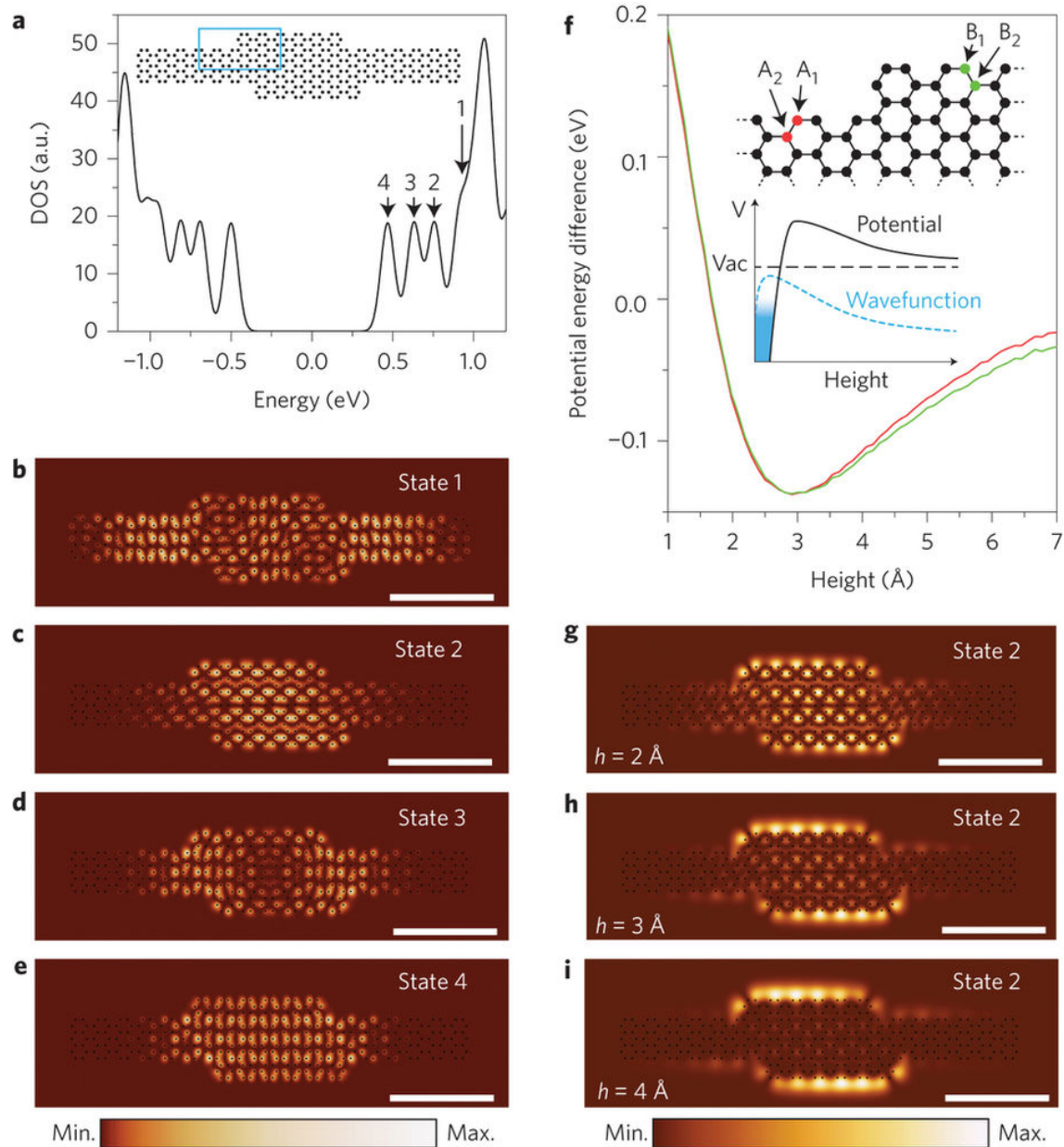


Figure 3.5 Theoretical electronic structure of 7-13 AGNR heterojunction. (a) Calculated DOS of the isolated 7-13 AGNR heterojunction structure shown in the inset, with a Gaussian broadening of 0.06 eV. Four unoccupied states are labeled 1-4 in the figure (states here are labeled analogous to the peaks observed experimentally; Figure 3.3). (b)-(e), Height-integrated LDOS maps of theoretical states 1-4 for the 7-13 AGNR heterojunction. The plots are normalized with respect to their maximum intensities (270, 348, 500 and 416 arbitrary units in (b)-(e), respectively). (f) Calculated electron potential energy difference between edge and inner atoms as a function of height h above the carbon plane of the 7-13 AGNR heterojunction. The

red curve shows the potential energy difference between atomic positions A1 and A2 (see upper inset). The green curve shows the potential energy difference between atomic positions B1 and B2 (see upper inset). The inset structural drawing depicts the boxed region in the inset to (a). Lower inset: Height dependence of the potential at one atomic location and the resulting decay of the wave function along the surface normal into the vacuum. The horizontal black dashed line indicates the vacuum energy level. Blue shading represents electron filling relative to the vacuum energy level. (g)-(i) Calculated LDOS of 7-13 AGNR heterojunction state 2 at heights of 2 Å (g), 3 Å (h) and 4 Å (i) above the plane of the GNR heterojunction. The LDOS plots are normalized with respect to their maximum intensities (180, 9.05 and 0.84 arbitrary units in (g)-(i), respectively). All scale bars, 2 nm.

3.1.3 Summary

These results imply that the band alignment in 7-13 AGNR heterojunctions is very similar to type I semiconductor junctions, because the lowest unoccupied (highest occupied) state in the $N=13$ segment is lower (higher) than that in the $N=7$ segment. Such spatially varying energy gap size is a hallmark of bandgap engineering and is different, for example, from the band offsetting that leads to p-n-type junctions [112]. The $N=7$ segment might therefore serve as an energy barrier for charge carriers trapped in the $N=13$ segment (our spectroscopic data suggest that the energy required to excite an electron from state 4, which is localized in the $N=13$ segment, to state 1 and thus into the $N=7$ segment, is ~ 0.7 eV). This provides a possible means for constructing graphene quantum-dot-based systems with sub-nanometer feature sizes and single-atom thickness. A potential benefit of this heterojunction architecture is that electrical contacts to the quantum dots are readily available via the outer GNR segments. Bottom-up GNR-based synthesis methods thus have potential for creating functional gap-modulated semiconductor junctions with atomically controlled features that are smaller than possible through conventional top-down lithography.

3.2 Concentration Dependence of Dopant Electronic Structure in

Boron-doped $N=7$ AGNR

The success of bottom-up syntheses of GNRs opened up new possibilities of inserting non-carbon heteroatoms into GNR structures by rational designs of molecular precursors. Efforts to utilize this principle have been carried out by different groups and different heteroatoms have been incorporated in an atomically-precise fashion, including nitrogen [112, 114], sulfur [115], oxygen [116], and boron [117, 118]. The boron-substituted $N=7$ AGNR, in particular, has a pair of boron atoms incorporated in the center of the GNR backbone for every unit cell. From a

chemistry standpoint, the empty p -orbitals of the boron atoms are in conjugation with the extended π -system of the 7-AGNR, and should therefore alter the electronic structure of pristine N=7 AGNR significantly.

In this study, we managed to fabricate Boron-doped N=7 AGNRs with different dopant concentration by a combination of pristine and doped GNR precursors, and determined how the dopant electronic structure evolves with increasing dopant density. Moreover, we discovered an unusual hybridization between the dopant states and the Au(111) surface, with the dopant-surface interaction strength dictated by the dopant orbital symmetry. This work is under review at “Nano Letters” at the time of this writing.

3.2.1 Concentration-Dependent Dopant Electronic Structure

Figure 3.6 shows a DFT calculation (within LDA) of the electronic structure of a freestanding N=7 AGNR (i.e., no substrate included in the calculation) for three boron dopant concentrations: (i) the undoped case (Figure 3.6(d)), (ii) the dilute doped limit (Figure 3.6(e)), and (iii) the densely doped limit (Figure 3.6(f)) (Figure 3.6(a)-(c) show the unit cells used for the three calculations). GW [8] calculations were seen to give similar results but with larger bandgap values due to self-energy effects [7, 9, 124]. We focus here on the DFT results since substrate screening typically reduces the GW bandgaps to values close to the DFT level when the system is put on a metallic surface (as done in our experiments) [9]. The undoped GNR band structure shows the familiar conduction (CB) and valence (VB) bands that have been calculated within DFT before [120], while the dilute-doped GNR exhibits band edges at similar energies. The most significant difference between the undoped and dilute-doped band structure is the presence of two new defect levels at ~ 0.5 eV above the VB edge for the dilute-doped case (the appearance of multiple bands above (below) the conduction (valence) band edge for the dilute-doped case is due to band-folding from the supercell geometry used in the calculation). The new impurity states are nearly degenerate ($\Delta E < 20$ meV) and exhibit a large contribution from the π -orbitals of the boron dopant atoms. Analysis of the wave function for the lower defect state shows that it has p -like symmetry (odd parity) along the GNR axial direction, while the upper defect state has s -like symmetry (even parity) along the longitudinal axis (a similar theoretical result for the dilute, freestanding limit was reported in another work [125]). As the dopant concentration increases, the energy splitting between the two impurity states correspondingly increases and the defect states evolve into impurity bands with an energy gap of 0.5 eV, as shown in the band structure for the densely-doped GNR in Figure 3.6(f).

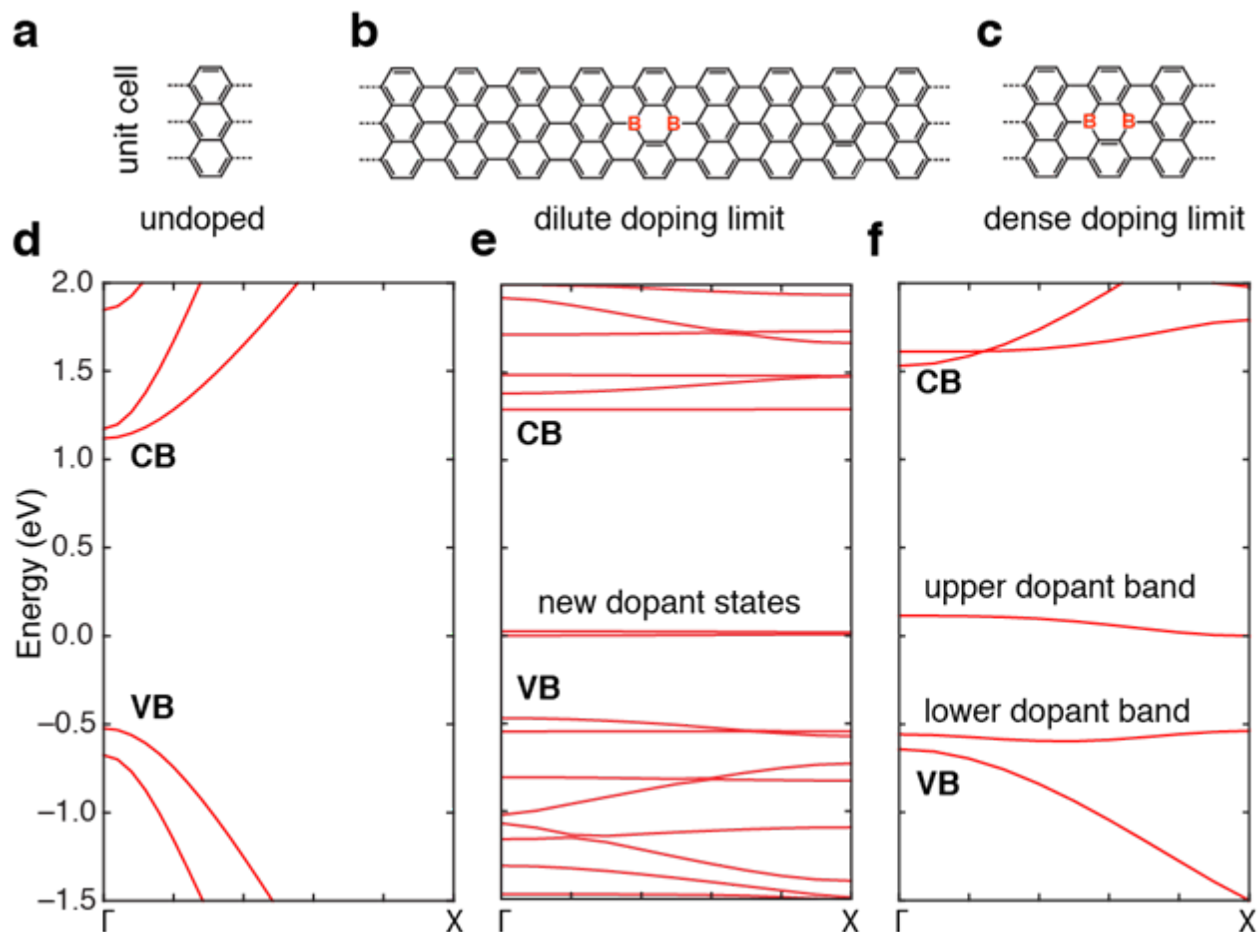


Figure 3.6 Band structure evolution of freestanding boron-doped $N=7$ armchair graphene nanoribbons at different dopant densities. Unit cells of (a) undoped, (b) dilute-doped, and (c) densely-doped $N=7$ GNRs. (d-f) corresponding band structures calculated by DFT within LDA.

3.2.2 Synthesis and Characterization of B-doped AGNRs with Different Dopant Concentrations

B-doped AGNRs were fabricated in both the dilute and dense regimes. The dilute-doped regime was accessed by combining molecular precursors for undoped $N=7$ GNR (10,10'-dibromo-9,9'-bianthryl, DBBA) with precursors for boron-doped $N=7$ AGNR [117, 118] in a 10:1 ratio using standard GNR growth conditions [15, 111] (polymerization of the precursors occurs at ~ 180 °C while cyclodehydrogenation occurs at ~ 360 °C). Figure 3.7(b) shows an STM topographic image of a resulting dilute-doped $N=7$ AGNR on Au(111) with vertical dashed lines

indicating the location of a boron defect (a sketch of the wireframe structure is shown in Figure 3.7(a)). The region surrounding the dopant atoms has a reduced apparent height in the STM image, suggesting that the boron atoms sit closer to the Au(111) surface than the GNR carbon atoms.

The experimental electronic structure of dilute-doped GNRs was investigated by dI/dV spectra at the position of boron dopants and then comparing that to spectra acquired on undoped GNR segments at the positions marked in Figure 3.7(b) (the different positions are color-coded with the dI/dV curves). Figure 3.7(c) shows a characteristic dI/dV point spectrum (green curve) recorded at the edge of an undoped segment of the GNR. This spectrum exhibits a peak at $V_s = 1.68 \pm 0.02$ V, which we identify as the CB edge, as well as a peak at $V_s = -0.80 \pm 0.02$ V which is identified as the VB edge (V_s is sample voltage). This leads to an overall GNR bandgap of 2.48 ± 0.02 eV, similar to bandgap measurements on undoped N=7 AGNRs performed previously [120, 121]. The identity of these familiar spectroscopic peaks was confirmed via energy-resolved dI/dV mapping, which allows visualization of the surface local density of states (LDOS) as depicted in Figure 3.7(d)-(g). Two new states attributed to the dopant atoms are observed in the STM spectroscopy measured at the center (top inset of Figure 3.7(c), blue curve) and edge (bottom inset of Figure 3.7(c), red curve) of the boron defect shown in Figure 3.7(b). The dI/dV spectrum measured at the impurity edge (red curve) shows the presence of a new peak (labeled State 1) that is centered at $V_s = -0.52 \pm 0.02$ V and that has a full width at half maximum (FWHM) of 0.23V. The dI/dV spectrum measured at the center of the dopant site (blue curve) exhibits a pronounced upward slope starting at $V_s \approx 0.3$ V and extending to $V_s \approx 1.2$ V that is not observed in the reference spectrum taken at the center of the undoped segment with the same tip (black curve). This second dopant-induced feature is labeled as State 2. We note that these spectroscopic features (States 1 and 2) persist even as adjacent dopants are separated by only 2.5 nm center-to-center.

The spatial distributions of dopant-induced States 1 and 2 were determined using dI/dV mapping. Figure 3.7(f) shows a dI/dV map measured at the energy of State 1 that exhibits bright lines along the edges of the dopant segment as well as two small high intensity spots near the boron atoms (the two central bright spots are located at the sites of the two horizontal boron-carbon bonds in Figure 3.7(a)). Figure 3.7(e) shows a representative dI/dV map of State 2 recorded at 0.8 V that exhibits bright, diffuse LDOS that is elliptically symmetric and centered at the position of the dopant (dI/dV maps recorded for State 2 at different energies in the range 0.3 V $<$ V_s $<$ 1.35 V show similar LDOS patterns).

closer to the substrate than the unsubstituted regions and leads to a $1.30 \pm 0.05 \text{ \AA}$ amplitude periodic height modulation along the GNR long axis in topography. We first characterized the electronic structure of densely-doped GNRs *via* dI/dV point spectroscopy. Figure 3.8(c) shows typical dI/dV spectra measured at a position along the backbone (blue curve) and at the edge (red curve) of a densely-doped GNR with the same tip (spectroscopy positions are marked in Figure 3.8(b)). The dI/dV spectrum recorded at the GNR edge shows a well-defined peak at $1.63 \pm 0.04 \text{ eV}$ above the Fermi level E_F . The spectrum recorded along the densely-doped GNR backbone is quite different and reveals a new, broad spectroscopic feature at $1.0 \pm 0.2 \text{ eV}$ above E_F (this peak is absent in STS of undoped GNRs [120-122]). We did not observe any reproducible spectroscopic features below E_F in our dI/dV point spectra for densely-doped GNRs on Au(111).

We used dI/dV mapping to visualize the electronic structure of densely-doped GNRs at different energies. Figure 3.8(d) shows a dI/dV map recorded at 1.60 eV , the energy of the upper spectroscopic peak. Here the intensity of the LDOS is highest along the GNR edges, similar to what has previously been observed for energies near the CB edge in undoped $N=7$ AGNRs [9, 118, 120, 121]. The dI/dV map obtained at an energy near the broad spectroscopic peak at 1.0 eV shows a pronounced shift in LDOS away from the GNR edges to the GNR backbone (Figure 3.8(e)). Figure 3.8(f) shows a dI/dV map obtained in the filled states at a voltage of $V_s = -0.23 \text{ V}$. Although we observe no peak at this energy in the dI/dV point spectroscopy, a clear transition is observed in the spatial LDOS distribution compared to dI/dV maps obtained at higher voltages. At this filled state energy the LDOS is pushed outwards toward the GNR edges and a longitudinal nodal structure is seen that does not appear in the map at $V_s = 1.0 \text{ V}$. The new densely-doped spectroscopic features observed at $V_s = -0.23 \text{ V}$ and $V_s = 1.0 \text{ V}$ do not occur for undoped $N = 7$ AGNRs, and so must arise from the influence of boron dopants. We label them here as State A ($V_s = -0.23 \text{ V}$) and State B ($V_s = 1.0 \text{ V}$).

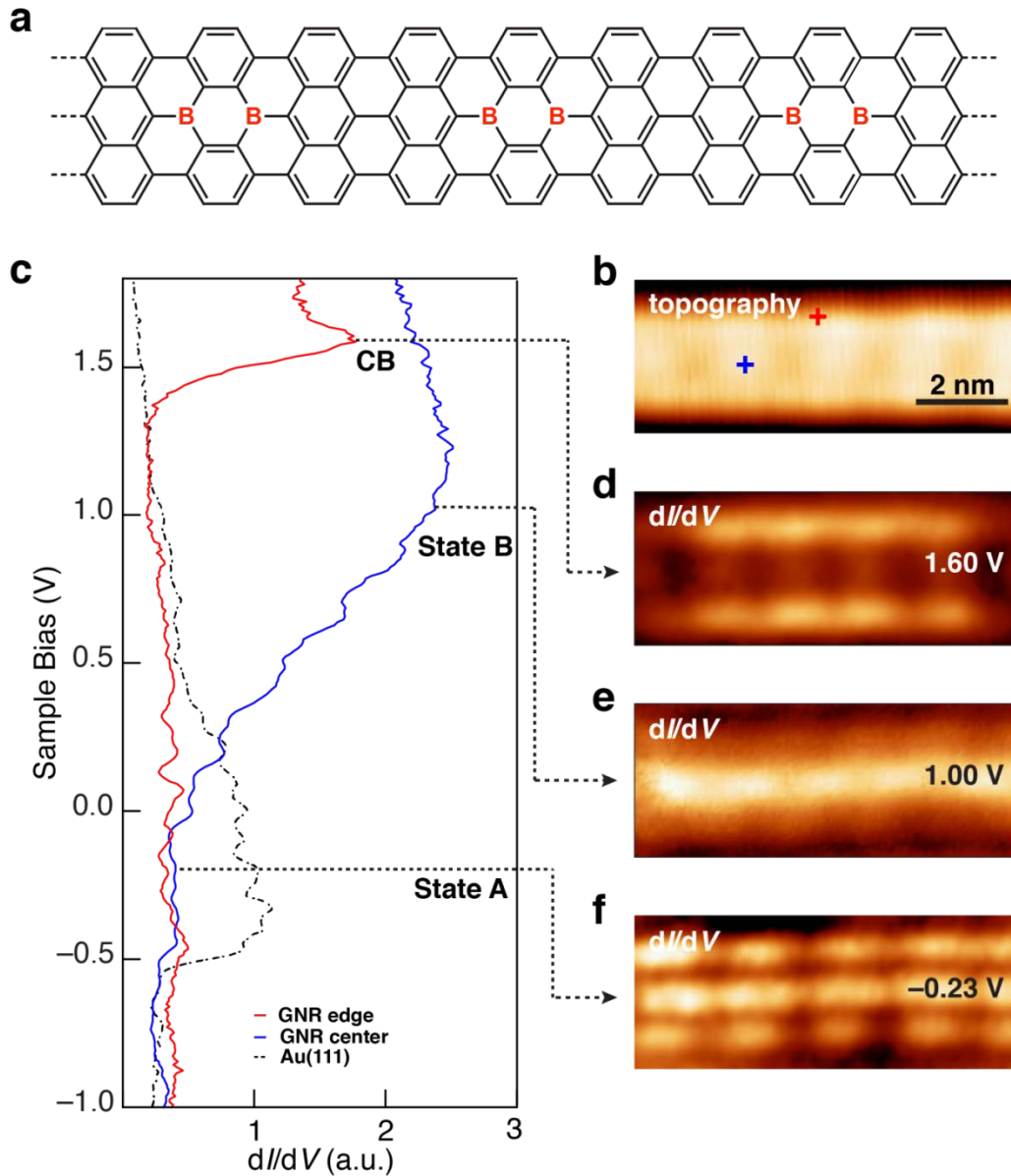


Figure 3.8: Electronic structure of densely boron-doped N=7 AGNR on Au(111). (a) Wireframe sketch of a densely-doped GNR. (b) STM topograph parameters: $V_s = 1.60$ V, $I_t = 20$ pA. (c) STM dI/dV spectroscopy measured at the edge and center of a densely-doped GNR as shown in (b). (d) dI/dV map taken at $V_s = 1.60$ V visualizes state at the CB edge. (e) dI/dV map taken at $V_s = 1.00$ V visualizes unoccupied dopant-induced state (State B). (f) dI/dV map taken at $V_s = -0.23$ V visualizes occupied dopant-induced state (State A). $T = 4.5$ K for all measurements. (d-f) have the same scale as (b).

3.2.3 Symmetry-Dependent Hybridization between the Dopant States and

Au(111) Substrate

Our experimental results for dilute and densely-doped AGNRs exhibit some qualitative agreement with DFT calculations for freestanding boron-doped AGNRs, but there are significant discrepancies. For example, in the dilute-doping limit our experiments faithfully reproduce the two expected defect states in the gap with one exhibiting s-like symmetry (State 2, which has no node) and the other exhibiting p-like symmetry (State 1, which has a node). However, our experimental measurements show a significant splitting between the two states (~ 1 eV) whereas the theoretical defect states are essentially degenerate. Furthermore, it is not clear why the experimental peak seen for State 1 is so much narrower than the broad, sloping spectroscopic feature that defines State 2.

In the densely-doped regime the experimental peak observed at $V_s = 1.60$ eV (Figure 3.8(c), red curve) is consistent with the theoretically predicted CB (Figure 3.6(f)). The new spectroscopic peak at $V_s \approx 1.0$ V (Figure 3.8(c), blue curve) also roughly corresponds to spectroscopic features expected to arise from a new dopant-induced band [125] (e.g., the upper dopant band in Figure 3.6(f)). However, there are major discrepancies between experiment and theory here as well. Most significant is the energy alignment of the observed spectroscopic features. The energy difference between the two experimental spectroscopic peaks shown in Figure 3.8(c) is only ~ 0.5 eV whereas the theoretically predicted energy difference between the CB and the upper dopant band in Figure 3.6(f) is ~ 1.5 eV. Moreover, the anomalously broad spectroscopic peak at $V_s = 1.0$ V is inconsistent with the simulation since the upper dopant bandwidth is predicted to be quite narrow (Figure 3.6(f)).

We conclude that these aforementioned discrepancies are most likely results of ignoring the Au(111) substrate in freestanding GNR calculations. Therefore, in order to better understand our experimental results, we performed additional calculations that fully take into account coupling from the underlying Au(111) substrate. The electronic structures of both dilute-doped and densely-doped GNRs on Au(111) were calculated via DFT using the supercells shown in Figure 3.9(d) and 3.10(d), respectively. Similar to our experimental data, the boron atoms in a fully relaxed simulated GNR sit closer to the Au(111) surface than the carbon atoms in undoped segments of the ribbon. This reduction of the boron-gold distance indicates significant interaction between the boron dopants and the gold substrate atoms.

In order to simulate the dilute-doped dI/dV spectroscopy of Figure 3.7(c), we calculated the energy-resolved LDOS (including gold substrate effects) averaged over a $7.5 \text{ \AA} \times 7.5 \text{ \AA}$ area 4 \AA above the boron-doped segment following the topography of the GNR. The results are plotted in Figure 3.9(a). Substantial features are seen to appear in previously gapped regions due to hybridization between the GNR and the underlying Au(111) substrate (the CB (1.6 eV) and VB

(-0.9 eV) edges are obtained from the undoped segment). In particular, two features are observed that arise from the boron defect, a broad resonance in the unoccupied states and a narrower resonance in the occupied states. The occupied resonance appears in the range -0.4 eV $< E <$ -0.1 eV and exhibits the LDOS pattern shown in Figure 3.9(c) (obtained at $E = -0.21$ eV).

This LDOS map has bright features at the outer edges and two interior peaks of high intensity located on the C-B bonds that lie along the GNR axis. As seen in Figure 3.9(f), the wavefunction at this energy has odd parity (p -like) under mirror symmetry.

The unoccupied LDOS is quite different from what is seen in the occupied states. Here a much broader feature arises over the range 0.3 eV $< E <$ 0.9 eV (a slight dip can be seen at $E \sim 0.5$ eV). Figure 3.9(b) shows a representative LDOS map of this defect state (obtained at $E = 0.38$ eV). As seen in Figure 3.9(e), this dopant state has a more delocalized wavefunction than the occupied state feature and exhibits approximate even parity (s -like).

The simulated behavior of the dilute-doped GNR on Au(111) supports our hypothesis that differences observed between the experiment and the “freestanding” theory arise from the interaction between boron-doped GNRs and the gold substrate. The reasonably good agreement between theory and experiment for the defect state energies and broadening allows us to identify the occupied and unoccupied features in the theoretical LDOS of Figure 3.9(a) with experimentally observed State 1 and State 2 of Figure 3.7(c). Further evidence for this assignment is found in the striking resemblance of the theoretical occupied state LDOS pattern (Figure 3.9(c)) to State 1 (Figure 3.7(f)), as well as the resemblance of the theoretical unoccupied LDOS pattern (Figure 3.9(b)) to State 2 (Figure 3.7(e)). The energy splitting between the central energy of the two simulated defect state peaks (~ 1 V) is also similar to what is observed experimentally, indicating that the boron-induced defect states (which are nearly degenerate for a freestanding GNR) are strongly split by interaction with the Au(111) substrate. This interaction also explains the different broadening of the two defect states, which arises due to the different symmetries of the dopant states. Because State 1 has p -like character it hybridizes more weakly with the s -like surface states of gold (leading to a narrower peak), whereas State 2 has s -like character and so hybridizes more strongly with gold (leading to a broader peak). The s - and p -like symmetry of the boron defect states is thus a primary factor in determining the dopant electronic structure for the strongly hybridized boron-doped GNR/Au(111) complex.

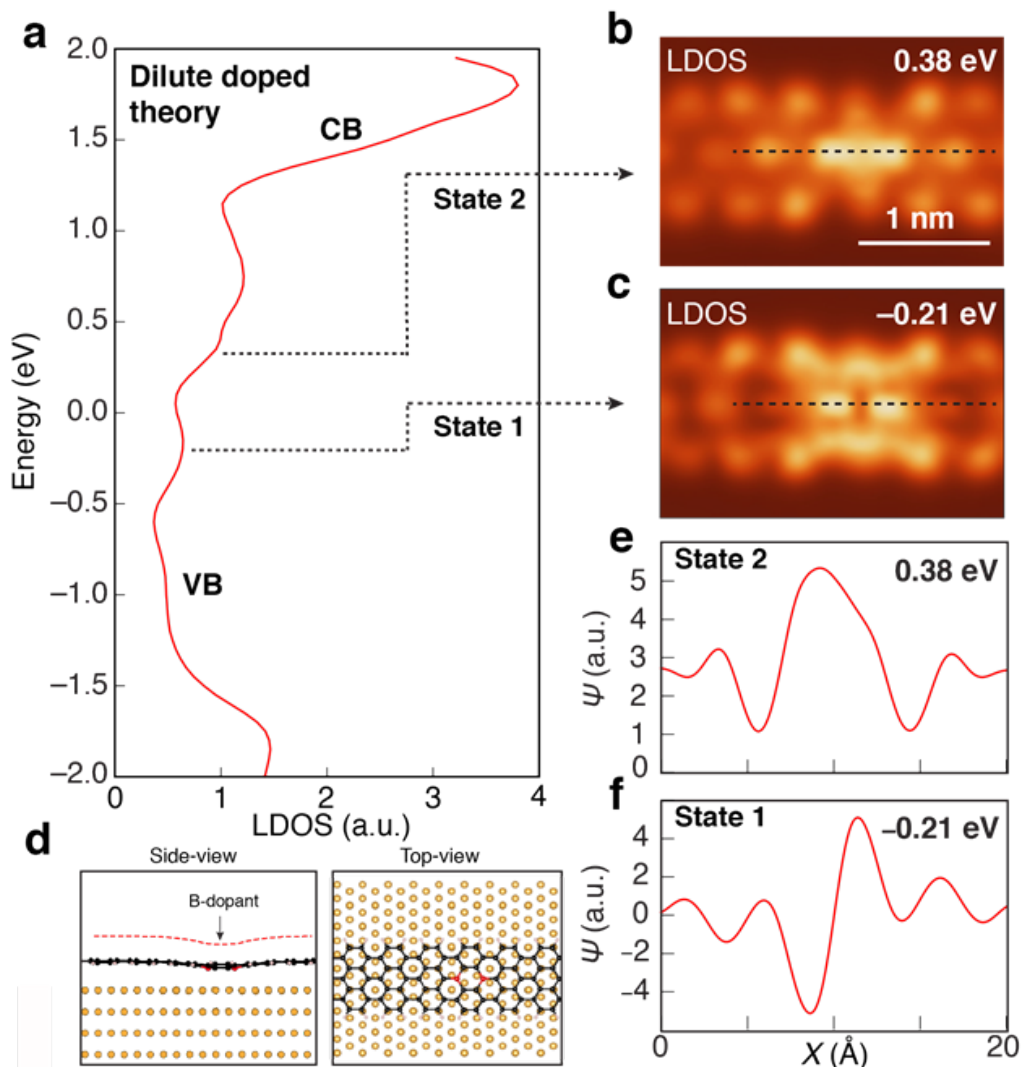


Figure 3.9 DFT-LDA calculation of dilute-doped N=7 GNR on Au(111) substrate. (a) Calculated LDOS 4 \AA above the boron-doped segment shows dopant States 1 and 2 (theoretical LDOS is broadened by a Gaussian function with standard deviation $\sigma = 125$ meV). Calculated LDOS map is shown for (b) $E = 0.38$ eV (integrated over a 0.05 eV energy window) and (c) $E = -0.21$ eV (integrated over a 0.05 eV energy window). (d) Side-view and top-view of the supercell and the relaxed structure used to calculate the dilute-doped GNR. The supercell includes 4 layers of Au atoms. Red dashed line shows the surface upon which the LDOS maps are calculated. (e) Calculated wave function along dashed line in (b) for $E = 0.38$ eV. (f) Calculated wave function along dashed line in (c) for $E = -0.21$ eV. (b) and (c) have the same scale.

Motivated by the agreement between experiment and theory for the dilute-doped GNRs in the presence of Au(111), we examined the electronic structure of densely-doped GNRs supported by Au(111). The energy-resolved LDOS 4\AA above the boron-doped segment was calculated using the same method as in the dilute case and is shown in Figure 3.10(a). The energy-dependent LDOS of Figure 3.10(a) is very similar to what is seen in the dilute-doped case (Figure 3.9(a)). For example, a broad unoccupied resonance and a narrower occupied resonance arise due to substrate interactions, and the resonances have almost identical energy and width as the State 1 and 2 features of the dilute regime. A representative LDOS map of the theoretical unoccupied states obtained at $E = 0.35\text{ eV}$ (Figure 3.10(c)) is dominated by nearly uniform bright intensity along the longitudinal axis of the densely-doped GNR (i.e., bright intensity occurs at the boron dimer sites as well as at the carbon dimer sites between them). This theoretical LDOS map is qualitatively very similar to the experimental unoccupied state dI/dV map of Figure 3.8(e), and so we identify the broad, unoccupied state feature of Figure 3.10(a) as State B. A representative map of the theoretical occupied states obtained at $E = -0.22\text{ eV}$ (Figure 3.10(d)) shows a shifting of LDOS intensity to the GNR edges and a new lateral periodicity whose wavelength matches the distance between boron dimers (due to reduction in LDOS at the carbon dimer sites between boron dimers). This theoretical LDOS map is qualitatively similar to the experimental occupied state dI/dV map of Figure 3.8(f), and so we identify the narrow, occupied state feature of Figure 3.10(a) as State A.

Our simulations allow us to confirm that the underlying physics determining the behavior of densely-doped GNRs is similar to the symmetry-dependent mechanism at work in the dilute-doped regime, despite the significant difference in dopant concentrations. This can be seen by examining the wave functions of occupied and empty states for densely-doped GNRs. The wave function for State B is seen to be symmetric around a line bisecting a boron dimer (not shown here), and thus exhibits s -like symmetry similar to State 2 of the dilute regime (Figure 3.9(e)). This explains why the densely-doped GNR couples so strongly to the s -like conduction band of Au(111) at this energy, thus leading to the broad, unoccupied resonance observed both theoretically (Figure 3.10(a)) and experimentally (Figure 3.8(c)) which looks so similar to State 2 of the dilute regime. The wave function for State A, on the other hand, has p -like symmetry around the boron dimer which explains why it couples less strongly to the gold conduction band and exhibits a narrower resonance, similar to State 1 of the dilute regime. Due to the dominant effects of substrate hybridization, States A and B of the dense regime can be heuristically thought of as simple 1D arrays of States 1 and 2 of the dilute regime, respectively.

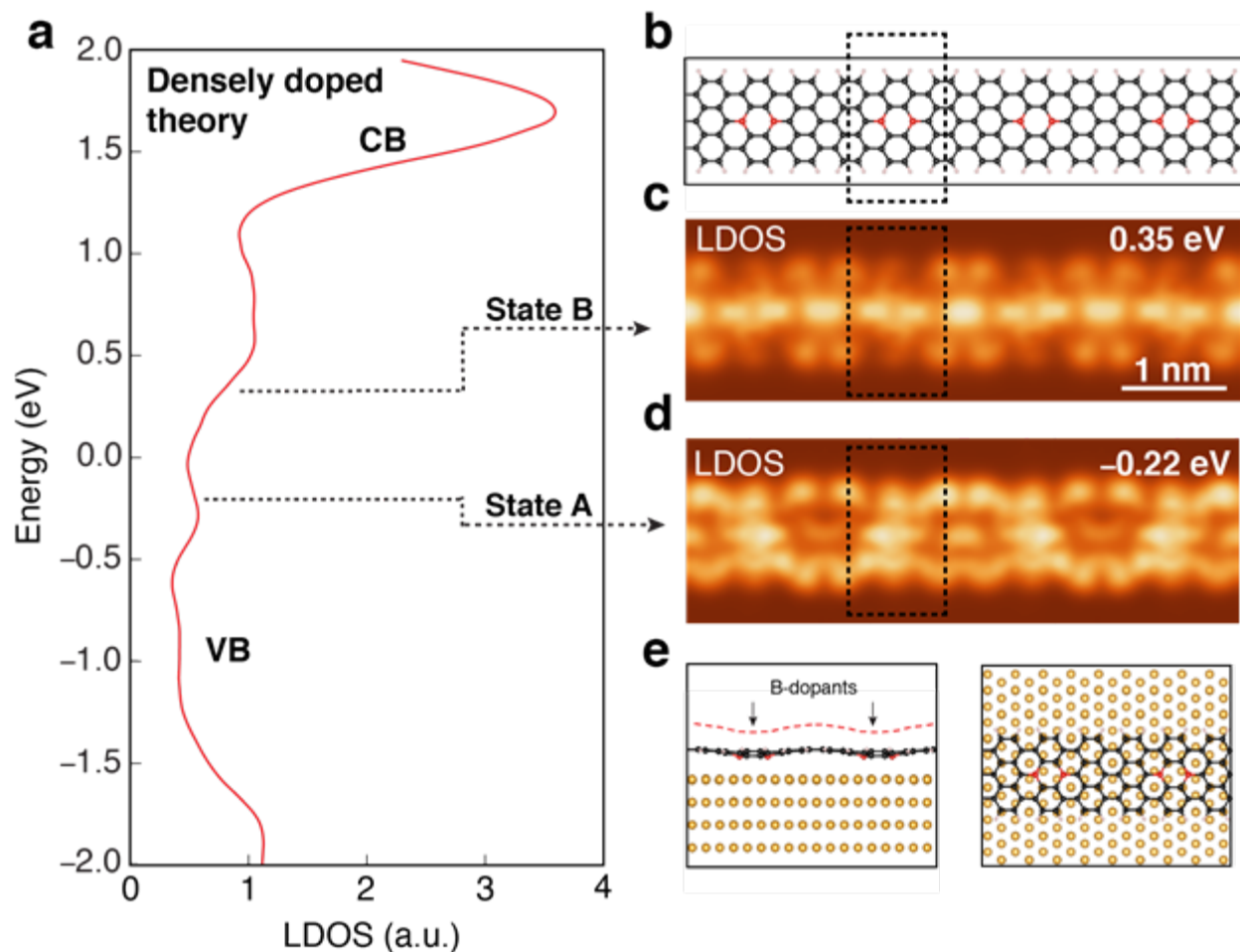


Figure 3.10 DFT-LDA calculation of densely-doped $N=7$ GNR on Au(111) substrate. (a) Calculated LDOS 4 \AA above boron-doped segment shows dopant States A and B (theoretical LDOS is broadened by a Gaussian function with standard deviation $\sigma = 125 \text{ meV}$). (b) Wireframe sketch shows location of boron atoms. Calculated LDOS maps (each including four boron dimers) are shown for (c) $E = 0.35 \text{ eV}$ (integrated over a 0.05 eV energy window) and (d) $E = -0.22 \text{ eV}$ (integrated over a 0.05 eV energy window). (e) Side view and top view of the supercell and the relaxed structure (includes 4 layers of Au atoms) used to calculate the relaxed densely-doped GNR. Red dashed line shows the surface upon which the LDOS maps are calculated. (c) and (d) have the same scale.

3.2.4 Summary

Our experimental and theoretical studies show that introduction of boron dopants into

AGNRs induces the formation of two new in-gap dopant states that have different symmetries. These dopant-induced states continuously evolve as the boron dopant concentration increases. Moreover, we see that hybridization between dopant atoms and the underlying Au(111) substrate has an unusually strong impact on the electronic structure of boron-doped GNRs, much greater than for other doped GNR systems studied to date [112, 114, 116]. Both the dilute and densely-doped electronic behavior depends strongly on the impurity state symmetry, with *s*-like (*p*-like) states hybridizing more strongly (weakly) with the gold substrate, thus leading to strong, symmetry-dependent energy splitting. This strong substrate coupling masks the effects of impurity-impurity interactions that are predicted for freestanding boron-doped GNRs. We thus expect very different electronic behavior for boron-doped GNRs placed on substrates that interact less strongly with boron impurity atoms than gold.

3.3 N=11 AGNR

According to DFT calculations, AGNRs can be grouped into three categories based on the number of carbon dimer rows across the width (or the number N). The three categories are $N = 3p$, $N = 3p + 1$, and $N = 3p + 2$ where p is an integer. Within each of the three categories, the band gap of AGNRs decreases as the width of the GNR increases due to quantum confinement effect, however, the band gap does not decrease monotonically as N increases [6]. In general, AGNRs in the $N = 3p + 2$ group have the smallest band gaps, and AGNRs in the $N = 3p + 1$ group have the biggest band gaps (see Figure 2(b) of ref [6]). That is to say, N=11 AGNR should have a smaller band gap than that of N=13 AGNR, although N=11 AGNR is narrower than N=13 AGNR.

Our goal for this project was to synthesize N=11 AGNRs and to test these theoretical predictions. Success here would allow our electrical engineering collaborators to make N=11 AGNRs into devices with potentially smaller Schottky barriers and better resulting device performance. After spending more than a year on this project, however, we were not able to publish any results due to the defective nature of the ribbons grown.

3.3.1 On-Surface Synthesis of N=11 AGNRs via *sp*³-to-*sp*² conversion

At the time we were working on this project, there were quite a few publications regarding AGNRs with different widths. There were reports of N=7 [15], N=13 [111], N=15 [126], and N=5 [127, 128] AGNRs, and a closer examination of all the molecular precursors involved in the bottom-up synthesis of these AGNRs reveals that all carbon atoms in each of the precursors have *sp*² hybridization. In other words, the coupling reactions leading to the AGNRs (polymerization and cyclodehydrogenation) did not change the hybridization of the carbon atoms.

In contrast, the molecular precursor we used to fabricate N=11 AGNRs (designed and

synthesized by Wade Perkins in Fischer's group) have four methyl groups with sp^3 carbon atoms (see Figure 3.11). And in order to get to totally flat and aromatic AGNRs, there has to be a conversion from sp^3 carbon to sp^2 carbon. More specifically, such a design of the precursor molecule means that the cyclodehydrogenation reaction after the polymerization needs to happen not only between carbon atoms of adjacent phenyl rings (which is the case for almost all previous AGNR synthesis), but also between adjacent methyl groups as well as carbon atoms of nearby methyl and phenyl (see Figure 3.11).

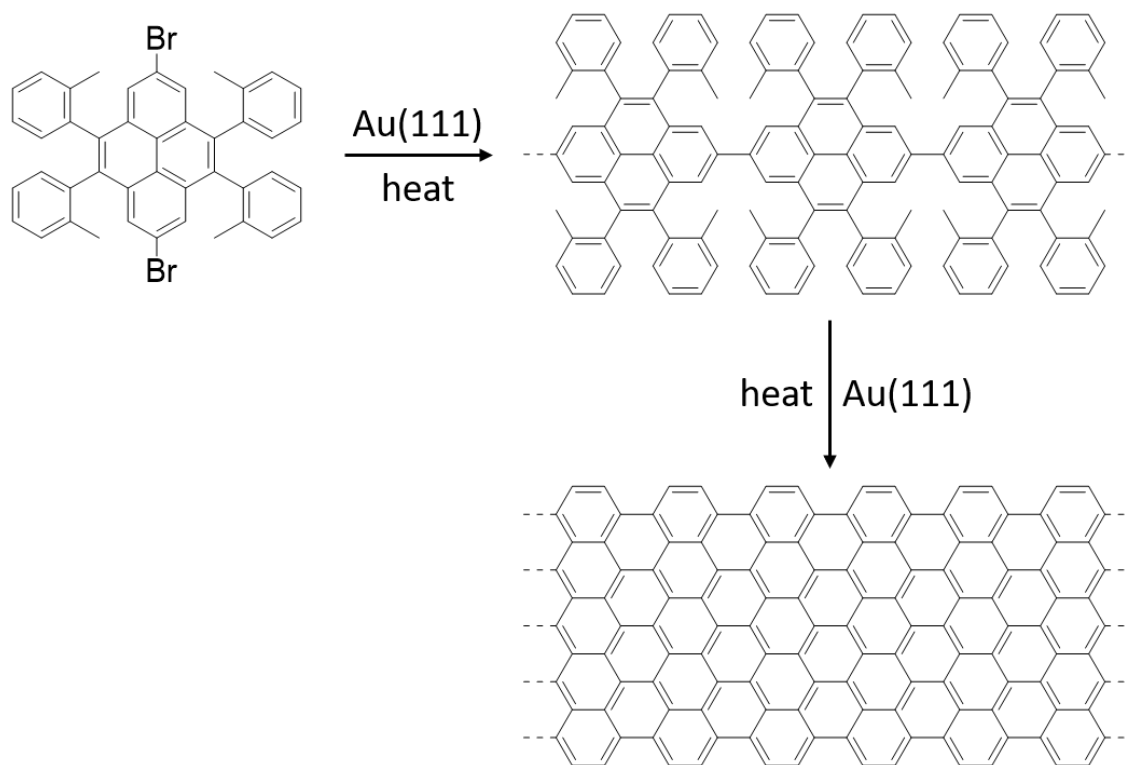


Figure 3.11 Proposed Synthetic Route of $N=11$ AGNRs.

After deposition of the precursor molecules onto a Au(111) surface, the sample was annealed to a sequence of increasing temperatures and cooled down to $T = 7$ K after each annealing for STM measurements. Figure 3.12 shows the representative STM images and chemical structures after each annealing stage. Annealing to 200 °C results in the formation of the polymer after dehalogenation, as bright protrusions can be seen along either side of the polymer chain. Such protrusions are usually associated with the non-planarity of the polymer, in this case induced by the phenyl rings and methyl groups pointing out of plane on either side of the polymer backbone. We therefore conclude that almost no cyclization reaction has happened at this annealing stage. Further annealing the sample to 250 °C leads to parts of the polymer becoming planar with

some bright protrusions remaining, and annealing to 300 °C reduces the number of bright protrusions even more. After annealing to 350 °C, there are almost no bright protrusions and fully cyclized N=11 AGNRs are formed. The gradual reduction of the bright protrusions with increasing temperature indicates the complete cyclization of the polymer doesn't happen at one fixed temperature; instead it happens gradually over a range of temperatures. This can be explained by the difference in cyclization barriers between the sp² carbons of the phenyl rings and the sp³ carbon of the methyl groups. These STM images capture the conversion from sp³ carbon to sp² carbon, a strategy that had not been used in the previous synthesized AGNRs. (Although later the synthesis of zigzag GNRs did use a molecular precursor with methyl groups and sp³ carbon [113].)

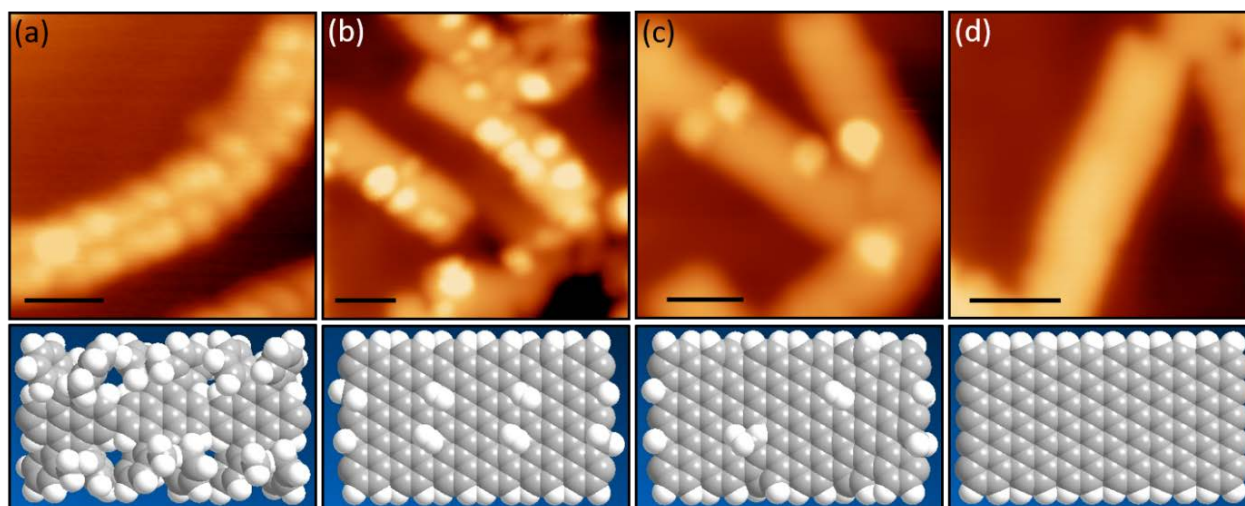


Figure 3.12 Representative STM images and chemical structures after each annealing stage during growth of N=11 AGNRs. (a) Sample annealed to 200 °C. ($I_t = 5$ pA, $V_s = 1.2$ V) (b) Sample annealed to 250 °C. ($I_t = 25$ pA, $V_s = 0.05$ V) (c) Sample annealed to 300 °C. ($I_t = 55$ pA, $V_s = 0.10$ V) (d) Sample annealed to 350 °C. ($I_t = 55$ pA, $V_s = -0.10$ V) All scale bars are 2 nm.

3.3.2 Quality of N=11 AGNRs Characterized by STM and nc-AFM

Figure 3.13 shows STM and nc-AFM characterizations of the sample after the final annealing stage. Although a large scale image (Figure 3.13(a)) seemingly indicates the successful synthesis of N=11 AGNRs, the ribbon-like features are unusually curvy, unlike the straight and rigid edges reported in previous studies of different AGNRs [15, 111]. A closer examination of Figure 3.13(a) reveals that the edges are not only curvy, but also defective. Occasionally there is a straight segment of uniform width as seen in Figure 3.13(b), however, there is seldom an entire ribbon that is as straight and uniform. In order to have a better understanding of these ribbon-like

structures, we decided to perform nc-AFM measurements. Figure 3.13(c) shows the STM image of a particular curly nanoribbon and the corresponding nc-AFM image is shown in Figure 3.13(d). Obviously the nanoribbon under imaging here is very defective with a lot of missing atoms and almost no straight edges. On the other hand, the dI/dV point spectra taken on different positions of the ribbon show features at different energy, and no state that is dispersive throughout the length of the ribbon can be seen. It was with great disappointment that we had to conclude that the nanoribbons we grew did not have good enough quality to warrant any intrinsic electronic property measurements.

Defective AGNRs indicate that the actual reactions happening on the Au(111) surface are not the same as shown in Figure 3.11. One hypothesis is based on the fact that the carbon atoms of the methyl groups are actually benzylic carbons, and they are relatively reactive. If the energy barrier of dehydrogenation on the benzylic carbons is similar to that of dehalogenation on the aryl carbons at the center of the GNR backbone, then a coexistence of benzyl radicals and aryl radicals is likely to happen on the surface at certain annealing temperature, and a decrease in the selectivity of preferred aryl to aryl coupling is expected. Moreover, the possibility of radical rearrangements within a conjugated- π network increases the number of potential radical configurations and therefore results in more undesired side products.

About one year after we got these results, a breakthrough in the field of bottom-up GNRs — synthesis of zigzag GNRs from molecular precursors — was achieved [113]. The precursor used in that synthesis contains a dimethyl phenyl segment, with two benzylic carbons. Comparing the synthesis of $N=11$ AGNRs and the ZGNRs, both precursors have benzyl carbon atoms (or methyl phenyl groups), and an sp^3 -to- sp^2 conversion is essential to form the fully cyclized GNRs; however, the ZGNRs are higher in quality compared to our $N=11$ AGNRs [113]. Due to STM's lack of temporal resolution at the time scale of chemical reactions, it is difficult to fully understand the origin of the difference in GNRs quality, although such difference may be related to a major difference in the reaction pathway between the two syntheses, that is, the formation of $N=11$ AGNRs requires cyclodehydrogenation not only between benzylic carbons (sp^3) and aryl carbons (sp^2), but also between benzylic carbons (sp^3) and benzylic carbons (sp^3) (see Figure 3.11), whereas the formation of the ZGNRs only requires cyclodehydrogenation between benzylic carbons (sp^3) and aryl carbons (sp^2).

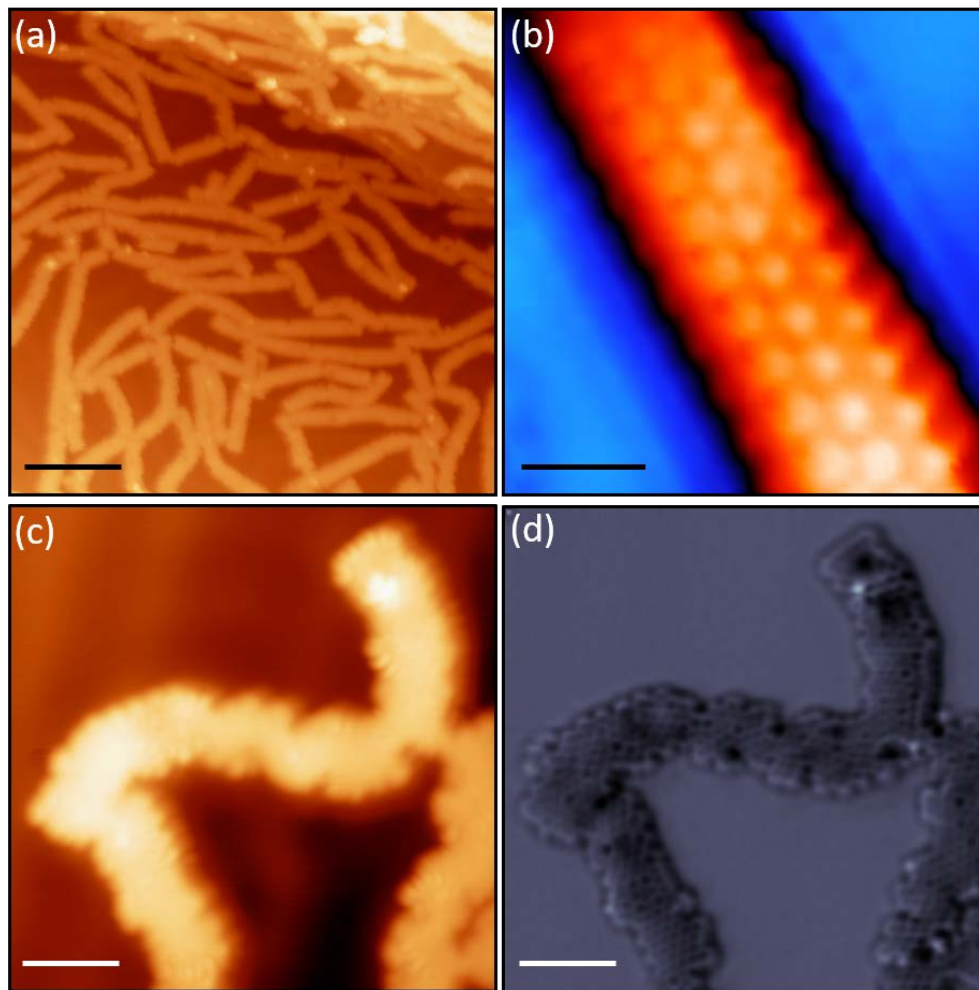


Figure 3.13 STM and AFM images of N=11 AGNRs. (a) Large scale STM image shows ribbon-like structures with highly defective edges. ($I_t = 10$ pA, $V_s = 0.80$ V) (b) Zoomed-in STM image shows a straight GNR segment with uniform width. ($I_t = 105$ pA, $V_s = 0.10$ V) (c) STM image of a particularly curvy and defective GNR. (d) Corresponding nc-AFM image of the same area as in (c). Scale bars: (a) 10 nm, (b) 1 nm, (c) and (d) 2 nm.

3.3.3 Summary

Our experiments show that the conversion from sp³ carbon to sp² carbon does occur during the on-surface synthesis of N=11 AGNRs. Although our proposed reaction pathway worked to some extent and gave one-dimensional ribbon-like structures, the resulting GNRs did not have high enough quality for the study of their intrinsic local electronic structure. At the time this is written, there is still no report of on-surface bottom-up synthesis of N=11 AGNRs, and our approach may very well be the closest to success. Certain modifications to the synthetic

procedure, such as change of the substrate, a slower increase of the annealing temperature, or a slight revision of the molecular precursor might lead to the synthesis of N=11 AGNRs with atomically precise edges and allow exploration of their intrinsic electronic properties.

3.4 Conclusion and Outlook

We have shown that on-surface synthesis from molecular precursors is an effective tool to obtain atomically precise graphene nanoribbons, including GNR heterojunctions with varying width and hetero-atom doped GNRs. The successful realization of the GNR species is confirmed by low temperature STM topographic imaging, which provides atomic resolution of the GNR structures. The local electronic structure of different GNR species is measured by means of STS and dI/dV mapping, and compared with results from DFT calculations. These studies help us understand how various aspects of a GNR system — such as width modulation, dopant atom concentration, and substrate hybridization — determines the electronic properties of the GNR.

One of the key aspects of GNR research that has not been discussed here is the integration of GNRs into electronic devices. Towards that end, our electrical engineering collaborators have made great strides, from the first realization of bottom-up graphene nanoribbon (N=7 AGNRs) field effect transistors [129] to short-channel field effect transistors with improved performance (N=9 and N=13 AGNRs) [130]. However, a few major obstacles still have to be overcome before high performance GNR FET devices can be realized. One barrier is due to the mismatch between the growth substrate for GNRs (which usually needs to be a metal in order to catalyze the reaction) and the substrate for a device (which has to be an insulator and cannot be a metal), and transfer of the as-grown GNRs from a metallic surface onto an insulating substrate has proven to be difficult. In order to overcome this barrier, both wet-transfer and dry-transfer strategies have been explored, but both methods have pros and cons. Therefore, finding the suitable chemistry which enables the synthesis of GNRs on an insulating substrate will be a major technological advance for the research of GNRs. Another barrier is literally called a “Schottky barrier”, which is the potential energy barrier for electrons formed at a metal–semiconductor junction. A high Schottky barrier between the semiconducting GNR and the metal contact limit the performance of the FET device. Potential improvement can be achieved by synthesizing new types of GNRs with smaller bandgaps and finding a better contact material or geometry. Devices that have different operation principles than the traditional FET have also been proposed, such as a tunnel field effect transistor [131].

From a scientific rather than technological point of view, there are also some very interesting questions that have not yet been answered. For example, can one synthesize a GNR that is metallic? What about GNR superconductors? Can ZGNRs be used as spintronic components due to spin polarizations on opposite zigzag edges? Answers to these questions will surely expand the scope of this vibrant research field.

Chapter 4

Two-Dimensional Covalent Organic Frameworks

This chapter discusses my work on 2D covalent organic frameworks, which are extended crystalline organic structures made of light elements. The researchers who contributed to these studies are Chen Chen, Trinity Joshi, Zahra Pedramrazi, Dr. Gaoqiang Wang, Dr. Huifang Li, Anton D. Chavez, Austin Evans, Dr. Michio Matsumoto, Dr. Christian Diercks, Daniel J Rizzo, Dr. Christopher Bronner, Nick Lau, Bobby Ge, Lingjie Zhou, Eric Yu, Ankit Kumar, Dr. Omar M. Yaghi, Dr. William R. Dichtel, Dr. Hong Li, Dr. Jean-Luc Bredas, and Dr. Michael F. Crommie.

Our study on 2D COFs has a major focus on understanding their local electronic structure. One central question that we want to answer is how covalent bonding causes the electronic structure of molecules to evolve as they bond into extended networks. On the other hand, we also want to explore the possibility of tuning the electronic structure of 2D COF by rational design of molecular precursors. The following sections will give examples on how we achieved these goals.

4.1 Symmetrical Bonding Scheme: COF366-OMe

After I had switched my research direction and started to study 2D COFs, I tried to grow a few different COF systems without success. This changed after I noticed the porphyrin-containing square-lattice COF of reference [67]. That paper reported the solution synthesis of single layer COF on HOPG as well as imaging with ambient STM; however, no spectroscopic results were reported. We decided to grow this same COF inside our UHV chamber and study its electronic structure with our low-temperature STM. This worked quite well.

The work described here was originally published in “ACS Nano” [68].

4.1.1 Electronic Structure of the Core Precursor Molecule TAPP

As mentioned earlier, a central question regarding COFs is how covalent bonding causes the

electronic structure of molecules to evolve as they bond into extended networks. Characterization of electronic structure of the precursor molecules thus becomes an integral part of our experiments. We first performed STM/STS electronic characterization of an isolated precursor molecule (5,10,15,20-tetrakis (4-aminophenyl) porphyrin, or TAPP, chemical structure shown in Figure 4.1(b)) on Au(111) (Figure 4.1). The STM topographic image of Figure 4.1(a) shows that TAPP exhibits a four-lobe structure with a slight dip in the middle, corresponding to the core of the porphyrin. Energy-dependent LDOS obtained by dI/dV spectroscopy at the center of a TAPP molecule exhibits two peaks that are assigned to the TAPP HOMO (-0.44 ± 0.06 V) and LUMO ($+1.42 \pm 0.05$ V), corresponding to a 1.85 eV transport gap (Figure 4.1(b)) (dI/dV traces obtained on different parts of the TAPP molecule exhibit different amplitudes for these peaks, but the peak energies do not vary).

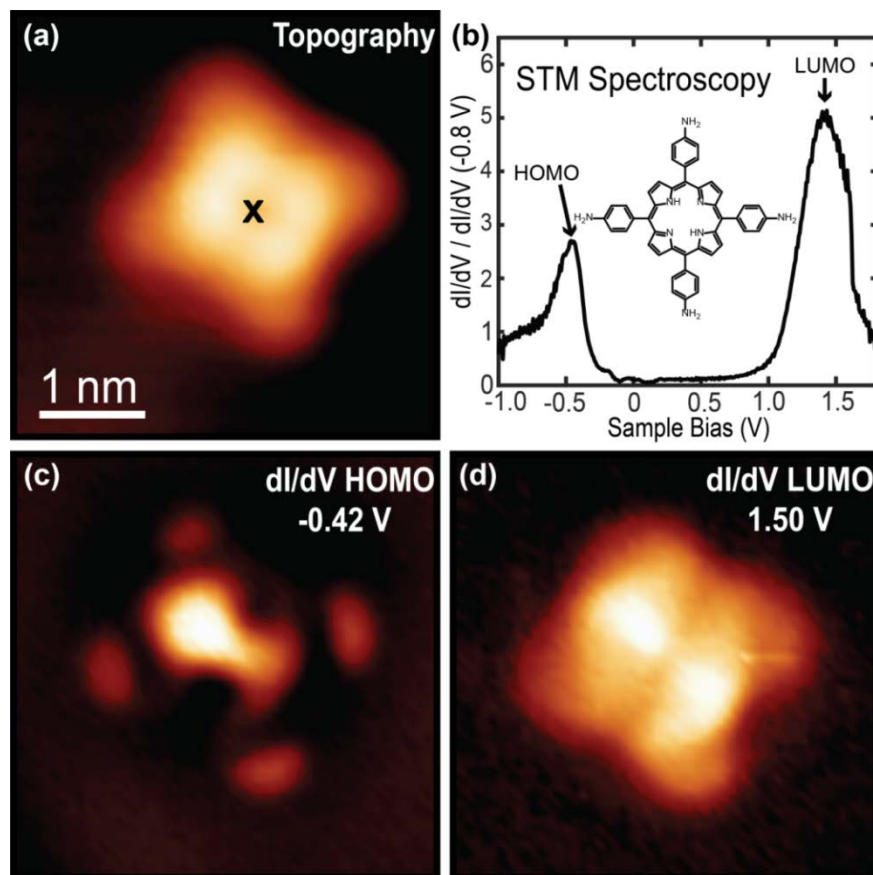


Figure 4.1 Single TAPP molecule electronic structure. (a) STM topographic image of a single TAPP molecule on a Au(111) surface (sample bias $V_s = 2.0$ V, tunneling current $I_t = 10$ pA). (The “X” represents the location where the dI/dV curve shown in (b) was obtained.) (b) dI/dV point spectra measured on top of a single TAPP molecule shows HOMO and LUMO states (open

feedback parameters: $V_s = 1.0$ V, $I_t = 60$ pA; modulation voltage $V_{rms} = 10$ mV). Inset shows chemical structure of a TAPP molecule. dI/dV maps of the TAPP HOMO and LUMO states are shown for bias voltages (c) -0.42 V and (d) 1.50 V (open feedback parameters: $V_s = 1.0$ V, $I_t = 60$ pA; modulation voltage $V_{rms} = 10$ mV).

dI/dV mapping was performed at the HOMO and LUMO peak energies to examine the wavefunction spatial distribution for isolated TAPP molecules (Figure 4.1(c), (d)). As seen in Figure 4.1(c), the HOMO state is nearly two-fold symmetric and exhibits an asymmetrical "dumbbell" structure in the interior. The LUMO state is more diffuse and has LDOS intensity in regions where the HOMO state is dark (Figure 4.1(d)). Similar frontier orbital LDOS patterns have been reported previously for related porphyrin molecule adsorbates on Au(111) [132].

4.1.2 Synthesis of COF366-OMe on Au(111) from Precursor Molecules

The Schiff-base condensation reaction between TAPP core molecules and 2,5-dimethoxybenzene-1,4-dicarboxaldehyde linker molecules (DMA, chemical structure shown in Figure 4.2(a)) results in a 2D COF with a square lattice. As shown in Figure 4.2(a), DMA molecules were first deposited onto a Au(111) surface with a coverage of 0.9 monolayer, resulting in close-packed islands with an inter-molecular spacing of 0.8 nm. TAPP molecules were then deposited onto this surface, resulting in an intermixed adlayer (DMA + TAPP) as shown in Figure 4.2(b). The TAPP/DMA intermixed adlayer was then annealed at 150° C for 1 hour in UHV to induce COF formation. The resultant COF covers the Au(111) surface in square-lattice patches (Figure 4.2(c)) with a unit cell size of 2.5 ± 0.1 nm, in good agreement with the expected porphyrin core-to-core distance (2.57 nm) for the COF structure shown in Figure 4.2(d). The observed structure is also in agreement with room temperature ambient STM images of this COF obtained previously from samples grown on graphite via solution-phase processing [67]. The zoomed-in STM image shown in Figure 4.3(a) shows additional detail that confirms the formation of the COF, which we refer to as COF366-OMe following the naming convention used in the report of its solvothermal synthesis [133]. The positions of each methoxy group can be inferred from the orientation of the oval-shaped linkages positioned between porphyrin centers in the zoomed-in image of Figure 4.3(a). We note that these methoxy groups are randomly distributed, i.e., there are no chiral domains within the COF.

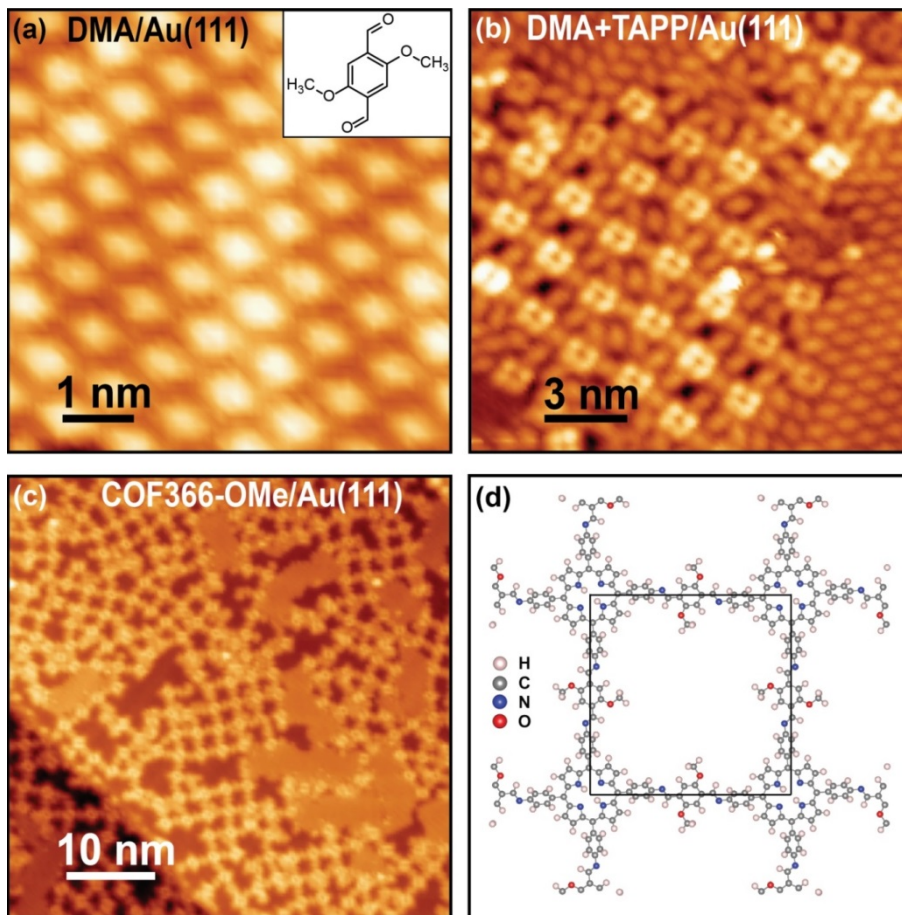


Figure 4.2 Synthesis of COF366-OMe on a Au(111) surface. (a) STM topographic image of DMA molecules deposited on Au(111) surface ($V_s = 0.8$ V, $I_t = 10$ pA). Inset shows the structure of a DMA molecule. (b) STM topographic image shows a mixture of TAPP and DMA molecules on Au(111) surface before reaction ($V_s = 1.0$ V, $I_t = 10$ pA). (c) Large-scale STM image of COF366-OMe on Au(111) after reaction of TAPP and DMA molecules ($V_s = 2.0$ V, $I_t = 10$ pA). (d) Model structure of COF366-OMe. The black square shows a unit cell.

4.1.3 Local Electronic Structure of COF366-OMe Measured by STM

The local electronic properties of COF366-OMe were characterized by performing STS point spectroscopy at different locations on the 2D COF (Figure 4.3(b)). The black curve shows a reference spectrum taken on a bare Au(111) region; the feature near -0.5 V corresponds to the well-known Shockley surface state of Au(111). When the TAPP core of the COF was probed (at the position of the blue X in Figure 4.3(a)), two prominent peaks are seen at -0.9 V and $+1.0$ V (blue curve). In contrast, the spectrum of the DMA linker shows only a small peak at $+1.0$ V (red curve), suggesting that this feature arises from delocalization of the state into the linker. We

assign the peak at -0.9 V as the COF366-OMe valence band maximum and the peak at $+1.0$ V as the conduction band minimum, thus leading to a band gap of 1.98 ± 0.04 eV for COF366-OMe (the uncertainty is the standard deviation of measurements obtained from 10 different cores, each connected to four nearest neighbors). Because the COF electronic structure is relatively localized, we refer to the COF valence band maximum as the highest occupied molecular orbital (HOMO) and the COF conduction band minimum as the lowest unoccupied molecular orbital (LUMO).

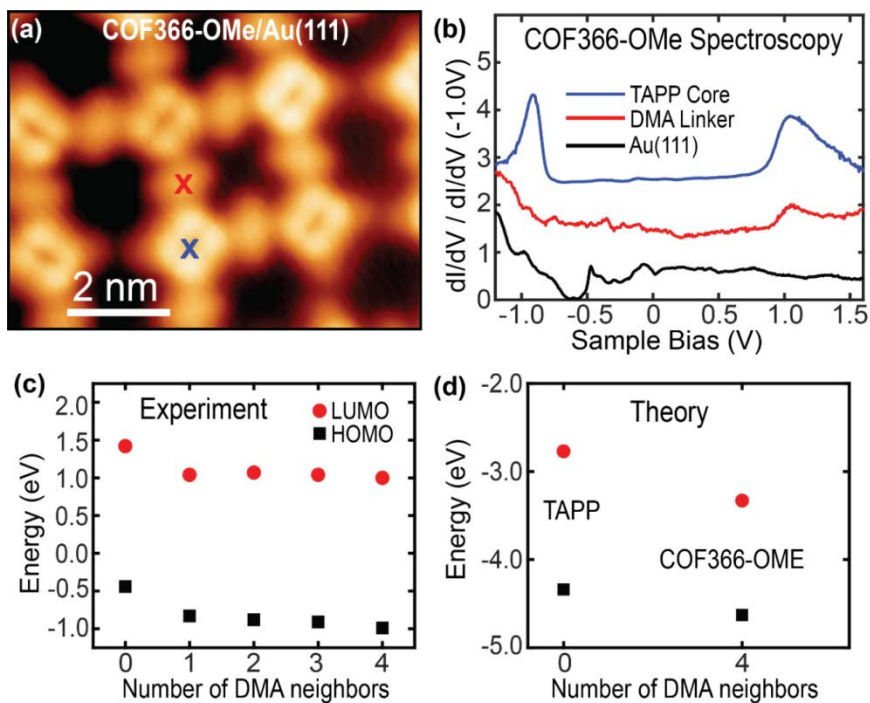


Figure 4.3 STS measurements of COF366-OMe on Au(111) surface. (a) Zoomed-in STM image of COF366-OMe ($V_s = 1.0$ V, $I_t = 10$ pA). Red and blue crosses indicate the positions at which dI/dV spectra were taken. (b) dI/dV spectra taken at location of DMA linker (red curve) and TAPP core (blue curve) shown in (a), as well as bare Au(111) surface for reference (black curve). Each curve is normalized by the value at $V_s = -1.0$ V, and the red (blue) curve is upshifted by 1 (2.5) a.u. for clarity (open feedback parameters: $V_s = 1.0$ V, $I_t = 40$ pA, 60 pA, 80 pA for the red, black and blue curve respectively; modulation voltage $V_{rms} = 10$ mV). (c) Effect of number of DMA neighbors on the HOMO and LUMO energies of a porphyrin core (0 DMA neighbors refers to an isolated TAPP molecule). Each data point consists of at least eight different measurements, and the error bars are smaller than the size of the dots. (d) DFT calculations of the electronic structure of freestanding, isolated TAPP molecule and COF366-OMe, indicating a downshift in HOMO and LUMO energies upon COF formation (zero energy is the vacuum level).

A closer inspection of the extended structure in Figure 4.3(a) reveals that some of the linkers are missing, resulting in TAPP cores that are covalently bonded to only two or three DMA linkers instead of the four found in the ideal COF structure. To understand the effect of this type of defect, we took dI/dV point spectra on TAPP cores connected to different numbers of DMA linkers. The average HOMO and LUMO energies for TAPP cores connected to different numbers of linkers are plotted in Figure 4.3(c). The HOMO-LUMO gap measured at the site of a TAPP core does not change significantly with the number of linkers bonded to it. However, a large energy downshift in the HOMO/LUMO states (0.4 eV) is seen as soon as even a single DMA linker is bound. Subsequent bound linkers do not significantly change the energy shift, although a slight downward trend in the HOMO energies is seen. Spectroscopic surveys performed in different COF regions and on different parts of the porphyrin cores yield no significant deviations from these findings.

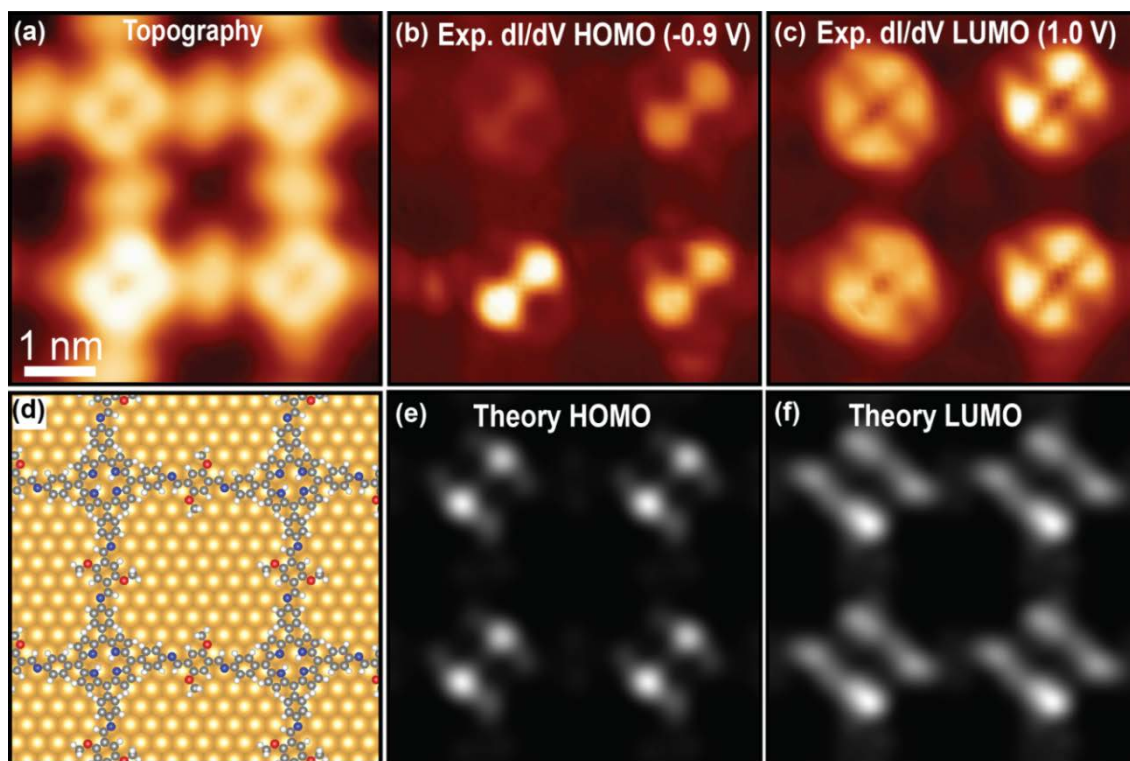


Figure 4.4 Spatial distribution of COF366-OMe electronic states. (a) STM topographic image shows zoom-in view of COF366-OMe ($V_s = 1.0$ V, $I_t = 60$ pA). Experimental dI/dV maps for (b) the COF HOMO at -0.90 V and (c) the COF LUMO at $+1.00$ V (open feedback parameters: $V_s = -0.90$ V for HOMO and $+1.00$ V for LUMO, $I_t = 60$ pA; modulation voltage $V_{rms} = 10$ mV). (d) DFT-optimized adsorption geometry of COF366-OMe on Au(111) surface. Simulated LDOS maps of COF366-OMe on Au(111) for (e) HOMO state and (f) LUMO state.

The spatial wavefunction distribution of the COF366-OMe HOMO and LUMO states was measured by dI/dV mapping conducted at their corresponding peak energies. Figure 4.4(a) shows an STM topographic image of the COF segment on which dI/dV mapping was performed. As shown in Figure 4.4(b) and 4.4(c), experimental HOMO and LUMO dI/dV maps both have significantly higher intensity on the TAPP cores than on the DMA linkers. The COF LUMO state exhibits a four-lobe structure with two nodal lines while the HOMO state exhibits a smaller “dumbbell” shape with bright intensity near the LUMO nodal region. There is some resemblance between the COF HOMO/LUMO states and the isolated TAPP precursor molecule HOMO/LUMO states (Figure 4.1), but the COF states are more symmetric. We note that the “dumbbells” of the COF HOMO can be misaligned between adjacent porphyrin cores.

4.1.4 Theoretical Calculations and Comparisons to Experimental Results

We first performed a series of DFT-PBE calculations aimed at understanding the origin of the electronic structure observed in our experiments. The initial calculations focused on isolated TAPP molecules (*i.e.*, core molecules with zero DMA linkers) as well as the full, periodic COF366-OMe network (*i.e.*, core molecules with four DMA linkers) in the absence of substrate effects (*i.e.*, the “freestanding” limit). After optimization both systems contained a planar central porphine macrocycle with the four phenyl rings twisted with dihedral angles ranging from 60° to 67° with respect to the central plane. The energies of the HOMO and LUMO states for the isolated TAPP molecule and the COF366-OMe network are plotted in Figure 4.3(d) where zero energy represents the vacuum level. The formation of COF366-OMe results in a LUMO downshift of 0.57 eV and a HOMO downshift of 0.29 eV compared to the isolated TAPP molecule. Formation of the COF thus leads to an energy downshift similar to what is seen experimentally, but the calculation also shows an energy gap reduction. This reduction is not observed in the experiment owing to the interactions of the TAPP and COF monolayers with the Au(111) surface (*vide infra*). Although these calculations were performed at the standard DFT-PBE level, which tends to underestimate absolute HOMO-LUMO gaps, the observed relative energy level shifts due to covalent bonding to the DMA linkers are consistent with our STS measurements. This energy-level downshift is explained by the fact that the amine ($-\text{NH}_2$) group of the isolated TAPP molecule is relatively electron-rich (*i.e.*, electron-donating) whereas the imine ($-\text{C}=\text{N}-$) group of the COF is more electron-poor (*i.e.*, electron-withdrawing). As a result, the transition from amine to imine due to the condensation reaction decreases electron density within the porphyrin core, thereby electrostatically shifting the frontier orbital energies downwards. This was further confirmed by the results of calculations on the electronic structure of a TAPP molecule bonded to a single DMA linker using a localized (atomic) basis set, where a clear downshift is observed again in the frontier orbitals of the combined TAPP+DMA system

compared to isolated TAPP molecules.

To better understand the spatial wavefunction properties of these molecular systems, we extended the DFT calculations for both individual TAPP molecules and COF366-OMe networks to include contact with a Au(111) substrate. These calculations show that the interaction between an isolated TAPP molecule and the underlying Au(111) substrate leads to a “saddle-like” structure, where the four pyrrole rings in the porphine macrocycle tilt alternately up and down so as to maximize the nitrogen-gold interactions (the equilibrium geometry has all four porphine nitrogens nearly on top of four Au atoms in the top layer of the Au(111) surface). This is in agreement with earlier results on other porphyrin derivatives [134-136]. After COF formation on the Au(111) surface, the porphine macrocycles are observed to retain the saddle structure. This distortion of the porphyrin core leads to a much stronger charge localization on the β - β C-C bond of the two up-tilted pyrrole rings compared to the β - β C-C bond of the two down-tilted pyrroles, resulting in the dumbbell shape of the COF HOMO state (Figure 4.4(e)). In contrast, the calculated LDOS of the LUMO state (Figure 4.4(f)) displays a nearly four-fold symmetric distribution on the TAPP core, in reasonable agreement with the four-lobe structure observed in the COF dI/dV map (Figure 4.4(c)) (some discrepancy does exist between theoretical and experimental maps, likely due to differences in tip trajectory since the experimental dI/dV maps were taken along a surface of constant-current feedback while the theoretical simulation shows LDOS intensity taken along a plane at fixed distance above the COF). Inclusion of the substrate in our calculations also results in the HOMO-LUMO gap remaining constant for isolated TAPP molecules compared to a fully formed COF, thus explaining why we do not experimentally observe the gap reduction predicted by the “freestanding” calculations.

We note that although the core dominates both the experimental and theoretical LUMO LDOS images shown in Figure 4.4, some LUMO state density does still extend across the DMA linker. The reason the core dominates the LUMO maps of Figure 4.4 is because the STM tip is relatively far from the surface (~ 4 Å) and the core LDOS is much greater than the linker LDOS at this distance. This is partly due to the fact that the phenyl rings of the core twist away from the Au surface by 35° (leading to the four brightest spots in the simulated LUMO dI/dV map) whereas the DMA linkers lie flat.

4.1.5 Summary

To summarize, we have characterized the local electronic structure of a single-layer porphyrin-containing square-lattice COF on Au(111), namely COF366-OMe. Energy shifts of the frontier orbitals of the porphyrin core are observed upon COF formation due to the electron withdrawing nature of the imine linkages. The experimentally measured HOMO and LUMO wavefunctions of the COF have highest intensity on the porphyrin cores and exhibit an energy gap of 1.98 ± 0.04 eV. DFT-based electronic local density of states simulations are consistent

with our experimental data and confirm that substrate-induced buckling observed for isolated porphyrins persists in COF networks. This provides insight into how the electronic structure of molecular nanostructures is affected by forming covalent bonds between monomer components.

4.2 Asymmetrical Bonding Scheme: TAPP-TFPP-COF

The core-linker geometry of COF366-OMe dictates that all porphyrin cores in the COF are in the same chemical environment. As we were brainstorming for interesting COF structures, the idea of creating intra-COF heterostructures came up. We thought that such heterojunctions might be realized in a porphyrin-containing COF where every pair of adjacent porphyrin cores consists of one metallated porphyrin and one unmetallated porphyrin. We went ahead and synthesized such a COF, and STS measurements showed that there is indeed an offset in orbital energies between adjacent porphyrin cores. However, when doing a control experiment where every pair of adjacent porphyrin cores consists of both unmetallated porphyrins, we found that the offset in orbital energies still persists, and with a similar magnitude. Theoretical calculations performed by our collaborator helped us pinpoint the origin of the energy offset; it turns out that incorporation of metal atoms into porphyrin cores does not have a big effect on the energy alignment; rather it is the asymmetrical linkage between adjacent porphyrin cores that is responsible for the energy offset and formation of heterojunctions.

The work described below is based on a manuscript we are preparing for publication.

4.2.1 Synthesis of TAPP-TFPP-COF on Au(111) Surface

A modification to the molecular precursors used to synthesize COF366-OMe was necessary to create a new COF with an “asymmetrical bonding scheme”. While TAPP molecule (Figure 4.1(b) inset) stays as one of the precursor, DMA molecule (Figure 4.2(a) inset) is replaced by (5,10,15,20-tetrakis (4-formylphenyl) porphyrin, or TFPP. Figure 4.5(a) shows the Schiff-base condensation reaction between TAPP and TFPP. The two molecules are identical except for the functional groups at the four ends: TAPP is functionalized with amine groups whereas TFPP is functionalized with aldehyde groups. The Schiff-base condensation reaction results in a 2D COF network of alternating porphyrin cores A and B connected through imine linkages. The core A originates from TAPP whereas the core B originates from TFPP, and both cores are almost the same except for the directionality of the imine bonds connected to them. For instance, if we start to move out from the center of any core A within the COF network, we will always encounter the nitrogen atom of the imine linkage first. On the other hand, if we start to move out from the center of any core B we will always encounter the carbon atom of the imine linkage first. Therefore, each porphyrin core exists in a different chemical bonding environment than its four nearest neighbors.

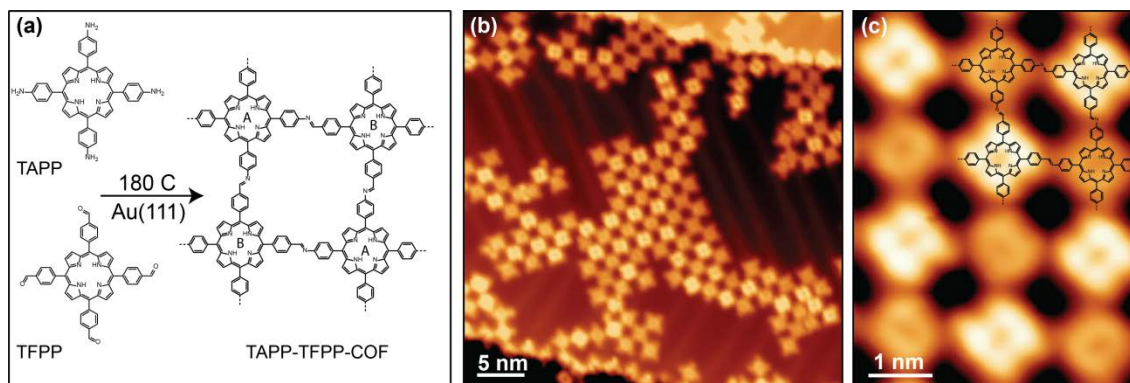


Figure 4.5 Synthesis and STM imaging of TAPP-TFPP-COF on Au(111). (a) Schematic for the synthesis of TAPP-TFPP-COF from molecular precursors. (b) Representative large-scale STM topographic image of TAPP-TFPP-COF on Au(111) showing the “checker board” pattern. ($V_s = 0.8$ V, $I_t = 10$ pA). (c) Zoomed-in STM image of the COF with the chemical structure overlaid on the top-right corner ($V_s = 0.8$ V, $I_t = 10$ pA).

The synthesis of this single layer COF was carried out on a Au(111) surface in UHV. TFPP molecules were first deposited onto the surface followed by the deposition of TAPP molecules. The mixture of two precursor molecules was then annealed to 180 °C for 1 hour to induce the condensation reaction leading to formation of the COF. Figure 4.5(b) shows a STM topographic image of the single layer COF, which we name as “TAPP-TFPP-COF”. Under the chosen tunneling condition (see Figure 4.5 caption), square lattice patches with a unique “checker board” pattern can be seen, indicating the alternation of two distinct porphyrin cores. The unit cell size determined from STM imaging is 2.7 nm, consistent with the theoretically calculated unit cell size for the structure shown in Figure 4.5(a). Figure 4.5(c) shows a zoomed-in image of a COF patch with the chemical structure overlaid on the top right corner. We assign the darker porphyrin cores as core A (originated from TAPP molecules) and brighter porphyrin cores as core B (originated from TFPP molecules).

4.2.2 Local Electronic Structure of TAPP-TFPP-COF Measured by STM

The local electronic structure of TAPP-TFPP-COF was characterized by dI/dV point spectroscopy at different positions on the 2D COF marked in Figure 4.6(a) (the positions are marked by color-coded “X” that corresponds to different spectra in Figure 4.6(b)). The black curve in Figure 4.6(b) shows the spectrum taken on a bare Au(111) region, and the feature around -0.5 V is the well-known Au(111) Shockley surface state. The blue curve (Figure 4.6(b)) represents a characteristic dI/dV point spectrum recorded on the core A (from TAPP) of the COF,

whereas the red curve represents a characteristic dI/dV point spectrum recorded on the neighboring core B (from TFPP). The orbitals of the core A are evidently shifted up in energy relative to the orbitals of the core B, indicating the successful realization of type II heterojunction within the single layer 2D COF. The blue spectrum exhibits a peak at $V_s = 1.03$ V, which we identify as the conduction band (CB) +1 state, as well as a peak at $V_s = -1.13$ V identified as the valence band (VB) edge of the COF. On the other hand, the red spectrum exhibits a peak at $V_s = 0.75$ V, which we identify as the CB edge, as well as a peak at $V_s = -1.39$ V identified as the VB-1 state of the COF (V_s is the sample voltage). This leads to an overall bandgap of 1.88 eV. We have taken many spectra on different porphyrin cores and within different patches of the COF, and they all have peaks at similar energies as those shown in Figure 4.6(b), depending on whether it is a core A or core B.

The spatial wave function distribution of TAPP-TFPP-COF's heterojunction energy states were investigated experimentally by recording dI/dV maps at the corresponding peak energies (Figure 4.6(c)-(f)). Figure 4.6(a) shows the STM topographic image of the COF patch on which dI/dV maps were recorded. Figure 4.6(c) shows the dI/dV map obtained at the CB energy, where significant LDOS is concentrated on core B (from TFPP) in the COF, and the LDOS pattern exhibits a four-lobe structure with two orthogonal nodal lines through the center of the porphyrin core. At this energy, the core A (from TAPP) within the COF does show slight LDOS intensity, which is consistent with the weak intensity of the dI/dV signal on core A (blue curve in Figure 4.6(b)). Figure 4.6(d) shows the dI/dV map recorded at the VB energy. This map displays marked LDOS on core A in the COF, and the LDOS pattern exhibits a "dumbbell" like structure. We note that a few core A sites in the map do not show notable LDOS. This is because the peak energy of the VB state measured at different core A sites is highly sensitive to the number of its nearest core B neighbors. Figure 4.6(e)-(f) show dI/dV maps recorded at CB+1 and VB-1 energies, with higher LDOS intensity on core A (from TAPP) and core B (from TFPP) respectively. The LDOS pattern of CB+1 (VB-1) on a single porphyrin core is similar to that of CB (VB), and is consistent with the LDOS pattern of the unoccupied (occupied) state previously reported for COF366-OMe [68]. Combining the results of dI/dV point spectra and maps, it is evident that this single layer TAPP-TFPP-COF contains a grid of atomically precise type II heterojunctions due to the asymmetrical bonding environments of adjacent porphyrin cores.

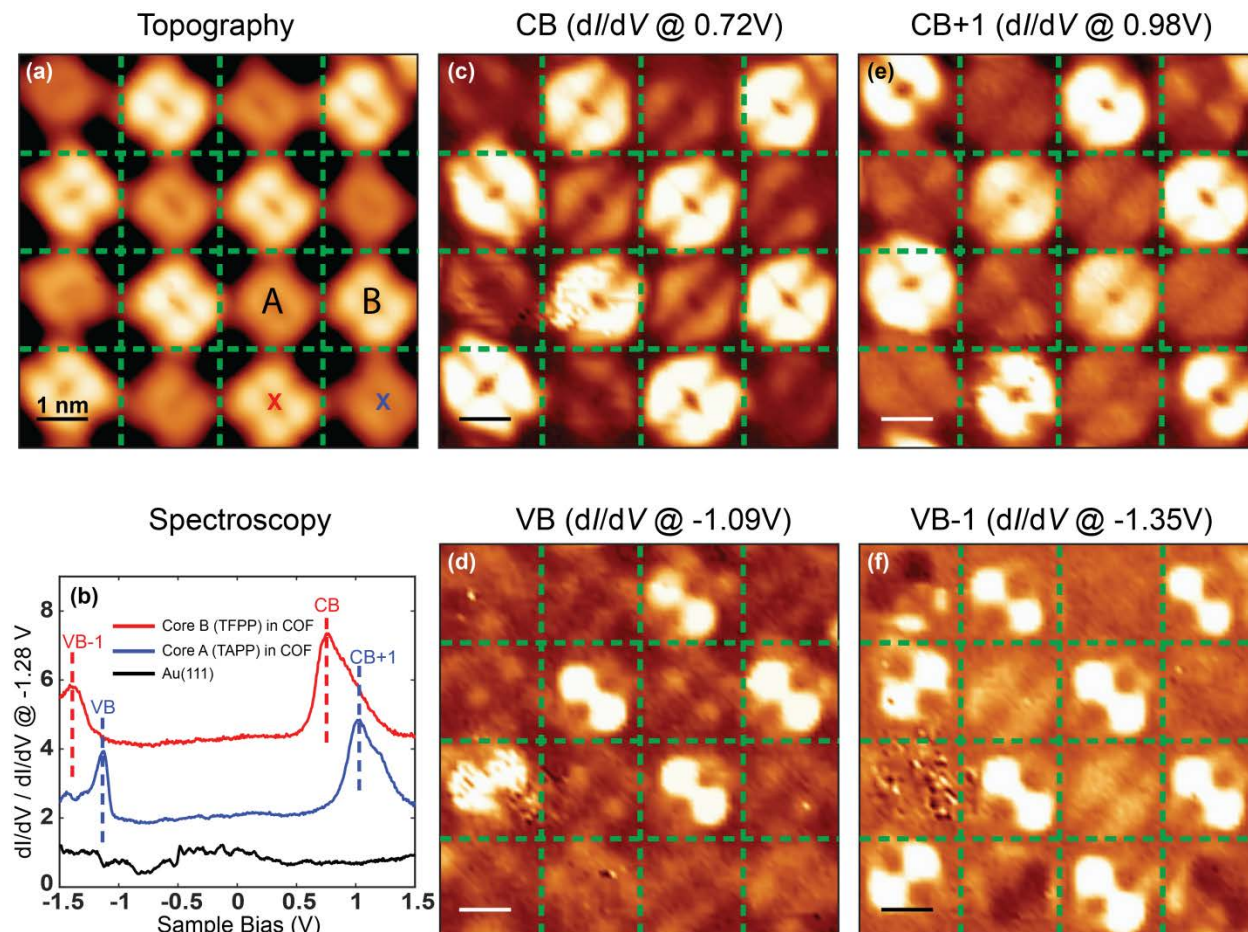


Figure 4.6 Local electronic structure of TAPP-TFPP-COF measured by STS and dI/dV mapping. (a) Zoomed-in STM image of a TAPP-TFPP-COF patch consisting of 16 porphyrin cores ($V_s = 0.80 \text{ V}$, $I_t = 10 \text{ pA}$). Red and blue crosses indicate the positions at which dI/dV spectra were recorded. (b) dI/dV spectra taken on top of the core B (from TFPP, red curve) and the core A (from TAPP, blue curve) in the COF patch shown in (a). The black curve is a reference spectrum taken on bare Au(111) surface. Each curve is normalized by its own value at $V_s = -1.28 \text{ V}$, and the red (blue) curve is upshifted by 4 (1.75) a.u. for clarity (open feedback parameters: $V_s = 0.8 \text{ V}$, $I_t = 20 \text{ pA}$ for all three curves, modulation voltage $V_{\text{rms}} = 10 \text{ mV}$). (c)-(f) Experimental dI/dV maps for different COF states: (c) CB at $+0.72 \text{ V}$, (d) VB at -1.09 V , (e) CB+1 at $+0.98 \text{ V}$, and (f) VB-1 at -1.35 V (open feedback parameters: $V_s = 0.72 \text{ V}, -1.09 \text{ V}, 0.98 \text{ V}, -1.35 \text{ V}$ for CB, VB, CB+1, VB-1 respectively, $I_t = 20 \text{ pA}$, modulation voltage $V_{\text{rms}} = 10 \text{ mV}$).

4.2.3 Theoretical Calculations and Comparisons to Experimental Results

To better understand the experimentally observed wave function localization and energy level offset in TAPP-TFPP-COF, we performed DFT calculations for the COF/Au system. The optimized structure of TAPP-TFPP-COF on the Au(111) surface is shown in Figure 4.7(a). The two dashed lines in the figure slice it into four unit cells, with the center of each unit cell occupied by the core A (from TAPP) and the four corners occupied by the core B (from TFPP). The calculations show that all porphyrin cores within TAPP-TFPP-COF undergo a saddle-like deformation due to interaction with the underlying Au(111) substrate, similar to our previous report of COF366-OMe [68] and reports for other porphyrin derivatives [134-136]. In particular, we confirmed that such a deformed saddle-like geometry represents a global energy minimum for the adsorption of TAPP-TFPP-COF on the Au(111) surface which can only be achieved when the four nitrogen atoms in the porphyrin core are nearly on top of four surface Au atoms with the average N-Au distance calculated at ~ 3.6 Å. The saddle-like deformation is critical for the formation of the two-fold symmetric dumbbell shape of VB and VB-1 states (Figure 4.6(d) and (f)).

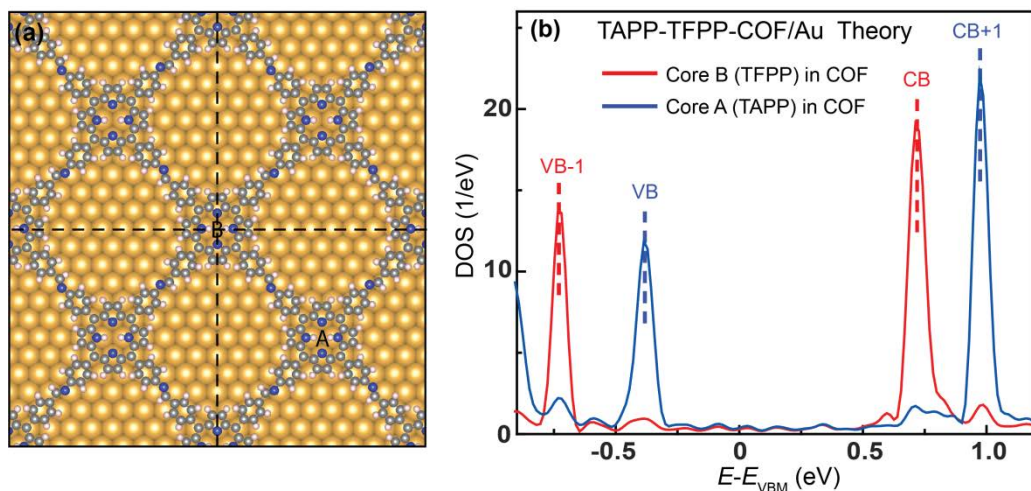


Figure 4.7 Structure of TAPP-TFPP-COF/Au(111) and PDOS calculated by DFT. (a) DFT-optimized adsorption geometry of TAPP-TFPP-COF on the Au(111) surface. The dashed lines divide the figure into four unit cells. (b) Theoretical PDOS calculated for TAPP-TFPP-COF/Au(111) system.

The theoretical projected density of states (PDOS) of the core A and core B within the

COF/Au(111) system are plotted in Figure 4.7(b). The core A (blue curve) shows two prominent peak corresponding to the VB and CB+1 states whereas the core B (red curve) shows two prominent peak corresponding to the VB-1 and CB states. The energy level upshift of the core A states compared to the core B states is consistent with experimental results (see Figure 4.6(b)). We note that the calculated VB-CB gap is 1.1 eV (peak to peak), which is about 0.8 eV smaller than the experimental value, due to underestimation of quasiparticle band gaps usually observed in DFT calculations. Interestingly, the DFT-calculated relative energy shift between VB and VB-1 is about 0.30 eV (Figure 4.7(b)), which is in good agreement with the experimentally observed energy shift of 0.26 eV (Figure 4.6(b)). Similar trend is also observed for the energy shift between CB and CB+1.

The spatial distribution of the COF states was characterized by calculating the partial charge density corresponding to the CB and VB peaks shown in Figure 4.7(b). The partial charge density plot for the COF CB minimum (Figure 4.8(a)) displays a 4-fold symmetric distribution on core B (from TFPP), consistent with the experimental dI/dV map of Figure 4.6(c). We note that core A (from TAPP) at the CB minimum does exhibit very slight intensity of LDOS, similar to what was observed experimentally. In contrast, the partial charge density plot for the COF state at the VB maximum displays LDOS distribution exclusively on core A (from TAPP) (Figure 4.8(b)), in reasonable agreement with the experimental dI/dV map of Figure 4.6(d). Similarly, the partial charge density plot for the CB+1 (VB-1) state exhibits localization of LDOS on the core A (core B) within the COF.

4.2.4 Hirshfeld Charge Analysis and Dipole-Induced Energy Shift

To further understand the origin of the energy level offset observed in both the experimental measurements and DFT calculations, we studied the charge distribution in the freestanding TAPP-TFPP-COF monolayer using the Hirshfeld charge analysis implemented in Tkatchenko-Scheffler method [137] in Vienna Ab initio simulation package (VASP) [138, 139]. The summed Hirshfeld charge on the core A and core B (including the porphyrin macrocycle and the four phenyl groups) are $+0.056 |e|$ and $+0.168 |e|$, respectively, indicating the electron-withdrawing role of the imine linkages and a charge redistribution upon COF formation. More importantly, the calculated Hirshfeld charge on the N and C atoms of the imine group are $-0.128 |e|$ and $0.036 |e|$ respectively, consistent with the fact that the N atom has a higher electronegativity than the C atom. Such charge distributions on N and C atoms can be effectively thought of as a dipole pointing from N to C. The energy level alignments of the TAPP-TFPP-COF, either as a freestanding monolayer or when supported by the Au(111) substrate, can thus be understood from the simplified electrostatic interactions between a point charge $-|e|$ localized on the porphyrin macrocycles and the dipole field of the imine bonds.

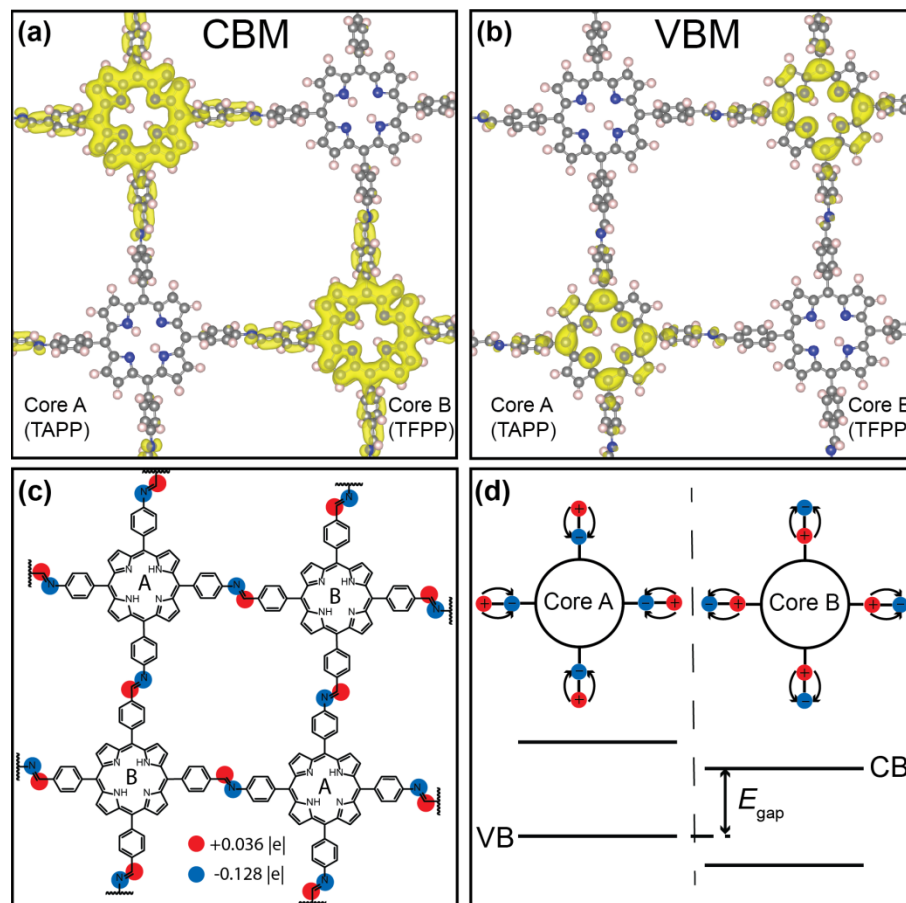


Figure 4.8 Partial charge density plots and Hirshfeld charge analysis of TAPP-TFPP-COF. (a)-(b) Partial charge density plots for freestanding TAPP-TFPP-COF at (a) CBM and (b) VBM. The iso-surface is $0.0008 \text{ e}/\text{\AA}$. (c) Charge distribution of the imine bonds calculated by Hirshfeld charge analysis, showing the formation of effective dipoles. (d) A simplified picture showing the effect of the imine dipoles on the energy offset between adjacent porphyrin core A and core B.

As illustrated in Figure 4.8(d), a point charge $-|e|$ located at either the core A or core B within the COF is influenced by the electric field originating from the four dipoles affiliated with the imine bonds around the core. For the point charge $-|e|$ located at core A (from TAPP), the electric field from the four imine-bond dipoles are pointing towards the center, thus its electrostatic energy will be changed by $\Delta E_A = +4(|e| \cdot |p|)/(r^2 - \frac{d^2}{4})$, where p represents the magnitude of the dipole moment associated with an imine bond, r the distance from the center of the dipole to the point charge (which is approximated to be located at the center of the porphyrin core), and d the length of the dipole (we assume that r and d are along the same direction). On the other hand, for a point charge $-|e|$ located at core B (from TFPP), the electric

field from the four dipoles are pointing away from the center, hence its electrostatic energy will be changed by $\Delta E_B = -4(|e| \cdot |p|)/(r^2 - \frac{d^2}{4})$. Therefore, an energy difference of $\Delta E = +8(|e| \cdot |p|)/(r^2 - \frac{d^2}{4})$ is expected between two point charges (each with charge $-|e|$) located at the core A and core B of the COF. Due to the unequal amount of charge on N and C atoms, we approximate the dipole moment $p = \frac{|q_C - q_N|}{2} \cdot d$. Plug in all the relevant quantities derived from DFT calculations and Hirshfeld charge analysis, we end up with an energy difference ΔE of 0.13 eV. Compared to the DFT value of 0.35 eV and experimental value of 0.26 eV (energy difference between VB and VB-1), we believe such a value is reasonable due to rough approximations involved in the analysis.

4.2.5 Summary

In summary, we have successfully synthesized a single layer porphyrin-containing imine-coupled square lattice COF with atomically precise heterojunctions that spread through the entire COF. Characterization of the COF *via* STM/STS measurements reveals an asymmetrical bonding environment for each pair of adjacent porphyrin cores, leading to the spatial separation of CB and VB states to different set of porphyrin cores. DFT calculations are consistent with our experimental data and confirm the formation of such unique heterojunction between each pair of neighboring porphyrin cores within the COF. Hirshfeld charge analysis attributes the observation of the heterojunction states to the dipole fields associated with the imine linkages in the COF. This peculiar type of single-layered 2D material with a lattice of atomically precise heterojunctions spreading throughout the entire material will potentially be integrated into future nanoscale opto-electronic devices.

4.3 Conclusion and Outlook

We have shown that Schiff-base condensation reactions can be utilized for the synthesis of imine linkage 2D COFs on the Au(111) surface. The formation of imine linkages has a significant effect on the electronic structures of the COFs. In the case of COF366-OMe, the electron-withdrawing nature of imine bonds results in a downward shift of frontier orbital energy levels of the COF compared to that of the precursor molecule TAPP. In the case of TAPP-TFPP-COF, the directionality of the imine bonds leads to an asymmetrical bonding environment between two adjacent porphyrin cores, and the effective dipole associated with the imine linkages gives rise to the orbital energy offset due to electrostatic interactions. The understanding of how the linkages of 2D COFs affect their electronic structures is crucial to the field of COF research and will guide the synthesis and application of new COF materials.

2D COFs are a promising class of materials to study exotic physics. For instance, in a quite general sense, graphene can be regarded as a 2D COF that consists of a 2-atom basis. It is not unreasonable to expect that other 2D COFs might have similar (or even more) exotic properties as graphene, thanks to the potentially inexhaustible collection of functional molecular building

blocks. Indeed, theory has predicted the existence of Dirac cones in several 2D COFs, and in some cases the Dirac cone is right at the Fermi level just like in graphene [140]. On the other hand, flat bands due to destructive quantum interference are an ideal platform to study strongly correlated electronic states, such as magnetism, superconductivity, and Wigner crystallization [141]. Two exemplary lattices that host such flat bands are the Lieb lattice [142] and the Kagome lattice [143], both of which can be achieved under the scope of 2D COFs/MOFs. Although the study of 2D COFs is a relatively young research field, I am certain that the close collaboration among chemists, material scientists, and physicists will pave the way for the discovery of interesting new 2D nano-materials with exotic physical properties.

Chapter 5

Molecular Species

This chapter discusses some novel molecular species that I studied with STM on a surface. The researchers who contributed to these studies are Chen Chen, Zahra Pedramrazi, Trinity Joshi, Dr. Cameron Rogers, Dr. Dan Lehnerr, Dr. Zhi Cao, Dr. Arash A. Omrani, Dr. Hsin-Zon Tsai, Han Sae Jung, Dr. Song Lin, Nick Lau, Bobby Ge, Lingjie Zhou, Eric Yu, Dr. Catherine R DeBlase, Joaquin M Alzola, Dr. Ivan Keresztes, Dr. Emil B Lobkovsky, Dr. William R. Dichtel, Dr. Felix Fischer, and Dr. Michael F. Crommie.

5.1 Surface-Assisted Synthesis of Peripentacene

When trying to synthesize $N=11$ AGNR from a molecular precursor (13,13'-dibromo-6,6'-bipentacene), we found that an intra-molecular reaction instead of an inter-molecular coupling occurred on the surface of Au(111). It is based on this unexpected result that we were able to synthesize the target molecule of peripentacene, which had long eluded solution-based synthesis by organic chemists.

The work described here was originally published in “Angewandte Chemie International Edition” [144].

5.1.1 Background on Periacenes

The novel optical and electronic properties emerging from quantum confinement effects in nano-graphene has inspired the development of novel strategies toward the rational synthesis of atomically defined nano-graphenes [145]. Among these structures, polycyclic aromatic hydrocarbons (PAHs) featuring uniform edges, *i.e.*, acenes or periacenes, are privileged scaffolds [146, 147]. Their pursuit is further motivated by a fundamental interest in the exotic physical properties associated with atomically precise boundaries in single-layer graphene [148-151]. n -Periacenes (**1**; Figure 5.1) are derived from the lateral fusion of two linear acenes at the peri-positions (n denotes the number of annulated rings formed through the lateral fusion) into rectangular nano-graphene flakes. The structure of n -periacene ($n > 1$) exhibits pairs of parallel zig-zag (long-edge) and armchair (short-edge) edges terminated with hydrogen atoms. While the smallest members of this family, perylene ($n = 1$) and bisanthrene ($n = 2$) have been studied for

decades [152-154], the slightly longer peritetracene ($n = 3$) and peripentacene ($n = 4$) have not been prepared through rational synthesis [155-158]. Recent resurgent interest in extended n -periacenes has been spurred by theoretical calculations which predict a substantial decrease of the HOMO–LUMO gap upon extending the length of the n -periacene, as well as an antiferromagnetic ground state featuring spin localization along opposing zig-zag edges [6, 149].

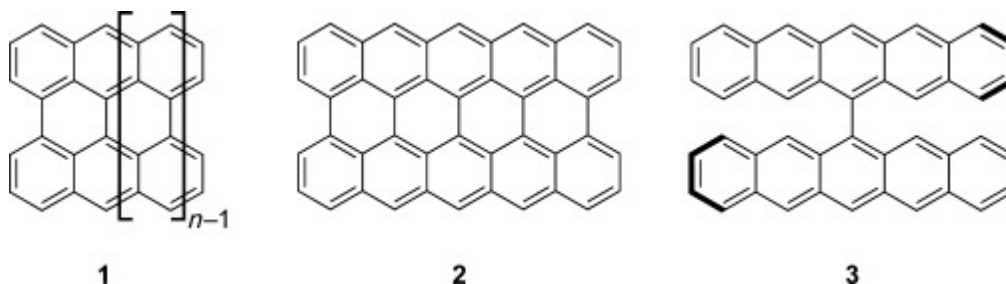


Figure 5.1 Chemical structure of n -periacene **1**, peripentacene **2**, and 6,6'-bipentacene **3**.

Several solution-based synthetic strategies toward elongated acenes have been reported, yet the fully cyclized n -periacenes ($n > 2$) could not be isolated from these reactions [155, 159-161]. This has been attributed to the inherent insolubility and unusual reactivity of unsubstituted acenes, as well as their thermal and photochemical instability due to a small band gap and significant contributions from resonance structures involving radical character [147, 148, 155, 159]. In particular, experimental signatures for peripentacene (**2**) have only been suggested by mass spectrometry as a potential side product of the thermal decomposition of pentacene, but there has been no structural confirmation for its existence.

5.1.2 Synthesis of Peripentacene on a Au(111) Surface

Solid crystals of bipentacene **3** (Figure 5.1) were prepared by our collaborator through four steps of solution synthesis. The purified molecule was then sublimed at 260 °C onto a Au(111) substrate held at room temperature (24 °C) in UHV. Thermally induced cyclodehydrogenation on Au(111) yield surface stabilized, rectangular flakes of peripentacene **2**. STM of both the precursor **3** and the product peripentacene **2** reveal the superb selectivity and almost quantitative yield of the intramolecular cyclization process. Atomic-resolution imaging using nc-AFM reveals the detailed structure of peripentacene **2**.

Figure 5.2(a) reveals that as-deposited bipentacene **3** assembles into islands of highly ordered linear chains on the Au surface. The average apparent height of alternating bright spots along a line of self-assembled molecules is 0.26 ± 0.01 nm. The zigzag appearance of the molecule self-assembly is associated with the preferred dihedral angle adopted between two pentacene subunits in **3** when adsorbed onto the surface (see inset of Figure 5.2(a)). Annealing

the sample of bipentacene **3** on Au(111) at 200 °C for 30 min induces a cyclodehydrogenation of all peri-positions to form the fully cyclized peripentacene **2**. A representative STM image of **2** (Figure 5.2(b)) reveals a sub-monolayer coverage of the surface with uniform discrete rectangular flakes. The apparent length, width, and height, 1.75 ± 0.04 nm, 1.25 ± 0.04 nm, and 0.21 ± 0.01 nm respectively, match the expected molecular dimensions of peripentacene **2**. Figure 5.2(b) shows a typical STM image illustrating the high yield and remarkable selectivity of the intra-molecular cyclodehydrogenation reaction, as fewer than 5% of the adsorbed molecules deviate from the expected rectangular shape.

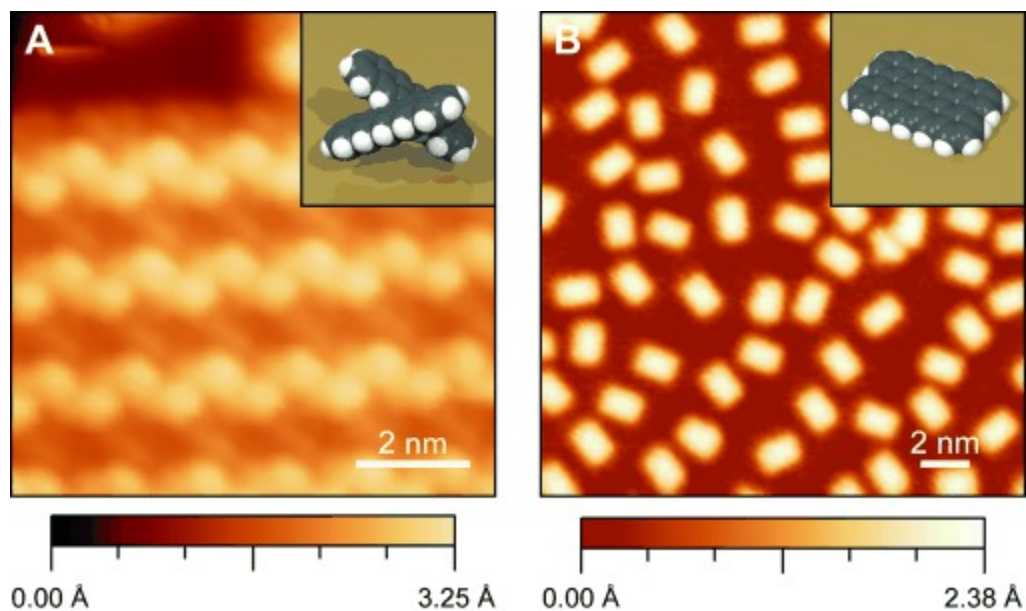


Figure 5.2 STM images of bipentacene and peripentacene. (a) Constant current STM image of bipentacene **3** as deposited on Au(111) ($I_t = 10$ pA, $V_s = 0.80$ V, $T = 7$ K). (B) Constant current STM image of peripentacene **2** on Au(111) after annealing at 473 K for 30 min ($I_t = 10$ pA, $V_s = 0.80$ V). Molecular models are shown in insets.

To unequivocally assign the structure of the cyclization product **2** we performed bond-resolved qPlus nc-AFM imaging using a low-temperature commercial Omicron LT-STM/AFM [162-165]. The apex of the gold-coated tungsten STM tip was functionalized with a single CO molecule prior to imaging. Contrast in nc-AFM images arises from the frequency shift of the qPlus sensor while scanning over the molecule in constant height mode. Unlike the diffuse STM topographic image (Figure 5.3(a)), which reflects frontier orbital LDOS, the nc-AFM image (Figure 5.3(b)) reveals not only the exact position of carbon atoms but also the intra-molecular bonds forming the aromatic carbon skeleton of peripentacene **2**. Figure 5.3 clearly shows the two parallel-aligned zigzag edges of peripentacene **2** that are predicted to lead

to exotic electronic/magnetic behavior in extended periacenes. The interaction of peripentacene with the free valences of the Au(111) surface stabilize this highly reactive molecule and prevent undesired radical side reactions that have thus far prevented the isolation of **2** from solution-based reactions.

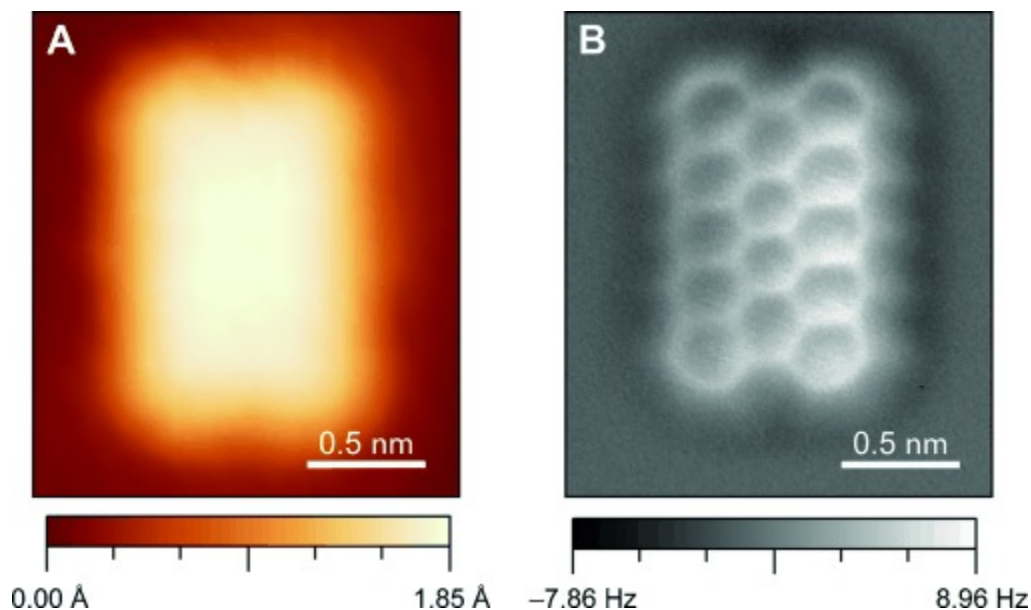


Figure 5.3 STM and nc-AFM images of a single peripentacene **2.** (a) Constant current STM image of a single peripentacene **2** ($I_t = 100$ pA, $V_s = 0.55$ V, $T = 4.5$ K). (B) nc-AFM image of the same molecule (qPlus resonance frequency = 28.73 kHz, $Q = 8 \times 10^4$, oscillation amplitude = 50 pm).

5.1.3 Summary

In summary, we report the first successful preparation of peripentacene **2** and its detailed characterization by STM and bond-resolved nc-AFM. Surface-assisted cyclodehydrogenation produces peripentacene from 6,6'-bipentacene precursor in excellent yields and high selectivity. This synthetic method has the potential to provide access to the experimental investigation of extended acenes predicted to exhibit exotic ground state electronic configurations. Periacenes and related materials, long the subject of only theoretical investigation, are now more accessible for practical study and application.

5.2 On-Surface Nano-Graphene Synthesis from *ortho*-Arylene Precursors

The work presented in the preceding section (section 5.1) made us realize that on-surface synthesis was a powerful tool to achieve otherwise elusive molecular targets. With this idea in mind, we were able to attain another “nano-graphene” species, which I will describe briefly. The work described here is part of a published manuscript in “Chemical Science” [166].

The reaction scheme is shown in Figure 5.4. Starting from *ortho*-arylene precursor which was synthesized by our collaborator, the oxidative cyclodehydrogenation on a Au(111) surface enables the formation of a “nano-graphene” species, which has the same width as a N=8 AGNR. The synthetic strategy for the precursor *ortho*-arylene leads to potential selective functionalization of the armchair edges with one edge of the ribbon being halogenated while the opposing edge being hydrogen terminated.

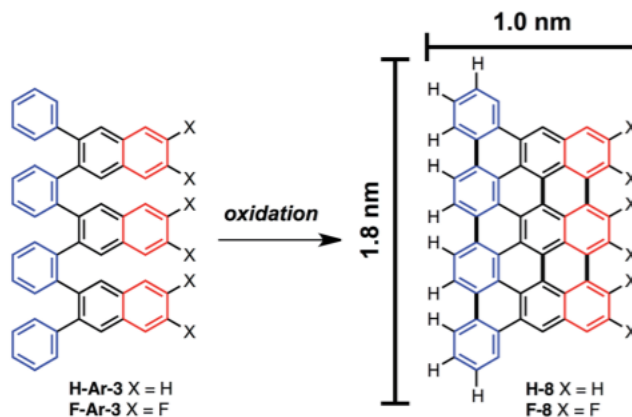


Figure 5.4 Reaction scheme from *ortho*-arylene to nano-graphene. *o*-Arylenes as precursors to nano-graphenes H-8 and F-8 with control of width and length dimensions in addition to potential control of edge-functionalization. Dimensions shown are estimated for H-8 based on DFT calculations and measurements between the furthest hydrogen atoms.

In particular, evaporation of H-Ar-3 molecules in UHV enabled its deposition onto Au(111). The STM image in Figure 5.5(a) illustrates a surface coverage of 0.8 monolayers of H-Ar-3 on Au(111). The molecules are seen to form ordered crystalline domains approaching *ca.* 20 nm (a diagonal grain boundary separating two such domains is visible in Figure 5.5(a)). At lower surface coverage, H-Ar-3 selectively attaches to step edges of Au(111) (Figure 5.5(b)). A close up of several molecules (Figure 5.5(c)) clearly shows the non-planarity of H-Ar-3, which exhibits an apparent height of 3 – 5 Å depending on molecular conformation.

Upon annealing the H-Ar-3/Au(111) sample to 286 °C, a change in the shape of the molecules is observed consistent with conversion to H-8. Figure 5.5(d) shows the dominant

product (60%): a planar, trapezoidal molecule with measured height of $1.9 \pm 0.1 \text{ \AA}$. The dimensions of this structure ($1.9 \pm 0.2 \text{ nm} \times 1.3 \pm 0.2 \text{ nm}$) are consistent with DFT predicted dimensions of H-8 (Figure 5.5(e)). It should be noted that an intermediate annealing temperature of 250 C is enough to convert some molecules (10%) to the desired H-8 product, but with the remaining sample still consisting of non-planar molecules.

5.3 Conclusion

We have shown the on-surface synthesis of two new “nano-graphene” species, the structure of which is characterized by STM and nc-AFM. Elusive target molecules that are difficult to obtain from traditional solution-based organic synthesis can be achieved through surface-assisted synthesis, as intra-molecular cyclodehydrogenation induced by thermal annealing results in the fully-fused “nano-graphene” species. Similar mechanisms may lead to the successful syntheses of other polycyclic aromatic hydrocarbons (PAHs), and future experiments are needed to study the scalability of the reactions and the stability of the products outside of UHV.

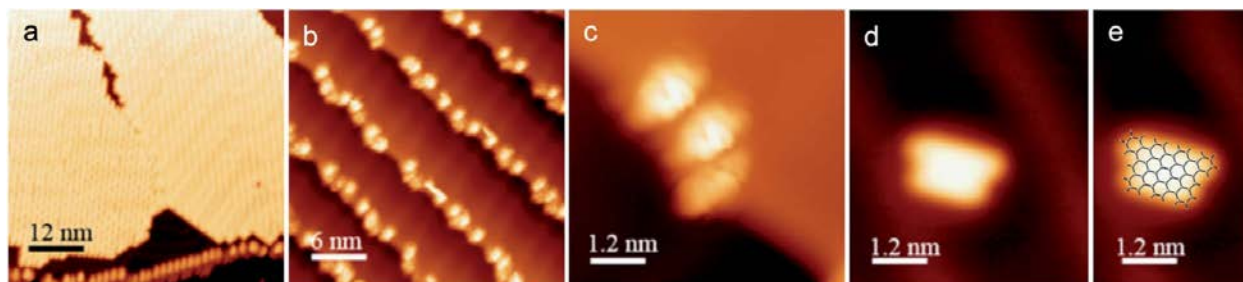


Figure 5.5 STM images of H-Ar-3 and H-8 molecules on Au(111). (a) 0.8 monolayer coverage of H-Ar-3 as deposited shows well-ordered crystalline domains. ($I_t = 10 \text{ pA}$, $V_s = 1.0 \text{ V}$) (b) Lower surface coverage of H-Ar-3 as deposited shows molecular adhesion to step edges of Au(111) crystal. ($I_t = 2 \text{ pA}$, $V_s = 1.0 \text{ V}$) (c) Close-up of several H-Ar-3 molecules before annealing reveals non-planarity. ($I_t = 2 \text{ pA}$, $V_s = 1.0 \text{ V}$) (d) Individual nano-graphene H-8 obtained after annealing to 286 °C. ($I_t = 200 \text{ pA}$, $V_s = 0.1 \text{ V}$) (e) DFT optimized structure of H-8 overlaid on top of STM image of H-8 shown in (d). All images were obtained at $T = 7 \text{ K}$.

Bibliography

1. Ghosh, A. and C.L. Brown. *Electronics for the post-silicon CMOS era...challenges and opportunities*. in *2009 International Semiconductor Device Research Symposium*. 2009.
2. Castro Neto, A.H., et al., *The electronic properties of graphene*. *Reviews of Modern Physics*, 2009. **81**(1): p. 109-162.
3. Allen, M.J., V.C. Tung, and R.B. Kaner, *Honeycomb Carbon: A Review of Graphene*. *Chemical Reviews*, 2010. **110**(1): p. 132-145.
4. Fujita, M., et al., *Peculiar Localized State at Zigzag Graphite Edge*. *Journal of the Physical Society of Japan*, 1996. **65**(7): p. 1920-1923.
5. Nakada, K., et al., *Edge state in graphene ribbons: Nanometer size effect and edge shape dependence*. *Physical Review B*, 1996. **54**(24): p. 17954-17961.
6. Son, Y.-W., M.L. Cohen, and S.G. Louie, *Energy Gaps in Graphene Nanoribbons*. *Physical Review Letters*, 2006. **97**(21): p. 216803.
7. Yang, L., et al., *Quasiparticle Energies and Band Gaps in Graphene Nanoribbons*. *Physical Review Letters*, 2007. **99**(18): p. 186801.
8. Hybertsen, M.S. and S.G. Louie, *Electron correlation in semiconductors and insulators: Band gaps and quasiparticle energies*. *Physical Review B*, 1986. **34**(8): p. 5390-5413.
9. Chen, Y.-C., et al., *Molecular bandgap engineering of bottom-up synthesized graphene nanoribbon heterojunctions*. *Nature Nanotechnology*, 2015. **10**: p. 156.
10. Chen, Y.-C., *Exploring Graphene Nanoribbons Using Scanning Probe Microscopy and Spectroscopy*. 2014, University of California, Berkeley.
11. Han, M.Y., et al., *Energy Band-Gap Engineering of Graphene Nanoribbons*. *Physical Review Letters*, 2007. **98**(20): p. 206805.
12. Kosynkin, D.V., et al., *Longitudinal unzipping of carbon nanotubes to form graphene nanoribbons*. *Nature*, 2009. **458**: p. 872.
13. Jiao, L., et al., *Facile synthesis of high-quality graphene nanoribbons*. *Nature Nanotechnology*, 2010. **5**: p. 321.
14. Li, X., et al., *Chemically Derived, Ultrasmooth Graphene Nanoribbon Semiconductors*. *Science*, 2008. **319**(5867): p. 1229-1232.
15. Cai, J., et al., *Atomically precise bottom-up fabrication of graphene nanoribbons*. *Nature*, 2010. **466**: p. 470.
16. Geim, A.K., *Graphene: Status and Prospects*. *Science*, 2009. **324**(5934): p. 1530-1534.
17. Xu, X., et al., *Spin and pseudospins in layered transition metal dichalcogenides*. *Nature Physics*, 2014. **10**: p. 343.
18. Wang, Q.H., et al., *Electronics and optoelectronics of two-dimensional transition metal*

BIBLIOGRAPHY

- dichalcogenides*. Nature Nanotechnology, 2012. **7**: p. 699.
19. Mak, K.F. and J. Shan, *Photonics and optoelectronics of 2D semiconductor transition metal dichalcogenides*. Nature Photonics, 2016. **10**: p. 216.
 20. Manzeli, S., et al., *2D transition metal dichalcogenides*. Nature Reviews Materials, 2017. **2**: p. 17033.
 21. Yaghi, O.M., *Reticular Chemistry—Construction, Properties, and Precision Reactions of Frameworks*. Journal of the American Chemical Society, 2016. **138**(48): p. 15507-15509.
 22. Côté, A.P., et al., *Porous, Crystalline, Covalent Organic Frameworks*. Science, 2005. **310**(5751): p. 1166-1170.
 23. Feng, X., X. Ding, and D. Jiang, *Covalent organic frameworks*. Chemical Society Reviews, 2012. **41**(18): p. 6010-6022.
 24. Uribe-Romo, F.J., et al., *Crystalline Covalent Organic Frameworks with Hydrazone Linkages*. Journal of the American Chemical Society, 2011. **133**(30): p. 11478-11481.
 25. Uribe-Romo, F.J., et al., *A Crystalline Imine-Linked 3-D Porous Covalent Organic Framework*. Journal of the American Chemical Society, 2009. **131**(13): p. 4570-4571.
 26. Hunt, J.R., et al., *Reticular Synthesis of Covalent Organic Borosilicate Frameworks*. Journal of the American Chemical Society, 2008. **130**(36): p. 11872-11873.
 27. Dalapati, S., et al., *An Azine-Linked Covalent Organic Framework*. Journal of the American Chemical Society, 2013. **135**(46): p. 17310-17313.
 28. Kuhn, P., M. Antonietti, and A. Thomas, *Porous, Covalent Triazine-Based Frameworks Prepared by Ionothermal Synthesis*. Angewandte Chemie International Edition, 2008. **47**(18): p. 3450-3453.
 29. Spitler, E.L. and W.R. Dichtel, *Lewis acid-catalysed formation of two-dimensional phthalocyanine covalent organic frameworks*. Nature Chemistry, 2010. **2**: p. 672.
 30. Diercks, C.S. and O.M. Yaghi, *The atom, the molecule, and the covalent organic framework*. Science, 2017. **355**(6328).
 31. Bisbey, R.P. and W.R. Dichtel, *Covalent Organic Frameworks as a Platform for Multidimensional Polymerization*. ACS Central Science, 2017. **3**(6): p. 533-543.
 32. Nagai, A., et al., *Pore surface engineering in covalent organic frameworks*. Nature Communications, 2011. **2**: p. 536.
 33. Furukawa, H. and O.M. Yaghi, *Storage of Hydrogen, Methane, and Carbon Dioxide in Highly Porous Covalent Organic Frameworks for Clean Energy Applications*. Journal of the American Chemical Society, 2009. **131**(25): p. 8875-8883.
 34. Doonan, C.J., et al., *Exceptional ammonia uptake by a covalent organic framework*. Nature Chemistry, 2010. **2**: p. 235.
 35. Ding, S.-Y., et al., *Construction of Covalent Organic Framework for Catalysis: Pd/COF-LZU1 in Suzuki–Miyaura Coupling Reaction*. Journal of the American Chemical Society, 2011. **133**(49): p. 19816-19822.

BIBLIOGRAPHY

36. Lin, S., et al., *Covalent organic frameworks comprising cobalt porphyrins for catalytic CO₂ reduction in water*. *Science*, 2015. **349**(6253): p. 1208.
37. Fang, Q., et al., *3D Microporous Base-Functionalized Covalent Organic Frameworks for Size-Selective Catalysis*. *Angewandte Chemie International Edition*, 2014. **53**(11): p. 2878-2882.
38. Wan, S., et al., *A Photoconductive Covalent Organic Framework: Self-Condensed Arene Cubes Composed of Eclipsed 2D Polypyrene Sheets for Photocurrent Generation*. *Angewandte Chemie International Edition*, 2009. **48**(30): p. 5439-5442.
39. Dogru, M., et al., *A Photoconductive Thienothiophene-Based Covalent Organic Framework Showing Charge Transfer Towards Included Fullerene*. *Angewandte Chemie*, 2013. **125**(10): p. 2992-2996.
40. Colson, J.W., et al., *Oriented 2D Covalent Organic Framework Thin Films on Single-Layer Graphene*. *Science*, 2011. **332**(6026): p. 228.
41. Tanoue, R., et al., *Thermodynamically Controlled Self-Assembly of Covalent Nanoarchitectures in Aqueous Solution*. *ACS Nano*, 2011. **5**(5): p. 3923-3929.
42. Dai, W., et al., *Synthesis of a Two-Dimensional Covalent Organic Monolayer through Dynamic Imine Chemistry at the Air/Water Interface*. *Angewandte Chemie International Edition*, 2016. **55**(1): p. 213-217.
43. Sahabudeen, H., et al., *Wafer-sized multifunctional polyimine-based two-dimensional conjugated polymers with high mechanical stiffness*. *Nature Communications*, 2016. **7**: p. 13461.
44. Zwaneveld, N.A.A., et al., *Organized Formation of 2D Extended Covalent Organic Frameworks at Surfaces*. *Journal of the American Chemical Society*, 2008. **130**(21): p. 6678-6679.
45. Gutzler, R., et al., *Surface mediated synthesis of 2D covalent organic frameworks: 1,3,5-tris(4-bromophenyl)benzene on graphite(001), Cu(111), and Ag(110)*. *Chemical Communications*, 2009(29): p. 4456-4458.
46. Sánchez-Sánchez, C., et al., *On-Surface Synthesis of BN-Substituted Heteroaromatic Networks*. *ACS Nano*, 2015. **9**(9): p. 9228-9235.
47. Bieri, M., et al., *Two-Dimensional Polymer Formation on Surfaces: Insight into the Roles of Precursor Mobility and Reactivity*. *Journal of the American Chemical Society*, 2010. **132**(46): p. 16669-16676.
48. Liu, X.-H., et al., *On-Surface Synthesis of Single-Layered Two-Dimensional Covalent Organic Frameworks via Solid–Vapor Interface Reactions*. *Journal of the American Chemical Society*, 2013. **135**(28): p. 10470-10474.
49. Morchutt, C., et al., *Interplay of Chemical and Electronic Structure on the Single-Molecule Level in 2D Polymerization*. *ACS Nano*, 2016. **10**(12): p. 11511-11518.
50. Steiner, C., et al., *Hierarchical on-surface synthesis and electronic structure of*

BIBLIOGRAPHY

- carbonyl-functionalized one- and two-dimensional covalent nanoarchitectures*. Nature Communications, 2017. **8**: p. 14765.
51. Binnig, G. and H. Rohrer, *Scanning tunneling microscopy - from birth to adolescence*. Reviews of Modern Physics, 1987. **59**(3): p. 615-625.
52. Binnig, G. and H. Rohrer, in *Trends in Physics 1984*, J. Janta and J. Pantoflicek, Editors. 1984, European Physical Society, The Hague: Prague. p. 38.
53. Gimzewski, J.K., E. Stoll, and R.R. Schlittler, *Scanning tunneling microscopy of individual molecules of copper phthalocyanine adsorbed on polycrystalline silver surfaces*. Surface Science, 1987. **181**(1): p. 267-277.
54. Smith, D.P., et al., *Images of a lipid bilayer at molecular resolution by scanning tunneling microscopy*. Proceedings of the National Academy of Sciences, 1987. **84**(4): p. 969-972.
55. Smith, D.P.E., M.D. Kirk, and C.F. Quate, *Molecular images and vibrational spectroscopy of sorbic acid with the scanning tunneling microscope*. The Journal of Chemical Physics, 1987. **86**(11): p. 6034-6038.
56. Gimzewski, J.K. and C. Joachim, *Nanoscale Science of Single Molecules Using Local Probes*. Science, 1999. **283**(5408): p. 1683-1688.
57. Rief, M., et al., *Single Molecule Force Spectroscopy on Polysaccharides by Atomic Force Microscopy*. Science, 1997. **275**(5304): p. 1295-1297.
58. Somorjai, G.A. and Y. Li, *Introduction to surface chemistry and catalysis*. 2010: John Wiley & Sons.
59. Bronner, C., et al., *Iodine versus Bromine Functionalization for Bottom-Up Graphene Nanoribbon Growth: Role of Diffusion*. The Journal of Physical Chemistry C, 2017. **121**(34): p. 18490-18495.
60. Shi, K.-J., et al., *On-Surface Heck Reaction of Aryl Bromides with Alkene on Au(111) with Palladium as Catalyst*. Organic Letters, 2017. **19**(11): p. 2801-2804.
61. Adisoejoso, J., et al., *A Single-Molecule-Level Mechanistic Study of Pd-Catalyzed and Cu-Catalyzed Homocoupling of Aryl Bromide on an Au(111) Surface*. Chemistry – A European Journal, 2014. **20**(14): p. 4111-4116.
62. Dong, L., P.N. Liu, and N. Lin, *Surface-Activated Coupling Reactions Confined on a Surface*. Accounts of Chemical Research, 2015. **48**(10): p. 2765-2774.
63. Zhang, Y.-Q., et al., *Homo-coupling of terminal alkynes on a noble metal surface*. Nature Communications, 2012. **3**: p. 1286.
64. Liu, J., et al., *Cyclotrimerization of arylalkynes on Au(111)*. Chemical Communications, 2014. **50**(76): p. 11200-11203.
65. Dienstmaier, J.F., et al., *Isorecticular Two-Dimensional Covalent Organic Frameworks Synthesized by On-Surface Condensation of Diboronic Acids*. ACS Nano, 2012. **6**(8): p. 7234-7242.

BIBLIOGRAPHY

66. Weigelt, S., et al., *Molecular Self-Assembly from Building Blocks Synthesized on a Surface in Ultrahigh Vacuum: Kinetic Control and Topo-Chemical Reactions*. ACS Nano, 2008. **2**(4): p. 651-660.
67. Liu, X.-H., et al., *Surface Host–Guest Supramolecular Assemblies on Porphyrin-Based Covalent Organic Grids*. The Journal of Physical Chemistry C, 2016. **120**(29): p. 15753-15757.
68. Chen, C., et al., *Local Electronic Structure of a Single-Layer Porphyrin-Containing Covalent Organic Framework*. ACS Nano, 2018. **12**(1): p. 385-391.
69. Matena, M., et al., *Transforming Surface Coordination Polymers into Covalent Surface Polymers: Linked Polycondensed Aromatics through Oligomerization of N-Heterocyclic Carbene Intermediates*. Angewandte Chemie, 2008. **120**(13): p. 2448-2451.
70. Zhong, D., et al., *Linear Alkane Polymerization on a Gold Surface*. Science, 2011. **334**(6053): p. 213-216.
71. Treier, M., N.V. Richardson, and R. Fasel, *Fabrication of Surface-Supported Low-Dimensional Polyimide Networks*. Journal of the American Chemical Society, 2008. **130**(43): p. 14054-14055.
72. Marele, A.C., et al., *Formation of a surface covalent organic framework based on polyester condensation*. Chemical Communications, 2012. **48**(54): p. 6779-6781.
73. Sun, Q., et al., *On-Surface Formation of One-Dimensional Polyphenylene through Bergman Cyclization*. Journal of the American Chemical Society, 2013. **135**(23): p. 8448-8451.
74. de Oteyza, D.G., et al., *Direct Imaging of Covalent Bond Structure in Single-Molecule Chemical Reactions*. Science, 2013.
75. Treier, M., et al., *Surface-assisted cyclodehydrogenation provides a synthetic route towards easily processable and chemically tailored nanographenes*. Nature Chemistry, 2010. **3**: p. 61.
76. Otero, G., et al., *Fullerenes from aromatic precursors by surface-catalysed cyclodehydrogenation*. Nature, 2008. **454**: p. 865.
77. Bebensee, F., et al., *On-Surface Azide–Alkyne Cycloaddition on Cu(111): Does It “Click” in Ultrahigh Vacuum?* Journal of the American Chemical Society, 2013. **135**(6): p. 2136-2139.
78. Díaz Arado, O., et al., *On-Surface Azide–Alkyne Cycloaddition on Au(111)*. ACS Nano, 2013. **7**(10): p. 8509-8515.
79. Ullmann, F. and J. Bielecki, *Ueber Synthesen in der Biphenylreihe*. Berichte der deutschen chemischen Gesellschaft, 1901. **34**(2): p. 2174-2185.
80. Sambigiato, C., et al., *Copper catalysed Ullmann type chemistry: from mechanistic aspects to modern development*. Chemical Society Reviews, 2014. **43**(10): p. 3525-3550.
81. Xi, M. and B.E. Bent, *Iodobenzene on Cu(111): formation and coupling of adsorbed*

BIBLIOGRAPHY

- phenyl groups*. Surface Science, 1992. **278**(1): p. 19-32.
82. Xi, M. and B.E. Bent, *Mechanisms of the Ullmann coupling reaction in adsorbed monolayers*. Journal of the American Chemical Society, 1993. **115**(16): p. 7426-7433.
83. Hla, S.-W., et al., *Inducing All Steps of a Chemical Reaction with the Scanning Tunneling Microscope Tip: Towards Single Molecule Engineering*. Physical Review Letters, 2000. **85**(13): p. 2777-2780.
84. Grill, L., et al., *Nano-architectures by covalent assembly of molecular building blocks*. Nature Nanotechnology, 2007. **2**: p. 687.
85. Lipton-Duffin, J.A., et al., *Synthesis of Polyphenylene Molecular Wires by Surface-Confining Polymerization*. Small, 2009. **5**(5): p. 592-597.
86. Lewis, E.A., et al., *Atomic-scale insight into the formation, mobility and reaction of Ullmann coupling intermediates*. Chemical Communications, 2014. **50**(8): p. 1006-1008.
87. Wang, W., et al., *Single-Molecule Resolution of an Organometallic Intermediate in a Surface-Supported Ullmann Coupling Reaction*. Journal of the American Chemical Society, 2011. **133**(34): p. 13264-13267.
88. Park, J., et al., *Interchain Interactions Mediated by Br Adsorbates in Arrays of Metal–Organic Hybrid Chains on Ag(111)*. The Journal of Physical Chemistry C, 2011. **115**(30): p. 14834-14838.
89. Chung, K.-H., et al., *Electronic structures of one-dimensional metal-molecule hybrid chains studied using scanning tunneling microscopy and density functional theory*. Physical Chemistry Chemical Physics, 2012. **14**(20): p. 7304-7308.
90. Schiff, H., *Mittheilungen aus dem Universitätslaboratorium in Pisa: Eine neue Reihe organischer Basen*. Justus Liebigs Annalen der Chemie, 1864. **131**(1): p. 118-119.
91. Segura, J.L., M.J. Mancheno, and F. Zamora, *Covalent organic frameworks based on Schiff-base chemistry: synthesis, properties and potential applications*. Chemical Society Reviews, 2016. **45**(20): p. 5635-5671.
92. Hu, F.-Y., et al., *In Situ STM Investigation of Two-Dimensional Chiral Assemblies through Schiff-Base Condensation at a Liquid/Solid Interface*. ACS Applied Materials & Interfaces, 2013. **5**(5): p. 1583-1587.
93. Xu, L., et al., *Surface-Confining Crystalline Two-Dimensional Covalent Organic Frameworks via on-Surface Schiff-Base Coupling*. ACS Nano, 2013. **7**(9): p. 8066-8073.
94. Liu, X.-H., et al., *Molecular engineering of Schiff-base linked covalent polymers with diverse topologies by gas-solid interface reaction*. The Journal of Chemical Physics, 2015. **142**(10): p. 101905.
95. Hu, Y., et al., *Probing the chemical structure of monolayer covalent-organic frameworks grown via Schiff-base condensation reactions*. Chemical Communications, 2016. **52**(64): p. 9941-9944.
96. Rowan, S.J., et al., *Dynamic Covalent Chemistry*. Angewandte Chemie International

BIBLIOGRAPHY

- Edition, 2002. **41**(6): p. 898-952.
97. Binnig, G., et al., *Tunneling through a controllable vacuum gap*. Applied Physics Letters, 1982. **40**(2): p. 178-180.
 98. Binnig, G., et al., *Surface Studies by Scanning Tunneling Microscopy*. Physical Review Letters, 1982. **49**(1): p. 57-61.
 99. Binnig, G., et al., *7x7 Reconstruction on Si(111) Resolved in Real Space*. Physical Review Letters, 1983. **50**(2): p. 120-123.
 100. Bardeen, J., *Tunnelling from a Many-Particle Point of View*. Physical Review Letters, 1961. **6**(2): p. 57-59.
 101. Tersoff, J. and D.R. Hamann, *Theory and Application for the Scanning Tunneling Microscope*. Physical Review Letters, 1983. **50**(25): p. 1998-2001.
 102. Tersoff, J. and D.R. Hamann, *Theory of the scanning tunneling microscope*. Physical Review B, 1985. **31**(2): p. 805-813.
 103. Chen, C.J., *Introduction to scanning tunneling microscopy*. Vol. 4. 1993: Oxford University Press on Demand.
 104. Alex, D.G. and W. Lisa, *Bardeen's tunnelling theory as applied to scanning tunnelling microscopy: a technical guide to the traditional interpretation*. Nanotechnology, 2006. **17**(8): p. R57.
 105. Ashcroft, N.W. and N.D. Mermin, *Solid State Physics*. 1985, Philadelphia: Sanders College.
 106. Chen, W., *STM investigations of pristine Au(111) at low temperature and surface-supported magnetic clusters*. 1999, Boston University.
 107. Madhavan, V., *Electronic properties of magnetic nanoclusters: a scanning tunneling microscope study of transition metal atoms on Au(111)*. 2000, Boston University.
 108. Jamneala, T., *Tunneling measurement of the electronic structure of magnetic nanostructures on surfaces*. 2001, University of California, Berkeley.
 109. Grobis, M., *Scanning tunneling spectroscopy of fullerene nanostructures*. 2005, University of California, Berkeley.
 110. Yamachika, R., *Probing atomic-scale properties of organic and organometallic molecules by scanning tunneling spectroscopy*. 2009, University of California, Berkeley.
 111. Chen, Y.-C., et al., *Tuning the Band Gap of Graphene Nanoribbons Synthesized from Molecular Precursors*. ACS Nano, 2013. **7**(7): p. 6123-6128.
 112. Cai, J., et al., *Graphene nanoribbon heterojunctions*. Nature Nanotechnology, 2014. **9**: p. 896.
 113. Ruffieux, P., et al., *On-surface synthesis of graphene nanoribbons with zigzag edge topology*. Nature, 2016. **531**: p. 489.
 114. Bronner, C., et al., *Aligning the Band Gap of Graphene Nanoribbons by Monomer Doping*. Angewandte Chemie International Edition, 2013. **52**(16): p. 4422-4425.

BIBLIOGRAPHY

115. Nguyen, G.D., et al., *Bottom-Up Synthesis of $N = 13$ Sulfur-Doped Graphene Nanoribbons*. The Journal of Physical Chemistry C, 2016. **120**(5): p. 2684-2687.
116. Nguyen, G.D., et al., *Atomically precise graphene nanoribbon heterojunctions from a single molecular precursor*. Nature Nanotechnology, 2017. **12**: p. 1077.
117. Cloke, R.R., et al., *Site-Specific Substitutional Boron Doping of Semiconducting Armchair Graphene Nanoribbons*. Journal of the American Chemical Society, 2015. **137**(28): p. 8872-8875.
118. Kawai, S., et al., *Atomically controlled substitutional boron-doping of graphene nanoribbons*. Nature Communications, 2015. **6**: p. 8098.
119. Franc, G. and A. Gourdon, *Covalent networks through on-surface chemistry in ultra-high vacuum: state-of-the-art and recent developments*. Physical Chemistry Chemical Physics, 2011. **13**(32): p. 14283-14292.
120. Ruffieux, P., et al., *Electronic Structure of Atomically Precise Graphene Nanoribbons*. ACS Nano, 2012. **6**(8): p. 6930-6935.
121. Koch, M., et al., *Voltage-dependent conductance of a single graphene nanoribbon*. Nature Nanotechnology, 2012. **7**: p. 713.
122. Ijäs, M., et al., *Electronic states in finite graphene nanoribbons: Effect of charging and defects*. Physical Review B, 2013. **88**(7): p. 075429.
123. Hod, O., J.E. Peralta, and G.E. Scuseria, *Edge effects in finite elongated graphene nanoribbons*. Physical Review B, 2007. **76**(23): p. 233401.
124. Cao, T., F. Zhao, and S.G. Louie, *Topological Phases in Graphene Nanoribbons: Junction States, Spin Centers, and Quantum Spin Chains*. Physical Review Letters, 2017. **119**(7): p. 076401.
125. Carbonell-Sanromà, E., et al., *Quantum Dots Embedded in Graphene Nanoribbons by Chemical Substitution*. Nano Letters, 2017. **17**(1): p. 50-56.
126. Abdurakhmanova, N., et al., *Synthesis of wide atomically precise graphene nanoribbons from para-oligophenylene based molecular precursor*. Carbon, 2014. **77**: p. 1187-1190.
127. Zhang, H., et al., *On-Surface Synthesis of Rylene-Type Graphene Nanoribbons*. Journal of the American Chemical Society, 2015. **137**(12): p. 4022-4025.
128. Kimouche, A., et al., *Ultra-narrow metallic armchair graphene nanoribbons*. Nature Communications, 2015. **6**: p. 10177.
129. Bennett, P.B., et al., *Bottom-up graphene nanoribbon field-effect transistors*. Applied Physics Letters, 2013. **103**(25): p. 253114.
130. Llinas, J.P., et al., *Short-channel field-effect transistors with 9-atom and 13-atom wide graphene nanoribbons*. Nature Communications, 2017. **8**(1): p. 633.
131. Zhang, Q., et al., *Graphene Nanoribbon Tunnel Transistors*. IEEE Electron Device Letters, 2008. **29**(12): p. 1344-1346.
132. Müllegger, S., et al., *Spectroscopic STM Studies of Single Gold(III) Porphyrin Molecules*.

BIBLIOGRAPHY

- Journal of the American Chemical Society, 2009. **131**(49): p. 17740-17741.
133. Wan, S., et al., *Covalent Organic Frameworks with High Charge Carrier Mobility*. Chemistry of Materials, 2011. **23**(18): p. 4094-4097.
134. Yokoyama, T., et al., *Nonplanar adsorption and orientational ordering of porphyrin molecules on Au(111)*. The Journal of Chemical Physics, 2001. **115**(8): p. 3814-3818.
135. Zhang, Q., et al., *Single-Molecule Investigations of Conformation Adaptation of Porphyrins on Surfaces*. The Journal of Physical Chemistry Letters, 2017. **8**(6): p. 1241-1247.
136. Auwärter, W., et al., *Site-specific electronic and geometric interface structure of Co-tetraphenyl-porphyrin layers on Ag(111)*. Physical Review B, 2010. **81**(24): p. 245403.
137. Tkatchenko, A. and M. Scheffler, *Accurate Molecular Van Der Waals Interactions from Ground-State Electron Density and Free-Atom Reference Data*. Physical Review Letters, 2009. **102**(7): p. 073005.
138. Kresse, G. and J. Furthmüller, *Efficient iterative schemes for ab initio total-energy calculations using a plane-wave basis set*. Physical Review B, 1996. **54**(16): p. 11169-11186.
139. Kresse, G. and J. Furthmüller, *Efficiency of ab-initio total energy calculations for metals and semiconductors using a plane-wave basis set*. Computational Materials Science, 1996. **6**(1): p. 15-50.
140. Adjizian, J.-J., et al., *Dirac Cones in two-dimensional conjugated polymer networks*. Nature Communications, 2014. **5**: p. 5842.
141. Liu, Z., F. Liu, and Y.-S. Wu, *Exotic electronic states in the world of flat bands: From theory to material*. Chinese Physics B, 2014. **23**(7): p. 077308.
142. Slot, M.R., et al., *Experimental realization and characterization of an electronic Lieb lattice*. Nature Physics, 2017. **13**: p. 672.
143. Han, T.-H., et al., *Fractionalized excitations in the spin-liquid state of a kagome-lattice antiferromagnet*. Nature, 2012. **492**: p. 406.
144. Rogers, C., et al., *Closing the Nanographene Gap: Surface-Assisted Synthesis of Peripentacene from 6,6'-Bipentacene Precursors*. Angewandte Chemie International Edition, 2015. **54**(50): p. 15143-15146.
145. Narita, A., et al., *New advances in nanographene chemistry*. Chemical Society Reviews, 2015. **44**(18): p. 6616-6643.
146. Anthony, J.E., *The Larger Acenes: Versatile Organic Semiconductors*. Angewandte Chemie International Edition, 2008. **47**(3): p. 452-483.
147. Ye, Q. and C. Chi, *Recent Highlights and Perspectives on Acene Based Molecules and Materials*. Chemistry of Materials, 2014. **26**(14): p. 4046-4056.
148. Sun, Z., et al., *Low band gap polycyclic hydrocarbons: from closed-shell near infrared*

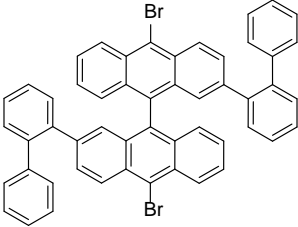
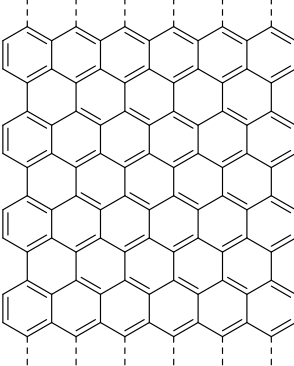
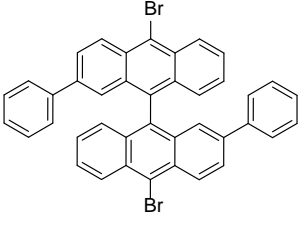
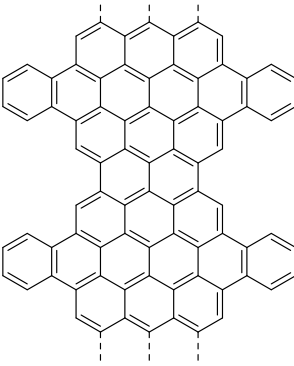
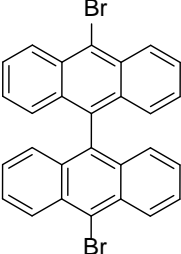
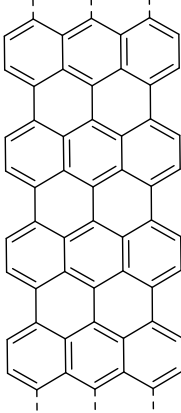
BIBLIOGRAPHY

- dyes and semiconductors to open-shell radicals*. Chemical Society Reviews, 2012. **41**(23): p. 7857-7889.
149. Jiang, D.-e., B.G. Sumpter, and S. Dai, *First principles study of magnetism in nanographenes*. The Journal of Chemical Physics, 2007. **127**(12): p. 124703.
150. Şahin, H. and R.T. Senger, *First-principles calculations of spin-dependent conductance of graphene flakes*. Physical Review B, 2008. **78**(20): p. 205423.
151. Plasser, F., et al., *The Multiradical Character of One- and Two-Dimensional Graphene Nanoribbons*. Angewandte Chemie International Edition, 2013. **52**(9): p. 2581-2584.
152. Fort, E.H., P.M. Donovan, and L.T. Scott, *Diels–Alder Reactivity of Polycyclic Aromatic Hydrocarbon Bay Regions: Implications for Metal-Free Growth of Single-Chirality Carbon Nanotubes*. Journal of the American Chemical Society, 2009. **131**(44): p. 16006-16007.
153. Hirao, Y., et al., *Synthesis and electronic structure of bisanthene: A small molecular-sized graphene with zigzag edges*. AIP Conference Proceedings, 2012. **1504**(1): p. 863-866.
154. Konishi, A., et al., *Synthesis and Characterization of Teranthene: A Singlet Biradical Polycyclic Aromatic Hydrocarbon Having Kekulé Structures*. Journal of the American Chemical Society, 2010. **132**(32): p. 11021-11023.
155. Zöphel, L., et al., *Toward the peri-Pentacene Framework*. Chemistry – A European Journal, 2013. **19**(52): p. 17821-17826.
156. Dorel, R., et al., *Tetrabenzocircumpyrrene: a nanographene fragment with an embedded peripentacene core*. Chemical Communications, 2015. **51**(32): p. 6932-6935.
157. Liu, J., et al., *Tetrabenz[o{a,f,j,o}]perylene: A Polycyclic Aromatic Hydrocarbon With An Open-Shell Singlet Biradical Ground State*. Angewandte Chemie International Edition, 2015. **54**(42): p. 12442-12446.
158. Matsumoto, A., et al., *Tetrabenzoperipentacene: Stable Five-Electron Donating Ability and a Discrete Triple-Layered β -Graphite Form in the Solid State*. Angewandte Chemie International Edition, 2015. **54**(28): p. 8175-8178.
159. Zhang, X., et al., *Fused Bispentacenequinone and Its Unexpected Michael Addition*. Organic Letters, 2010. **12**(17): p. 3946-3949.
160. Konishi, A., et al., *Facile Synthesis and Lateral π -Expansion of Bisanthenes*. Chemistry Letters, 2013. **42**(6): p. 592-594.
161. Konishi, A., et al., *Synthesis and Characterization of Quarteranthene: Elucidating the Characteristics of the Edge State of Graphene Nanoribbons at the Molecular Level*. Journal of the American Chemical Society, 2013. **135**(4): p. 1430-1437.
162. Gross, L., et al., *The Chemical Structure of a Molecule Resolved by Atomic Force Microscopy*. Science, 2009. **325**(5944): p. 1110.
163. Giessibl, F.J., *High-speed force sensor for force microscopy and profilometry utilizing a quartz tuning fork*. Applied Physics Letters, 1998. **73**(26): p. 3956-3958.

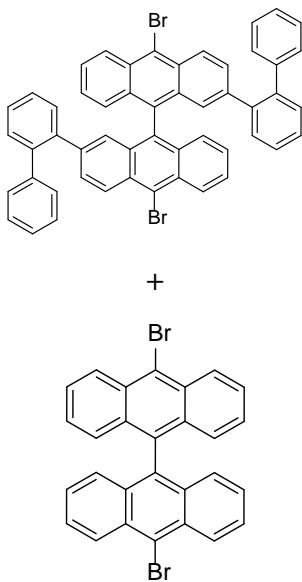
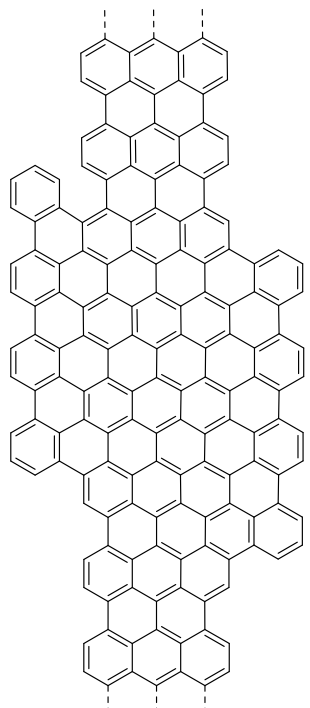
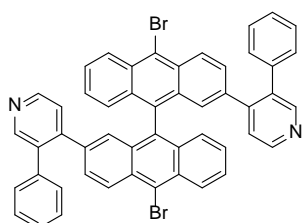
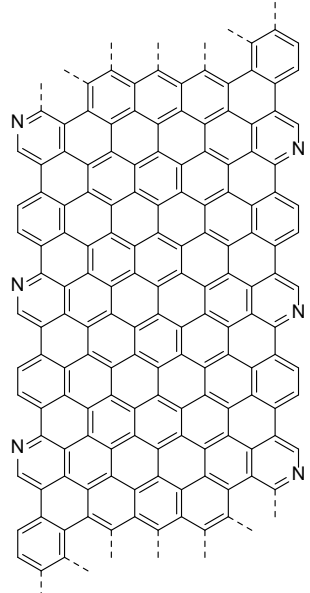
BIBLIOGRAPHY

164. Giessibl, F.J., *Atomic resolution on Si(111)-(7×7) by noncontact atomic force microscopy with a force sensor based on a quartz tuning fork*. Applied Physics Letters, 2000. **76**(11): p. 1470-1472.
165. Giessibl, F.J., *Advances in atomic force microscopy*. Reviews of Modern Physics, 2003. **75**(3): p. 949-983.
166. Lehnherr, D., et al., *Sequence-defined oligo(ortho-arylene) foldamers derived from the benzannulation of ortho(arylene ethynylene)s*. Chemical Science, 2016. **7**(10): p. 6357-6364.

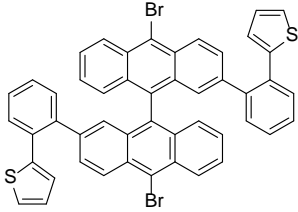
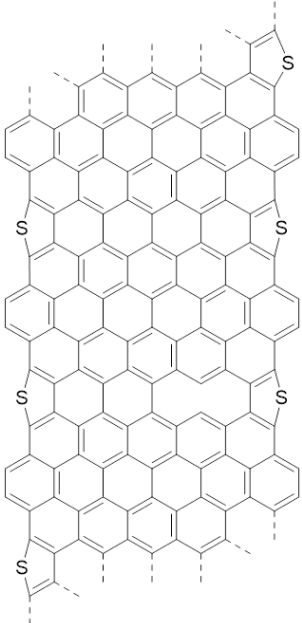
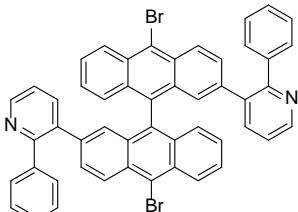
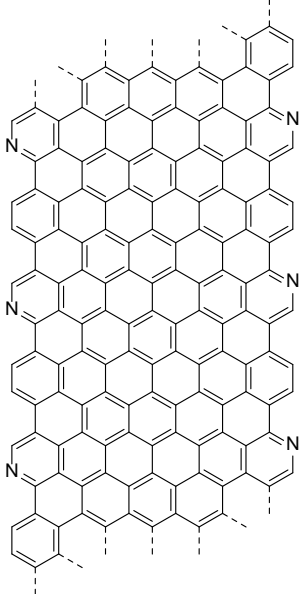
Appendix: List of All Molecules Studied

Molecule	Expected Product	Result Summary	Time Period*
		<p>On Au(111): N=13 AGNRs with atomically precise edges</p>	<p>LT Jan. 2013 to Feb. 2013</p>
		<p>On Au(111): only saw one GNR segment with desired product</p>	<p>LT Mar. 2013</p>
		<p>On Au(111): N=7 AGNRs with atomically precise edges</p>	<p>LT Mar. 2013</p>

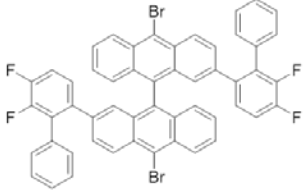
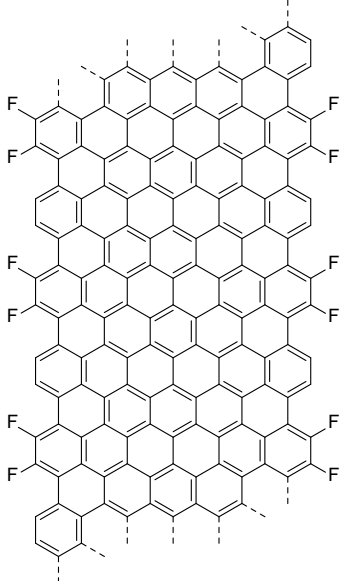
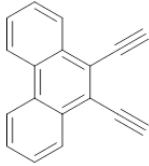
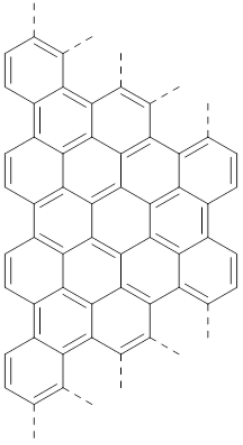
APPENDIX: LIST OF ALL MOLECULES STUDIED

		<p>On Au(111): 7-13 AGNR heterojunctions with atomically precise interface structure, but segment lengths are random.</p>	<p>LT Mar.2013 to Sep. 2013</p>
		<p>On Au(111): irregular, worm-like structure; no GNRs.</p>	<p>LT Jun. 2013 to Jul. 2013</p>

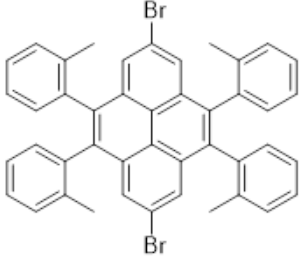
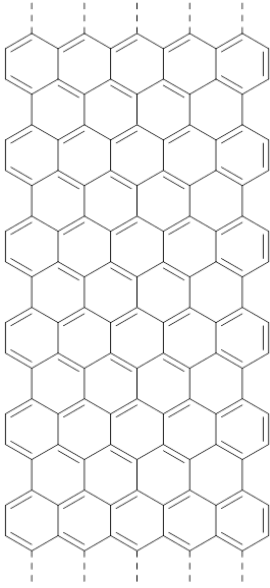
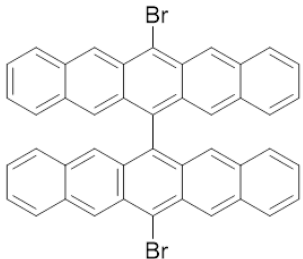
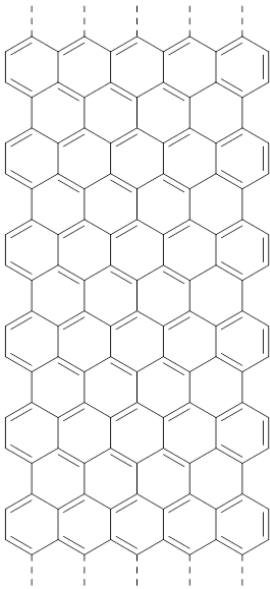
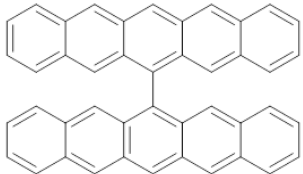
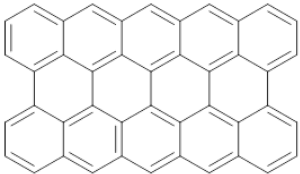
APPENDIX: LIST OF ALL MOLECULES STUDIED

		<p>On Au(111): some linear ribbons; edges tend to be defective</p>	<p>LT Jul. 2013</p>
		<p>On Au(111): irregular, worm-like structure; no GNRs.</p>	<p>LT Oct. 2013 to Nov. 2013</p>

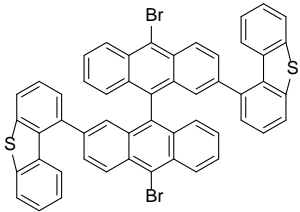
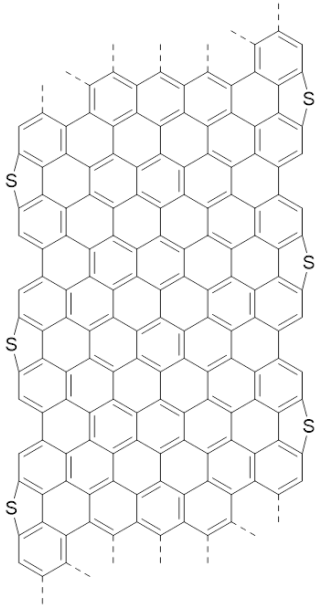
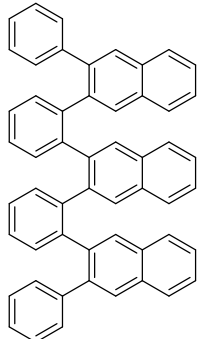
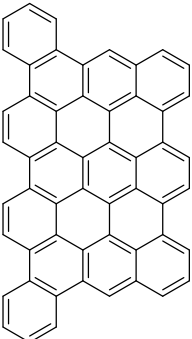
APPENDIX: LIST OF ALL MOLECULES STUDIED

		<p>On Au(111): irregular, worm-like structure; no GNRs.</p>	<p>LT Nov. 2013</p>
		<p>On Au(111): oligomers after moderate annealing, irregular worm-like structure after high annealing. On Cu(111): ordered linear structure and oligomers. No GNRs on either surface.</p>	<p>LT Dec. 2013 to Apr. 2014</p>

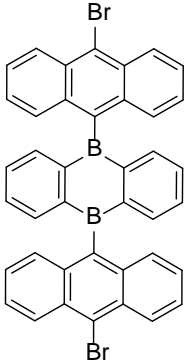
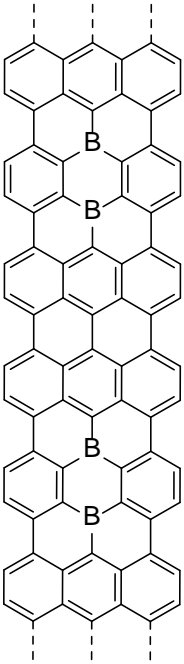
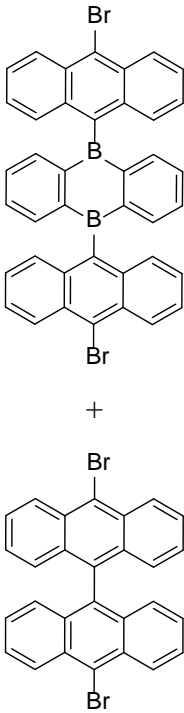
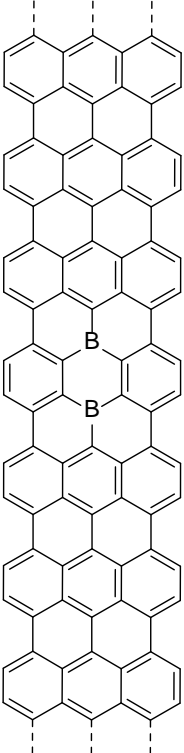
APPENDIX: LIST OF ALL MOLECULES STUDIED

		<p>On Au(111): defective N=11 AGNRs</p>	<p>LT Apr. 2014 to Jul. 2014, Oct. 2014 to Nov. 2014, Jun. 2015 to Jul. 2015</p>
		<p>On Au(111): mostly intra-molecular cyclized nano-graphene; few oligomers.</p>	<p>LT Jul. 2014 to Aug. 2014</p>
		<p>On Au(111): fully cyclized peripentacene</p>	<p>LT Dec. 2014 to Apr. 2015</p>

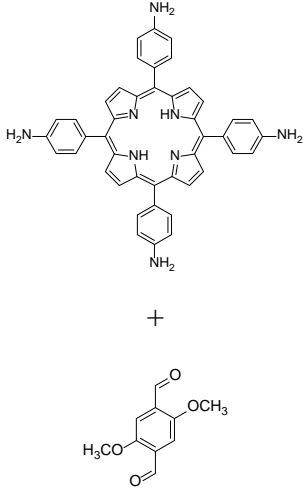
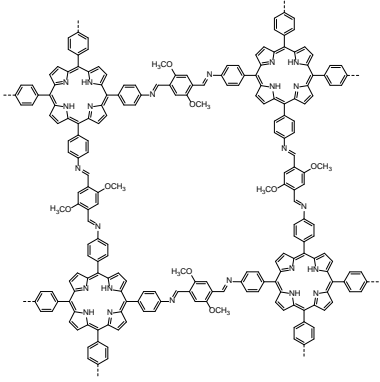
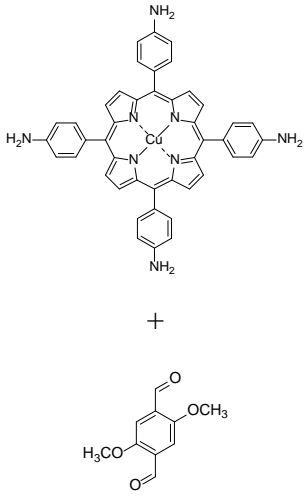
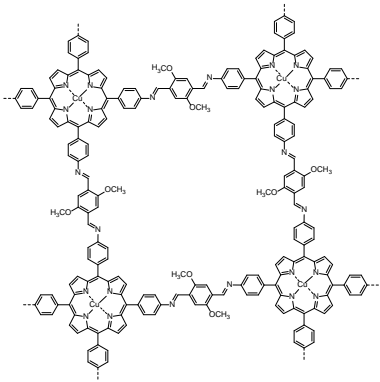
APPENDIX: LIST OF ALL MOLECULES STUDIED

		<p>On Au(111): saw some nice hexagonal self-assembly; irregular worm-like structures after annealing.</p>	<p>LT Aug. 2014 to Sep. 2014</p>
		<p>On Au(111): ordered self-assembly at high coverage. Stepwise annealing gradually flattens the molecules until fully cyclized product, also saw other by-products such as oligomers.</p>	<p>LT Jul. 2015 to Aug. 2015</p>

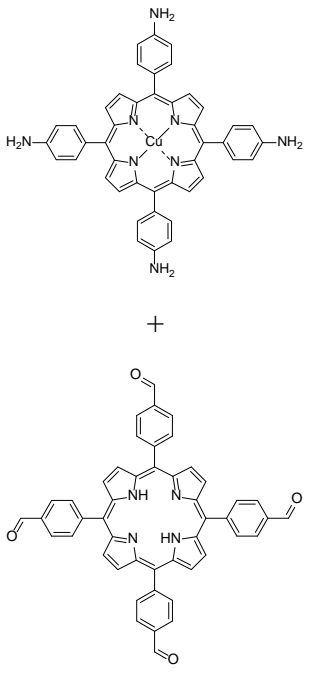
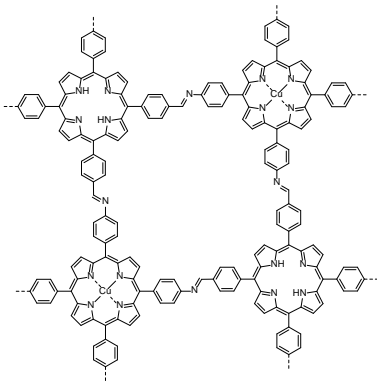
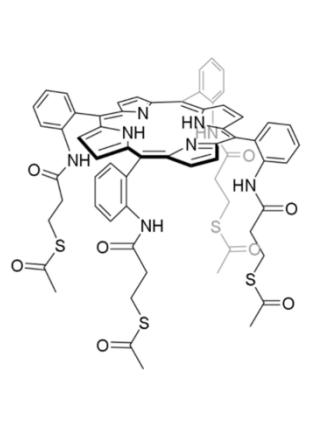
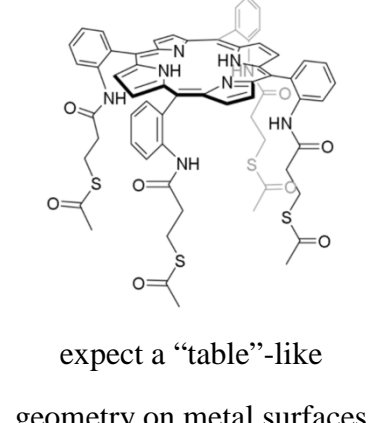
APPENDIX: LIST OF ALL MOLECULES STUDIED

		<p>On Au(788): able to get B-doped 7-AGNRs, although sample quality was not the best (short ribbons and quite some dirt).</p>	<p>LT Aug. 2015 to Sep. 2015</p>
		<p>On Au(111): dilute boron-doped 7-AGNRs with various dopant concentrations</p>	<p>LT Sep. 2015 to Jan. 2016, Apr. 2016 to May 2016</p>

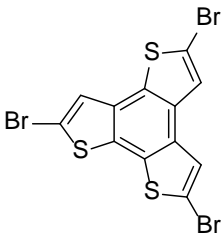
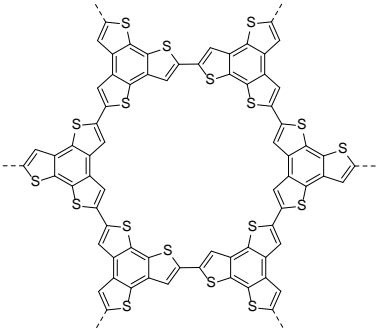
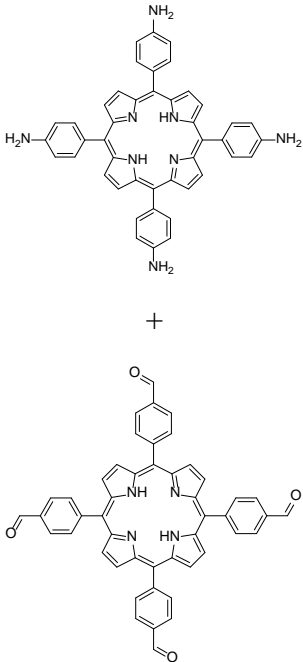
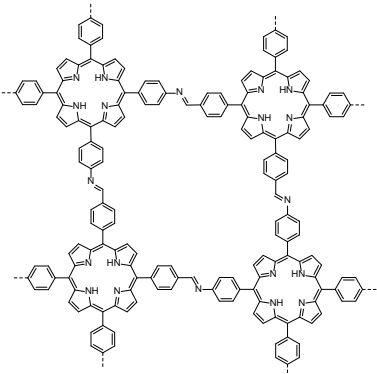
APPENDIX: LIST OF ALL MOLECULES STUDIED

		<p>On Au(111): square lattice COF with core-linker geometry.</p>	<p>LT Jul. 2016 to Nov. 2016</p>
		<p>On Au(111): square lattice COF with core-linker geometry. Low coverage with small domain size.</p>	<p>LT Dec. 2016</p>

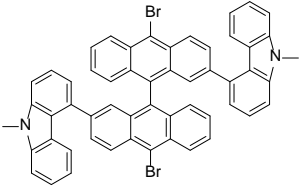
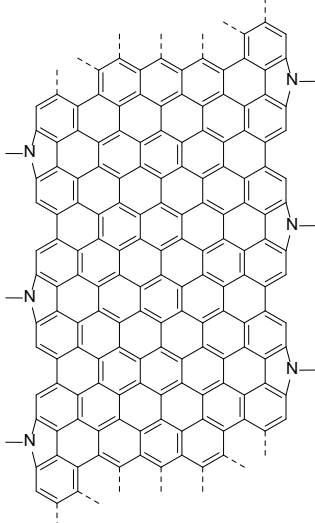
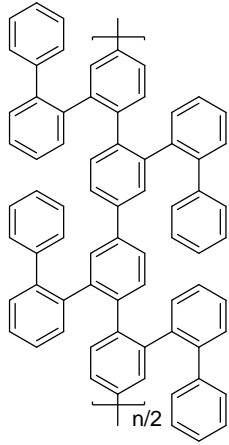
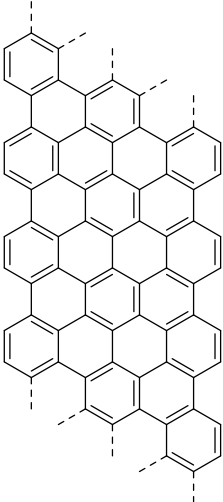
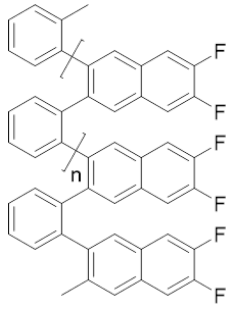
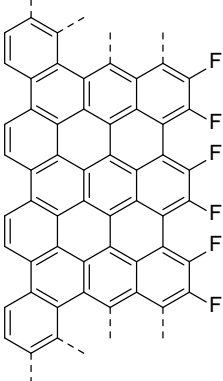
APPENDIX: LIST OF ALL MOLECULES STUDIED

 <p>+</p>		<p>On Au(111): square lattice COF with checker board pattern.</p>	<p>LT Dec. 2016 to Apr. 2017</p>
	 <p>expect a “table”-like geometry on metal surfaces</p>	<p>On Cu(111): molecules of irregular shapes; nothing resembles the expected “table”-like geometry</p>	<p>LT Apr. 2017</p>

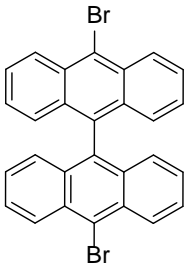
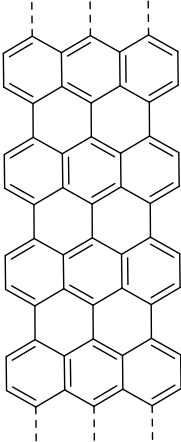
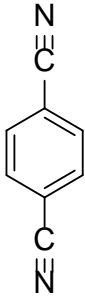
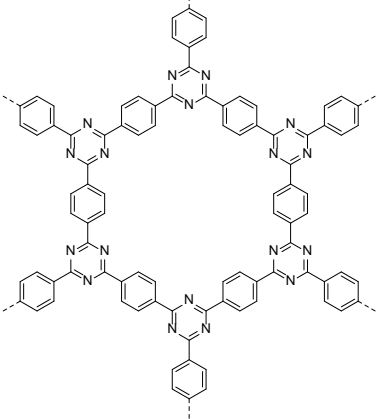
APPENDIX: LIST OF ALL MOLECULES STUDIED

		<p>On Au(111): imperfect hexagonal lattice.</p> <p>On Cu(111): worm-like structure instead of ordered hexagons.</p> <p>On Ag(111): imperfect hexagonal lattice; also saw organometallic intermediate.</p>	<p>LT May 2017 to Jul. 2017, Feb. 2018 to Mar. 2018</p>
		<p>On Au(111): square lattice COF with checker board pattern.</p>	<p>LT Aug. 2017 to Jan. 2018</p>

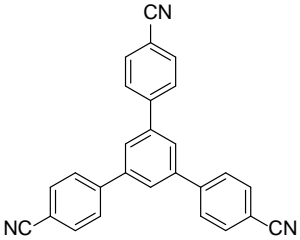
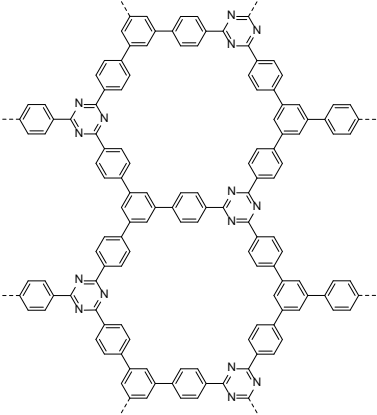
APPENDIX: LIST OF ALL MOLECULES STUDIED

		<p>On Au(111): random branches, no GNRs.</p>	<p>RT Mar. 2014 to Apr. 2014</p>
 <p>polymer solution</p>		<p>On Au(111): annealing the drop-coated polymer solution (DCM as solvent) resulted in N=9 AGNRs, with dirt on surface. Hard to reproduce.</p>	<p>RT Jun. 2014 to Aug. 2014</p>
 <p>polymer solution</p>		<p>On Au(111): annealing after drop-coating resulted worm-like structure on the surface; no GNRs.</p>	<p>RT Aug. 2014</p>

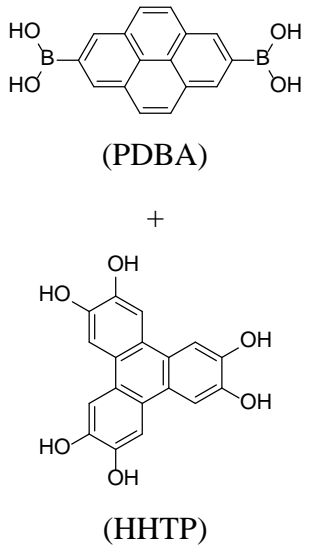
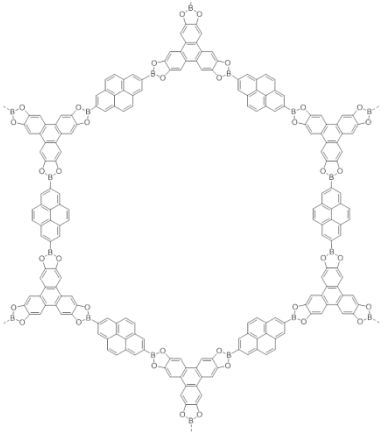
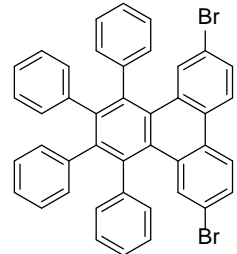
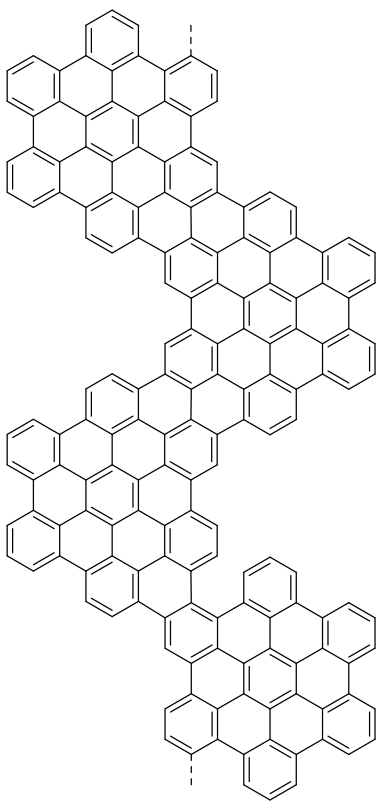
APPENDIX: LIST OF ALL MOLECULES STUDIED

 <p>Chemical structure of 2,6-dibromo-1,3-bis(phenyl)benzene, showing two phenyl rings connected at their 1-positions to a central benzene ring, with bromine atoms at the 2 and 6 positions of the central ring.</p>	 <p>Schematic representation of a zigzag nanoribbon structure, showing a chain of fused benzene rings with dashed lines indicating the continuation of the lattice.</p>	<p>On Au(788): able to get long N=7 AGNRs along step edges of Au(788).</p>	<p>RT Jun. 2015</p>
 <p>Chemical structure of 1,4-bis(cyano)benzene, showing a benzene ring with cyano groups (-C≡N) at the 1 and 4 positions.</p>	 <p>Schematic representation of a zigzag nanoribbon structure, showing a chain of fused benzene rings with cyano groups (-C≡N) attached to the structure.</p>	<p>Difficult to deposit onto Au(111) due to high vapor pressure of precursor (10^{-3} torr at 25 °C),</p>	<p>RT Jan. 2016 to Feb. 2016</p>

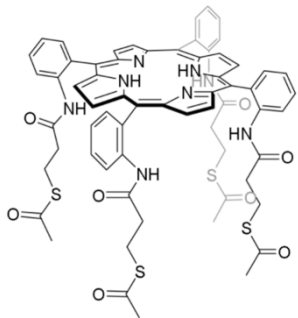
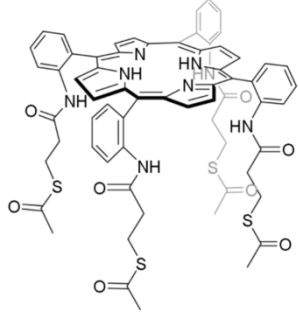
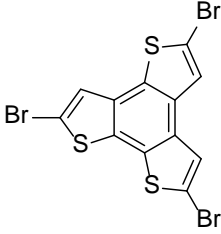
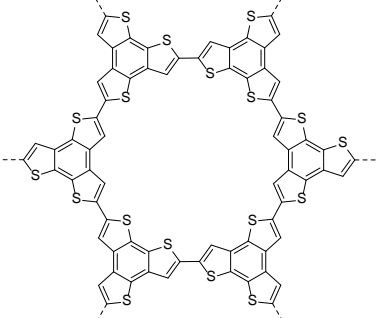
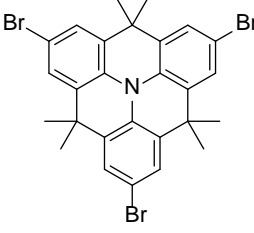
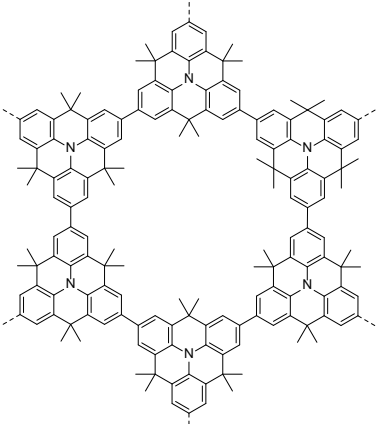
APPENDIX: LIST OF ALL MOLECULES STUDIED

 <p>Chemical structure of a molecule consisting of a central benzene ring substituted with three 4-cyanophenyl groups.</p>	 <p>Chemical structure of a large, complex, worm-like molecular structure, possibly a macrocyclic or dendritic molecule, featuring multiple benzene rings and nitrogen-containing heterocycles.</p>	<p>On Au(111): saw molecular self-assembly and random worm-like structure upon annealing; no COFs. On Ag(111): very nice and ordered molecular self-assembly upon annealing; further annealing results in desorption of most molecules.</p>	<p>RT Feb. 2016 to Mar. 2016</p>
---	--	---	--

APPENDIX: LIST OF ALL MOLECULES STUDIED

 <p> <chem>O[B-](O)c1ccc2c(c1)ccc3c2c(O)cc3</chem> (PDBA) + <chem>Oc1cc(O)c(O)c(O)c1</chem> (HHTP) </p>		<p>On Ag(111): after depositing PDBA, no molecular structure on the surface. On Au(111): molecular self-assembly for HHTP; no clear evidence of PDBA on the surface, and no COF.</p>	<p>RT May 2016 to Jun. 2016</p>
		<p>On Au(111): nice Chevron GNRs as expected</p>	<p>RT Sep. 2016</p>

APPENDIX: LIST OF ALL MOLECULES STUDIED

	 <p>expect a “table”-like geometry on metal surfaces</p>	<p>On Au(111) and Cu(111): able to deposit molecules onto both surfaces, but not enough resolution to tell the geometry.</p>	<p>RT Feb. 2017 to Mar. 2017</p>
		<p>On Au(111): got the hexagonal lattice with high coverage. On Ag(111): also saw hexagonal lattice, which might be MOF or COF.</p>	<p>RT Mar. 2017 to Jun. 2017</p>
		<p>On Au(111): hexagonal COF with high coverage</p>	<p>RT May 2017</p>

* “LT” and “RT” represent low temperature and room temperature STM, respectively.